

# Actin polymerisation and crosslinking drive left-right asymmetry in single cell and cell collectives

Received: 17 December 2021

Accepted: 6 January 2023

Published online: 11 February 2023

 Check for updates

Yee Han Tee  <sup>1</sup>✉, Wei Jia Goh <sup>1,7</sup>, Xianbin Yong  <sup>1,7</sup>, Hui Ting Ong <sup>1</sup>, Jinrong Hu <sup>1</sup>, Ignacius Yan Yun Tay <sup>1</sup>, Shidong Shi <sup>1</sup>, Salma Jalal <sup>1</sup>, Samuel F. H. Barnett <sup>1</sup>, Pakorn Kanchanawong  <sup>1,2</sup>, Wenmao Huang <sup>3</sup>, Jie Yan  <sup>1,3</sup>, Yong Ann Ben Lim <sup>1</sup>, Visalatchi Thiagarajan <sup>1</sup>, Alex Mogilner  <sup>4,5</sup> & Alexander D. Bershadsky  <sup>1,6</sup>✉

Deviations from mirror symmetry in the development of bilateral organisms are common but the mechanisms of initial symmetry breaking are insufficiently understood. The actin cytoskeleton of individual cells self-organises in a chiral manner, but the molecular players involved remain essentially unidentified and the relationship between chirality of an individual cell and cell collectives is unclear. Here, we analysed self-organisation of the chiral actin cytoskeleton in individual cells on circular or elliptical patterns, and collective cell alignment in confined microcultures. Screening based on deep-learning analysis of actin patterns identified actin polymerisation regulators, depletion of which suppresses chirality (mDia1) or reverses chirality direction (profilin1 and CapZ $\beta$ ). The reversed chirality is mDia1-independent but requires the function of actin-crosslinker  $\alpha$ -actinin1. A robust correlation between the effects of a variety of actin assembly regulators on chirality of individual cells and cell collectives is revealed. Thus, actin-driven cell chirality may underlie tissue and organ asymmetry.

While many animals demonstrate approximate bilateral symmetry, many important features of the body layout such as position of visceral organs, as well as the shape of organs themselves are usually asymmetric. These asymmetries are tightly programmed and aberrations in such a program can lead to severe defects in embryonic development<sup>1</sup>. Several examples of left-right asymmetry emerging have been discovered. At the level of entire organisms, emergence of left-right asymmetry has been thoroughly described for visceral organs in vertebrates<sup>1,2</sup> and formation of asymmetric body in snails<sup>3</sup>. The processes of asymmetric organogenesis include heart-looping in vertebrates<sup>4</sup>, chiral shaping of hindgut and genitalia<sup>5,6</sup>, and asymmetric tilting of wing bristles in *Drosophila*<sup>7</sup>. Cell groups confined to

micropatterned adhesive substrates (in the form of stripes or rings) demonstrated chiral cell alignment and movement<sup>8–10</sup>. Finally, on the single cell level, the processes of intracellular swirling, cortical flow, and cell migration can demonstrate left-right asymmetry<sup>11–15</sup>.

It is commonly believed that mechanisms underlying emergence of left-right asymmetry in diverse biological systems are based on the function of special chiral molecules<sup>16</sup>, and in particular the chiral cytoskeletal fibres<sup>17</sup>. Indeed, several classes of cytoskeletal proteins were shown to be involved in the processes of left-right asymmetry development listed above. While the asymmetric positioning of visceral organs depends on numerous cilia-related proteins<sup>18</sup> and attributed to cilia function in specialised cells located in the embryonic node

<sup>1</sup>Mechanobiology Institute, National University of Singapore, Singapore 117411, Singapore. <sup>2</sup>Department of Biomedical Engineering, National University of Singapore, Singapore 117583, Singapore. <sup>3</sup>Department of Physics, National University of Singapore, Singapore 117542, Singapore. <sup>4</sup>Courant Institute, New York University, New York, NY 10012, USA. <sup>5</sup>Department of Biology, New York University, New York, NY 10012, USA. <sup>6</sup>Department of Molecular Cell Biology, Weizmann Institute of Science, Rehovot 7610001, Israel. <sup>7</sup>These authors contributed equally: Wei Jia Goh, Xianbin Yong. ✉e-mail: [teeyehan@nus.edu.sg](mailto:teeyehan@nus.edu.sg); [alexander.bershadsky@weizmann.ac.il](mailto:alexander.bershadsky@weizmann.ac.il)

(left-right organiser), actin cytoskeleton-related proteins are involved in other examples of asymmetry. In particular, non-conventional myosins 1d and 1c are needed for asymmetric hindgut and male genitalia development in *Drosophila*<sup>5,6</sup>, and myosin 1d is sufficient to induce chirality in other *Drosophila* organs<sup>19</sup>. We previously proposed the role of formin family proteins in the development of actin cytoskeleton chirality<sup>11</sup> and several recent publications established the role of diaphanous formin in dextral snail chirality<sup>20,21</sup>, Daam formin in *Drosophila* hindgut and genitalia chirality<sup>22</sup>, and *Caenorhabditis elegans* CYK-1 formin in chiral cortical flow of *C.elegans* zygote<sup>23</sup>. Finally, some data indicated the involvement of the actin filament crosslinking protein  $\alpha$ -actinin1 in emergence of chirality in cultured individual cells and multi-cell spheroids<sup>11,24</sup>. However, how intrinsic chirality of the actin filaments<sup>25</sup> is translated in vivo into chirality of cells, and whether this is sufficient to explain the emerging of chirality in multicellular groups such as tissue and organs remains obscure.

In particular, it is unknown whether left-right asymmetry emerges as a result of the activity of a single chiral determinant such as myosin 1d<sup>19</sup> (perhaps different proteins in different systems) or is mediated by coordinated activities of a group of proteins with complementary functions. Here, we addressed this question by systematic investigation of the involvement of major actin-associated proteins in the regulation of left-right asymmetry of the actin cytoskeleton in individual cells. In the course of this analysis, we examined the effects of depletion of chirality regulators found in previous studies, namely formins, myosin 1c and 1d, and  $\alpha$ -actinin1. We show that, even in this simple system, the chiral swirling of actin depends on the functions of several groups of actin regulators. We reveal several types of such regulators: depletion of some of them reduced or abolished chirality, while depletion of others reversed the direction of chirality.

The discovery of numerous regulators of chiral morphogenesis in individual cells allowed us to perform detailed comparison between factors affecting individual and collective cell chirality. It was previously unclear whether chiral asymmetry of the actin cytoskeleton in individual cells is related to emergence of collective chirality in cell groups. Here, we found that the majority of treatments affecting the asymmetric self-organisation of the actin cytoskeleton in individual cells also affected the asymmetric alignment of cell groups. In particular, all factors that reversed direction of cytoskeletal chirality in individual cells also reversed the direction of chiral cell alignment in cell groups. Altogether our findings provide the background for the future understanding of the processes of emerging left-right asymmetry in tissues and organs.

## Results

### Assessment of chiral organisation of radial fibres

We have previously shown that human fibroblasts (HFF) plated on fibronectin-coated circular islands with an area of 1800  $\mu\text{m}^2$  formed a chiral pattern of organisation of actin filament bundles. Radial actin fibres originating from focal adhesions at the cell edge eventually tilted to the right from the axis connecting the focal adhesion with the cell centre. This coincided with the development of chiral swirling – an anti-clockwise bias in centripetal movement of transverse fibres along the tilted radial actin fibres<sup>11</sup> (Supplementary Movie 1). To quantitatively investigate the molecular requirements for actin cytoskeleton chiral self-organisation, we introduced a quantitative method of assessment of radial fibre tilting (Fig. 1a to h, and Supplementary Fig. 1). First, we segmented the radial fibres using a deep-learning network (Unet-ResNet50) (Fig. 1a, b, e and f, and Supplementary Fig. 1a). The identified radial fibres are presented as having similar brightness (grey values) irrespective to their fluorescence intensity in the original image (Supplementary Fig. 1b). The segmented images were further binarized and skeletonised. Second, the image of circular cell was subdivided into eight concentric annular rings located at given distances from the cell edge (Fig. 1c and g, and Supplementary Fig. 1c). The mean tilt of

radial fibre segments located in each ring was calculated for each cell (Fig. 1d and h, and Supplementary Fig. 1c). The radial fibre pattern for the cell population was then characterised by the curve showing the mean tilt of radial fibre segments (averaged over all cells) as a function of their distance from the cell edge (Fig. 1i). In addition, to further characterise the variability between cells, we compared histograms characterising the distribution of the average radial fibre tilt in the single annulus located between 6–10 or 8–12 microns from the cell edge (Fig. 1i to k). Details of the methodology are described in methods section.

### Chiral pattern formation requires mDia1, Arp2/3 and cofilins 1&2

We evaluated the effects of the knockdowns of 10 of 15 formin family members expressed in fibroblasts on chiral organisation of radial fibres (Supplementary Fig. 2a to f). Knockdown of diaphanous-related formin, mDia1, did not prevent the formation of either radial or transverse fibres, but abolished the tilting of the radial fibres (Fig. 1j). As a result, mDia1 depleted cells exhibited a radially symmetric organisation of the actin cytoskeleton (Fig. 1j and l). The inhibitory effect of mDia1 knockdown on chiral actin pattern formation can be rescued by expression of exogenous mDia1-GFP construct (Fig. 1k and l, and Supplementary Fig. 2d and Supplementary Table 1, lines 1–3). The statistical analysis of the results of knockdown of several other abundant formins revealed that their effect on chirality can be classified into two groups (Supplementary Fig. 2b and c, and Supplementary Table 1, lines 124–133). FMNL2, FHOD3 and Daam1 knockdowns reduced the degree of actin cytoskeleton chirality, albeit not to such extent as knockdown of mDia1 (Supplementary Fig. 2b and Supplementary Table 1, lines 124–127 and 134–136). The knockdowns of other examined formins (FMN2, mDia2, mDia3, INF2, FHOD1 and Daam2) did not have an apparent effect on chirality (Supplementary Fig. 2c and Supplementary Table 1, lines 128–133).

We further studied the cell orientation in multicellular microcultures on rectangular adhesive islands with a 1:2 aspect ratio (300  $\times$  600  $\mu\text{m}$ ). At 48 h following plating, the cells approached confluence and aligned mainly along the diagonal of the rectangles as seen from the orientation of nuclei or local average cell orientation characterised by nematic directors on phase-contrast images<sup>26</sup> (Fig. 2a to c and Supplementary Movie 2). Thus, each rectangular microculture was characterised by the mean angle between local nematic directors and the long axis of the rectangle (Fig. 2b and d). In complementary set of measurements, the long axes of elliptical nuclei were used instead of nematic directors (Fig. 2c and d). In control microcultures, the cells orientation was chiral so that the distribution of the values of angles characterising individual rectangles was asymmetric (Fig. 2d). In other words, the cells on the rectangular pattern preferentially aligned into a *I*-orientation rather than a *N*-orientation (when observed from above). We also examined rectangles with other aspect ratios and found that the 300  $\times$  600  $\mu\text{m}$  size was optimal for asymmetric alignment of microcultures (Supplementary Fig. 3).

We found that knockdown of mDia1 converted the distribution of the angles characterising individual microcultures into bimodal distribution (Fig. 2d and Supplementary Fig. 4), meaning that mDia1 knockdown cells in the rectangular microcultures co-oriented in *I* or *N* fashion with equal probability. Examining the knockdowns of other formins revealed that FMNL2, FHOD3, Daam1 knockdown significantly reduced the mean angles of nematic directors (Supplementary Fig. 2g and Supplementary Table 1, lines 148–150), while INF2 knockdown increased it (Supplementary Fig. 2h and Supplementary Table 1, line 154). Knockdowns of other formins – FMN2, mDia3, mDia2, FHOD1 and Daam2, did not produce significant effect (Supplementary Fig. 2h and Supplementary Table 1, lines 151–153 and 155–156).

We further assessed the effect of the knockdowns of other major regulators of actin polymerisation<sup>27</sup>. The suppression of the actin-

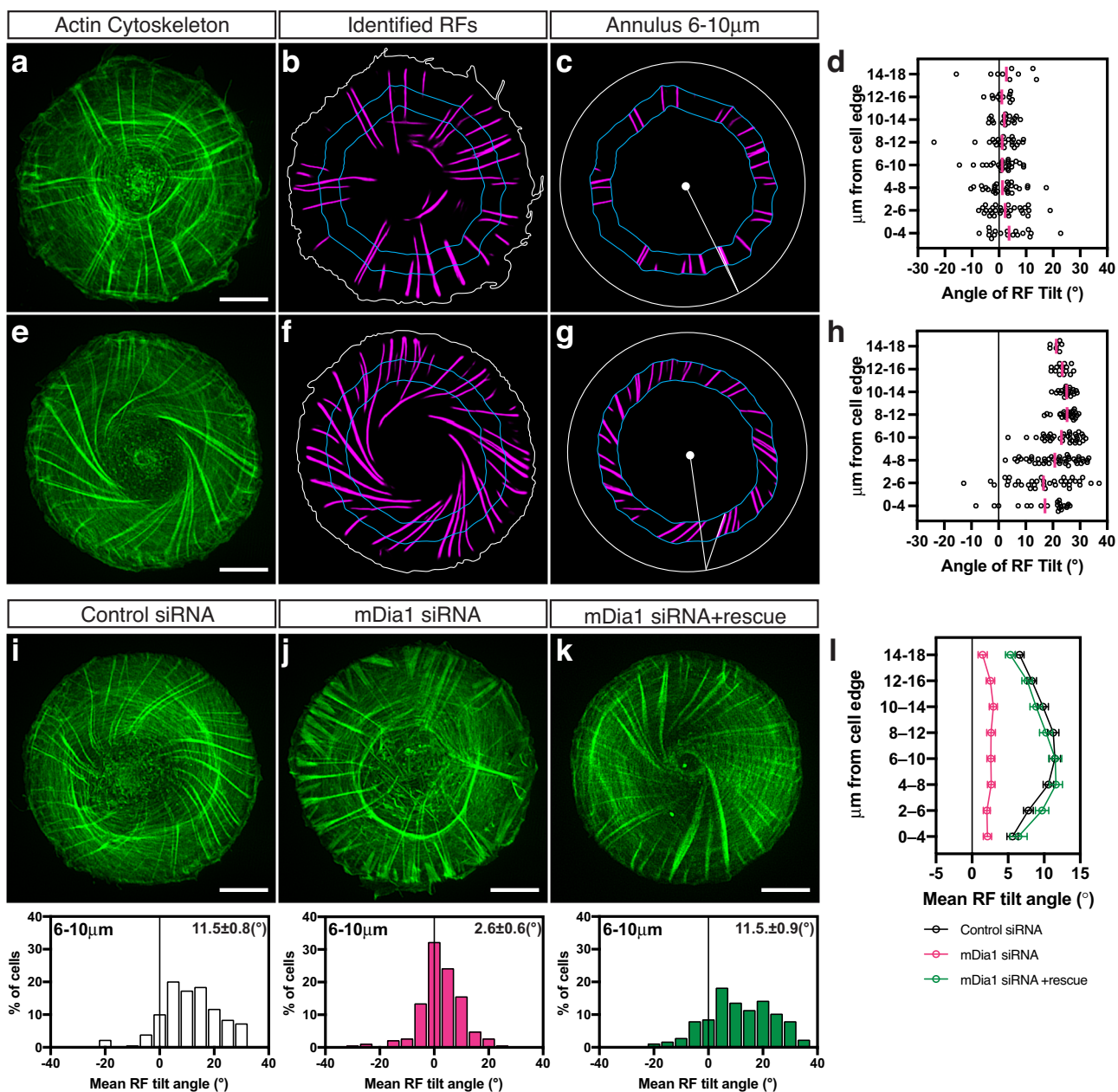


**Fig. 1 | Quantification of radial fibre tilt reveals a decrease in actin cytoskeleton chirality in mDia1 knockdown cells.** **a–h** Illustration of measurements of the radial fibre (RF) tilt. Selected fluorescence images of actin cytoskeleton in a radial (**a**) and a chiral (**e**) cells from the population of control cells fixed and stained with phalloidin at 6 h after plating. **b, f** RFs were identified by deep-learning procedure. Pair of cyan lines located at the 6 and 10  $\mu\text{m}$  distances from the cell edge (white line) delineate the concentric belt that we termed the 6–10  $\mu\text{m}$  annulus. Other annuli are defined in a similar way. The tilts of all RF segments in the annuli located at given distance from the cell edge were measured as shown in (**c**) and (**g**). In these measurements, the cell edge was replaced with best fit circle (white line) with the centre at the cell centroid (white dot). See Methods. See also Supplementary Fig. 1c. **d, h** The tilt values in all eight annuli of cells (**a**) and (**e**) are shown in (**d**) and (**h**) respectively. Each symbol represents the tilt angle of an individual RF segment. The mean of tilt values at each given distance from the cell edge are shown in magenta. **i–l** Effect of mDia1 knockdown and rescue on RF tilt. **i–k** Typical examples of actin organisation visualised by phalloidin-staining of cells transfected with control siRNA (**i**), mDia1 siRNA (**j**) and mDia1 siRNA plus mDia1 full-length plasmid (**k**) 6 h following cell plating on circular patterns. The histograms in (**i–k**) show the distribution of mean RF tilt in the 6–10  $\mu\text{m}$  annulus in cells under corresponding conditions (white bars – control siRNA-treated cells, magenta bars – mDia1 siRNA-treated cells, green bars – mDia1 siRNA-treated cells rescued by mDia1 plasmid). Histograms and mean $\pm$ SEM values (in **i–k**) are based on measurements of 179 control cells, 186 mDia1 knockdown cells, and 177 mDia1 knockdown cells rescued by mDia1 plasmid overexpression. **l** Graphs of average RFs tilts (mean $\pm$ SEM) as a function of the distance of annuli from the cell edge (the same cell samples as **i–k**). Scale bars, 10  $\mu\text{m}$  (**a, e, i–k**). For statistical analysis, see Supplementary Table 1, lines 1–6.

nucleating Arp2/3 complex via the knockdown of its major component ARPC2 (Supplementary Fig. 5f), resulted in the inhibition of actin cytoskeleton chirality as evident by the reduction in radial fibre tilt angle (Supplementary Fig. 5a and b, and Supplementary Table 1, line 167). Otherwise, the overall effect of ARPC2 downregulation on the actin cytoskeleton appearance in these experiments was relatively mild and cell spreading was not impaired.

The double knockdown of actin depolymerising proteins, cofilins 1 and 2 (Supplementary Fig. 5g), led to a pronounced inhibition of actin chirality (Supplementary Fig. 5c and d, and Supplementary Table 1, line

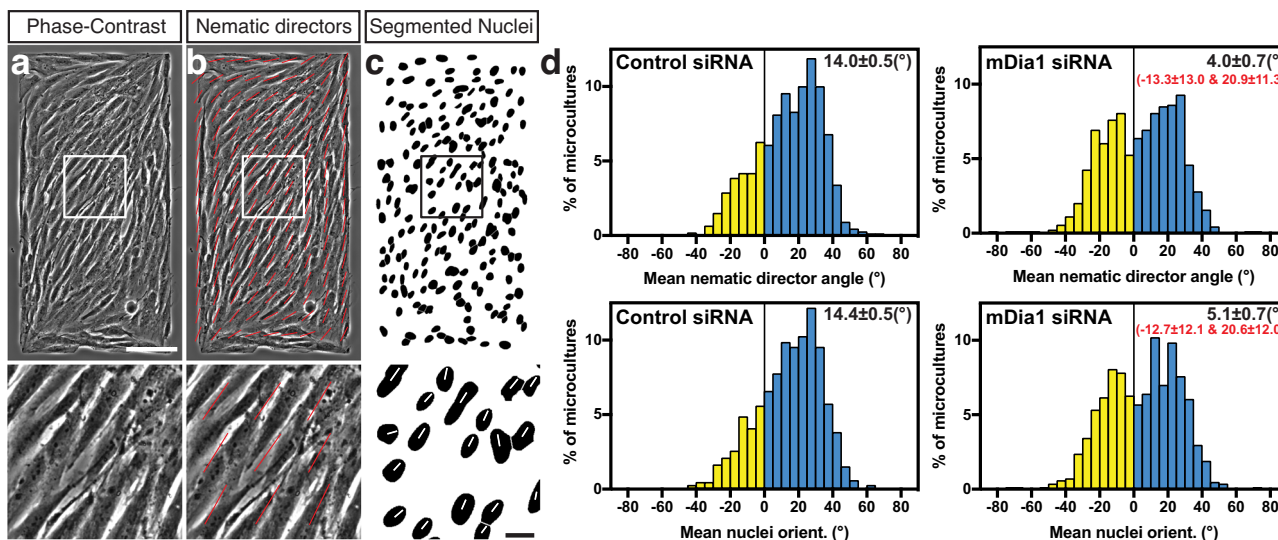


**Fig. 2 | Quantification of chiral alignment of cells in confined cell groups reveals a decrease of chirality in mDia1 knockdown cells.** **a** Phase-contrast image of cells 48 h following plating on rectangular adhesive pattern ( $300 \times 600 \mu\text{m}$ ). **b** Image shown in (a) overlaid with red lines representing average local orientation of cells (nematic directors). **c** Segmented Hoechst 33342-stained nuclei of cells shown in (a). Boxed areas in (a to c) are shown at higher magnification in the lower row. **d** Histograms showing distributions of the values of mean nematic directors angles (upper row) and mean nuclei orientation angles (lower row) characterising individual microcultures at 48 h after plating. The histograms were built based on

average nematic director angles from 1530 control and 894 mDia1 knockdown microcultures, and average nuclei orientation angles from 1521 control and 844 mDia1 knockdown microcultures. Mean  $\pm$  SEM values are indicated at the top right corner of each histogram. Negative and positive values are coloured in yellow and cyan respectively. Note that for mDia1 knockdown cells both nematic directors and nuclei orientation distribution are bimodal as determined by fitting it as a sum of 2 Gaussian distributions (see Supplementary Fig. 4); the values of the respective two means ( $\pm$ SD) are indicated in red. Scale bars, 100  $\mu\text{m}$  (upper row); 20  $\mu\text{m}$  (lower row). For statistical analysis, see Supplementary Table 1, lines 7–14.

169). The knockdown of related protein, actin depolymerising factor (ADF) (Supplementary Fig. 5g), diminished anti-clockwise actin cytoskeleton chirality slightly (Supplementary Fig. 5d and e, and Supplementary Table 1, line 172), but combined knockdown of ADF and cofilins 1 and 2 completely abolished cell chirality resulting in symmetrical distribution of radial fibre tilt with a zero mean value (Supplementary Fig. 5d and e, and Supplementary Table 1, lines 173 and 177). Re-introduction of only cofilin-1 to the cofilins 1 and 2 depleted cells was sufficient to restore anticlockwise chirality of the cell (Supplementary Fig. 5d, e and g, and Supplementary Table 1, line 171).

Investigation of the effects of depletion of ARP2/3 and cofilins/ADF family members on collective cell alignment in rectangular microculture revealed that, unlike the knockdown of mDia1, the knockdown of ARPC2, cofilins and ADFs only slightly affected the degree of chiral orientation of cells in microcultures on rectangles (Supplementary Fig. 5h and Supplementary Table 1, lines 179–182). It can be explained by assumption that knockdowns of ARPC2 and cofilins delayed the anti-clockwise chirality onset but not suppressed it entirely.

Lastly, the knockdowns of Ena/VASP family activators of actin filament elongation, VASP and Mena, moderately albeit significantly reduced the development of asymmetric actin pattern in individual cells (Supplementary Fig. 6a to e, and Supplementary Table 1, lines 188–189) but did not perturb the chiral alignment of cell collectives in microcultures (Supplementary Fig. 6f and Supplementary Table 1, lines 192–193).

#### Perturbing actin polymerisation can alter chirality direction

While depletion of mDia1, ARPC2, or cofilins reduced the asymmetry of actin pattern, the manipulations of several other actin-associated proteins or actin pharmacological perturbations reversed the direction of chirality (Fig. 3). Profilins are abundant actin-monomer sequestering proteins which can either augment or inhibit actin polymerisation, depending on their biological context<sup>28</sup>. We found that the siRNA-mediated knockdown of profilin 1 (Supplementary Fig. 7a to c)

reversed the direction of actin swirling in cells, resulting in sinistral chirality pattern (Fig. 3b and f, and Supplementary Movie 3). This effect can be rescued by the expression of exogenous human profilin 1 (Fig. 3c and f, and Supplementary Fig. 7b and Supplementary Table 1, line 17). The curve showing the average tilt of radial fibres as a function of distance from the cell edge in profilin 1 siRNA-treated cells was approximately a mirror-image of the curve for control cells (Fig. 3f). In our experiments, siRNA transfection only partially inhibited the expression of profilin 1 protein ( $0.38 \pm 0.17$  fold change) (Fig. 5h and Supplementary Fig. 7b and c) which, however, was sufficient to reverse chirality direction. At the same time, depletion of ~90% of endogenous profilin 2 (Supplementary Fig. 7b) not only did not reverse chirality direction but increased the degree of anti-clockwise chirality in terms of radial fibre tilt (Fig. 3d and f and Supplementary Table 1, line 18).

Capping proteins bind to the barbed end of actin filaments and interferes with both polymerisation and depolymerisation<sup>27</sup>. Knockdown of CapZ $\beta$ , a subunit of capping protein CapZ, (Supplementary Fig. 7d) resulted in the reversal of direction of radial fibres tilting so that sinistral actin pattern was formed (Fig. 3e and f).

Of note, even though the effects of knockdowns of CapZ $\beta$ , mDia1 and cofilins 1&2 were reproducible in experiments where actin pattern was quantified in fixed phalloidin-stained cells, they were less pronounced in experiments where actin was visualised by expression of LifeAct fused with either GFP or mRuby fluorescent proteins. The reason for these discrepancies is unknown; it might be related to some effects of LifeAct on actin polymerisation<sup>29</sup>.

By screening of actin polymerisation affecting drugs, we found that latrunculin A, which sequester G-actin monomer and depolymerise F-actin<sup>30</sup>, when applied at low concentration (20 nM), effectively reversed the direction of chirality – inducing sinistral actin pattern (Fig. 3g). The time course of chirality development in the presence of latrunculin A was the same as in control, while the average tilt of the radial fibres was of similar magnitude but opposite in direction as compared to control (Fig. 3h). The effect of latrunculin A was readily seen in both phalloidin-stained fixed cells and LifeAct-labelled live cells.

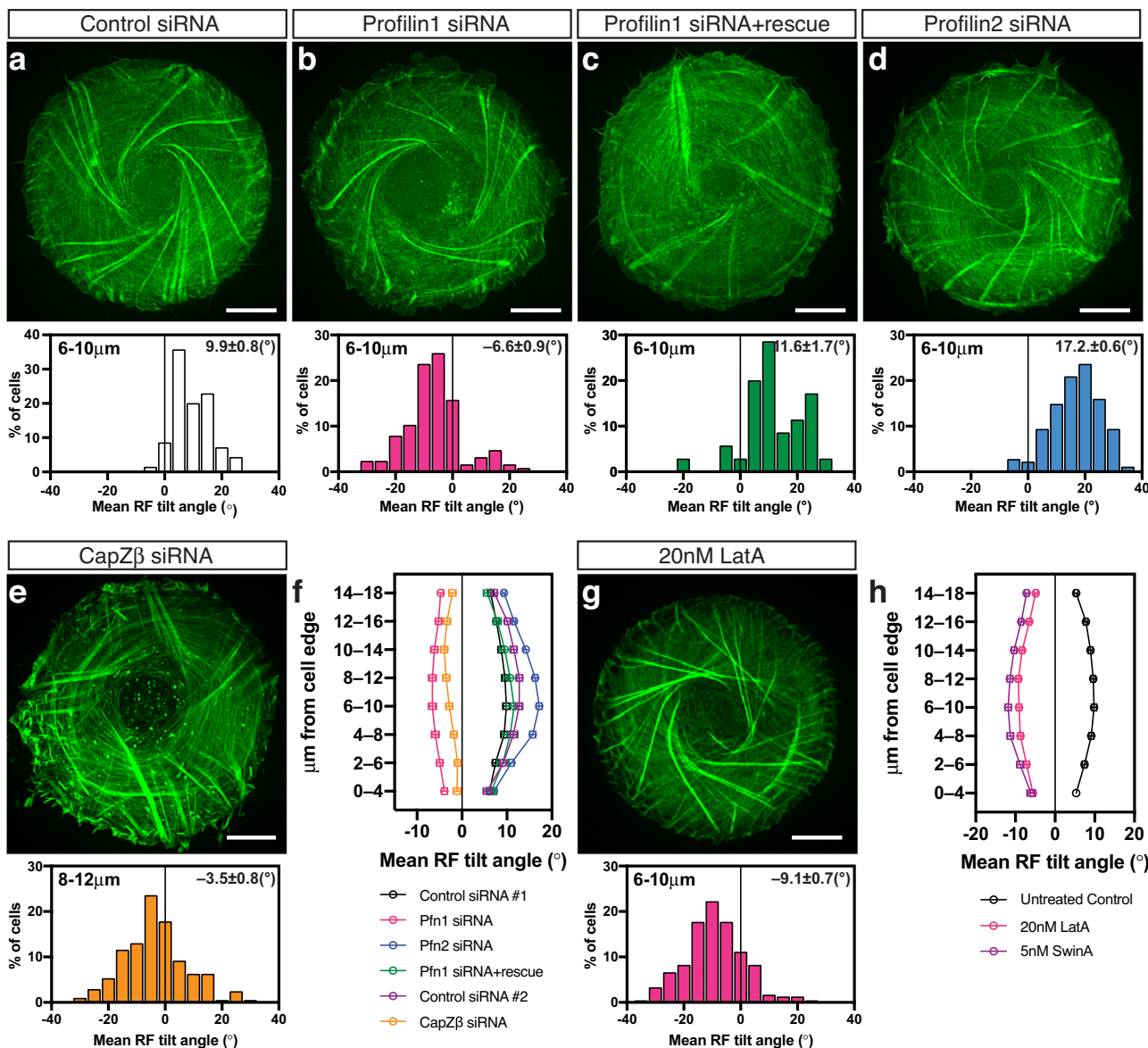


**Fig. 3 | Genetic knockdowns and pharmacological treatments reversing the direction of the actin cytoskeleton chirality.** **a–d** Typical examples of actin organisation visualised by LifeAct-GFP in control siRNA (**a**), profilin 1 (Pfn1) siRNA (**b**), profilin 1 siRNA plus Pfn1 full-length plasmid (**c**) and profilin 2 (Pfn2) siRNA (**d**) transfected cells. The histograms in (**a–d**) show the distribution of mean RF tilt in the 6–10 μm annulus in cells treated as indicated and imaged for 12–16 h after plating. Histograms and mean  $\pm$  SEM values are based on measurements during the entire period of imaging of 70 control cells, 127 Pfn1 knockdown cells, 35 Pfn1 knockdown cells rescued by co-transfection with full-length Pfn1 plasmid and 182 Pfn2 knockdown cells. **e** Typical example of actin organisation visualised by phalloidin-staining in CapZβ siRNA-transfected cells fixed at 6 h after cell plating. Histogram under the image shows the distribution of mean RF tilt in the 8–12 μm annulus in cells at 6 h after plating. Histogram and mean  $\pm$  SEM value are based on 208 cells. **f** Average values of RF tilts (mean  $\pm$  SEM) as a function of the distance of annuli from the cell edge for untreated control cells ( $n = 274$ ), 20 nM LatA-treated cells ( $n = 243$ ), and 5 nM swinholide A (SwinA)-treated cells ( $n = 153$ ) at 6 h after cell plating. Colour coding in histograms (**b–e**) and (**g**) correspond to those indicated in graphs (**f**) and (**h**) respectively. Scale bars, 10 μm (**a–e** and **g**). See also Supplementary Movie 3. For statistical analysis, see Supplementary Table 1, lines 15–29.

annuli from the cell edge for profilins and CapZβ experiments (the same cell samples as **a–e**). Control siRNA #1 and #2 represent the 70 and 146 control cells used in experiments with profilins and CapZβ respectively. **g** Typical example of actin organisation visualised by phalloidin-labelling in cells treated with 20 nM of latrunculin A (LatA). Histogram under image shows the distribution of mean RF tilt in the 6–10 μm annulus of cells fixed at 6 h after cell plating. Histogram and mean  $\pm$  SEM value are based on 243 cells. **h** Average values of RF tilts (mean  $\pm$  SEM) as a function of the distance of annuli from the cell edge for untreated control cells ( $n = 274$ ), 20 nM LatA-treated cells ( $n = 243$ ), and 5 nM swinholide A (SwinA)-treated cells ( $n = 153$ ) at 6 h after cell plating. Colour coding in histograms (**b–e**) and (**g**) correspond to those indicated in graphs (**f**) and (**h**) respectively. Scale bars, 10 μm (**a–e** and **g**). See also Supplementary Movie 3. For statistical analysis, see Supplementary Table 1, lines 15–29.

Addition of latrunculin A reversed the direction of swirling in cells with an established anti-clockwise (dextral) actin cytoskeleton (Supplementary Movie 4). These effects were rapid and became evident within 1–2 h following latrunculin A addition. Washing out of latrunculin A resulted in rapid return to anti-clockwise actin swirling (Supplementary Movie 5). Among other actin polymerisation affecting drugs, the actin filament severing and dimer forming drug swinholide A<sup>31</sup>, at 5 nM, produced the same reversing effect on chirality direction as latrunculin A (Fig. 3h). The fast effects of latrunculin A on chirality direction suggest that its

action does not depend on any transcriptional effects. Indeed, we showed that chiral tilting of radial fibres and anti-clockwise actin swirling, as well as reversion of direction of these processes upon latrunculin A treatment can occur in enucleated cells (Supplementary Fig. 8 and Movie 6). The experiment with enucleated cells also showed that tilting of the radial fibres does not depend on their possible interaction with the nucleus.

The genetic knockdowns and drug treatments that changed the direction of chirality of the actin cytoskeleton in individual cells

induced corresponding changes in the chirality of alignment in microcultures on a rectangular pattern. Depletion of profilin 1 or CapZ $\beta$ , or treatment with latrunculin A or swinholide A resulted in preferential cell alignment in the direction mirror-symmetrical to that of control cells (Fig. 4a and b). In all these cases, the average orientation of multicellular groups in rectangles was tilted at negative angles relative to the long axis of the rectangle (Fig. 4c and Supplementary Fig. 7e). Similar to results in individual cells, the knockdown of profilin 2 did not change the direction of cell alignment as compared to control (Fig. 4c and Supplementary Fig. 7e). Therefore, the effect of treatments affecting the direction of chirality in individual cells strongly correlates with their effect on the chirality of cell alignment in microcultures.

Altogether, the results presented in this section showed that human fibroblasts can demonstrate two types of actin cytoskeleton chirality – anti-clockwise, observed in wildtype cells, and clockwise, observed upon knockdowns of some actin regulating proteins and pharmacological treatments. Such situation is typical for some living systems, for example, pond snails demonstrate dextral (prevalent) and sinistral (rare) coiling. Since formin mDia1 is shown to be required for dextral anti-clockwise chirality (Figs. 1l to 1 and 5d and g), we examined its possible involvement in establishing sinistral clockwise chirality induced by profilin 1 knockdown and latrunculin A treatment. The data presented in Fig. 5 show that while knockdown of mDia1 suppressed the dextral chirality of fibroblast, it does not significantly affect the development of sinistral chirality (Supplementary Table 1, lines 48–49).

#### Alteration of chirality direction is $\alpha$ -actinin1-dependent

Overexpression of actin crosslinking protein  $\alpha$ -actinin1 resulted in the reduction of cell chirality and reversal of the direction of actin cytoskeleton swirling in a fraction of transfected cells in agreement with our previous study<sup>11</sup> (Fig. 6a and b, and Supplementary Fig. 9a). The effect of chirality reversal upon overexpression of  $\alpha$ -actinin1 was also evident on multicellular microcultures confined to rectangular pattern (Fig. 6c and d, and Supplementary Fig. 9e). Overexpression of  $\alpha$ -actinin4 largely reduced the fraction of chiral cells, while overexpression of another actin crosslinker, Filamin A, had no effect (Fig. 6b and Supplementary Fig. 9, b and c and Supplementary Table 1, lines 57, 58 and 61). Neither  $\alpha$ -actinin1 knockdown alone nor the expression of truncated  $\alpha$ -actinin construct, ABDdel-actinin<sup>32</sup>, which interfered with the actin crosslinking activity of  $\alpha$ -actinin, changed the chirality direction in individual cells and cell groups (Fig. 6e to h, Fig. 7a and e, and Supplementary Fig. 9d and e).

In view of the involvement of  $\alpha$ -actinin1 in reversal of cell chirality in these and other study<sup>24</sup>, we further investigated the combined effect of  $\alpha$ -actinin1 loss-of-function and experimental manipulations, which reversed chirality direction. The average tilt of RFs in cells with double knockdowns of profilin 1 and  $\alpha$ -actinin1 does not statistically significantly differ from that of control (Fig. 7b and Supplementary Table 1, lines 83–85). Double knockdowns of CapZ $\beta$  and  $\alpha$ -actinin1 resulted in dextral anti-clockwise chirality (Fig. 7c and Supplementary Table 1, lines 89–91). Latrunculin A treatment of  $\alpha$ -actinin1 knockdown cells or ABDdel-actinin expressing cells (Fig. 7d and Supplementary Fig. 9f) resulted in broad symmetrical distribution of radial fibre tilt with the mean close to zero (Supplementary Table 1, lines 97 and 218). At least for  $\alpha$ -actinin1 knockdown cells treated with latrunculin A, this distribution can be approximated by a sum of 2 Gaussian distributions (Supplementary Fig. 4b). Thus, reversal of chirality by depletion of either profilin 1 or CapZ $\beta$ , or latrunculin treatment requires  $\alpha$ -actinin1 function. In microcultures, knockdown of  $\alpha$ -actinin1 similarly prevents the reversal of chirality upon profilin 1 (Fig. 7f and Supplementary Table 1, lines 101–103) or CapZ $\beta$  (Fig. 7g and Supplementary Table 1, lines 104–106) depletion, but not upon latrunculin A treatment (Fig. 7h and Supplementary Table 1, lines 107–109).

Since several studies have clearly demonstrated the importance of myosin 1c and 1d in the chiral morphogenesis of *Drosophila* organs<sup>5,6,19</sup>, we checked whether human myosin 1c and 1d are involved in individual and collective chirality development in our experimental systems. The differences between control and myosin 1c or myosin 1d knockdown cells (Supplementary Fig. 10d and e) in the development of the chiral actin pattern in individual cells were not statistically significant (Supplementary Fig. 10a to c and Supplementary Table 1, lines 219–220). However, chirality of collective alignment in microcultures of myosin 1c knockdown cells was significantly more pronounced than in control microcultures (Supplementary Fig. 10f and Supplementary Table 1, line 223). Thus, myosin 1c may participate in chirality regulation in our experimental system while such function of myosin 1d was not revealed. Of note, the human myosins 1c and 1d are not the exact homologs of their *Drosophila* counterparts with similar names<sup>33</sup>, however, human myosin 1c did demonstrate chiral interaction with the actin filaments in an *in vitro* assay<sup>34</sup>.

In order to assess whether any of the knockdown effects observed above could be attributed to an associated alteration in the expression level of other proteins involved in chirality regulation, we examined the transcriptional profile of cells depleted of major proteins strongly associated with chirality phenotype (Supplementary Fig. 11a). We found that, with few exceptions, knockdowns of the members of this group of proteins (mDia1, ARPC2, cofilins 1&2, CapZ $\beta$ , profilin 1, and  $\alpha$ -actinin1) only slightly, if at all, affected the expressions of other members of the group. Moreover, some increase in  $\alpha$ -actinin1 transcriptional level upon knockdowns of mDia1 or cofilins 1&2 (Supplementary Fig. 11a) was not accompanied by an increase in its protein level (Supplementary Fig. 11b and c). These data suggested that phenotypic changes observed upon knockdown of these proteins are not mediated by transcriptional regulation of the expression of other members of this group. This is consistent with the apparent transcription-independent effect on chirality observed in latrunculin A-treated enucleated cells, as mentioned above (Supplementary Fig. 8).

#### Correlation between individual and collective cell chirality

Altogether, in our experiments, we characterised the effects of 35 different pharmacological and genetic manipulations on the emergence of left-right actin cytoskeleton asymmetry in individual confined cells, as well as on chiral cell alignment of confined multicellular groups. To analyse the interrelationship between the establishment of left-right asymmetry in these two systems, we plotted the average angle between the nematic directors characterising the alignment of cells in cell groups versus the average tilt of radial fibre segments located between 6–10 microns from the cell edge (Fig. 8 and Supplementary Table 2). In spite of some discrepancies, as mentioned earlier, the correlation between these two parameters was highly significant (Pearson correlation coefficient,  $r = 0.8104$ ,  $p < 0.0001$ ) (Fig. 8). Ranking the data in ascending order also revealed a strong correlation between these two parameters (Spearman's rank correlation coefficient,  $r = 0.7081$ ,  $p < 0.0001$ ) (Supplementary Fig. 12a and Supplementary Table 2). Moreover, such presentation of the data clearly shows the correlation between effects of knockdown of majority of formin family members on individual and collective cell chirality (Supplementary Fig. 12b). Altogether these data demonstrate the role of actin cytoskeleton asymmetry in individual cells in the establishment of collective asymmetry of cell alignment in cell groups.

#### Chirality of actin cytoskeleton in confined elliptical cells

In view of the obvious correlation between the chirality of actin cytoskeleton swirling in individual cells and the chiral nematic orientation of elongated cells in cell groups, we decided to check whether actin cytoskeleton in elongated cells could demonstrate chiral

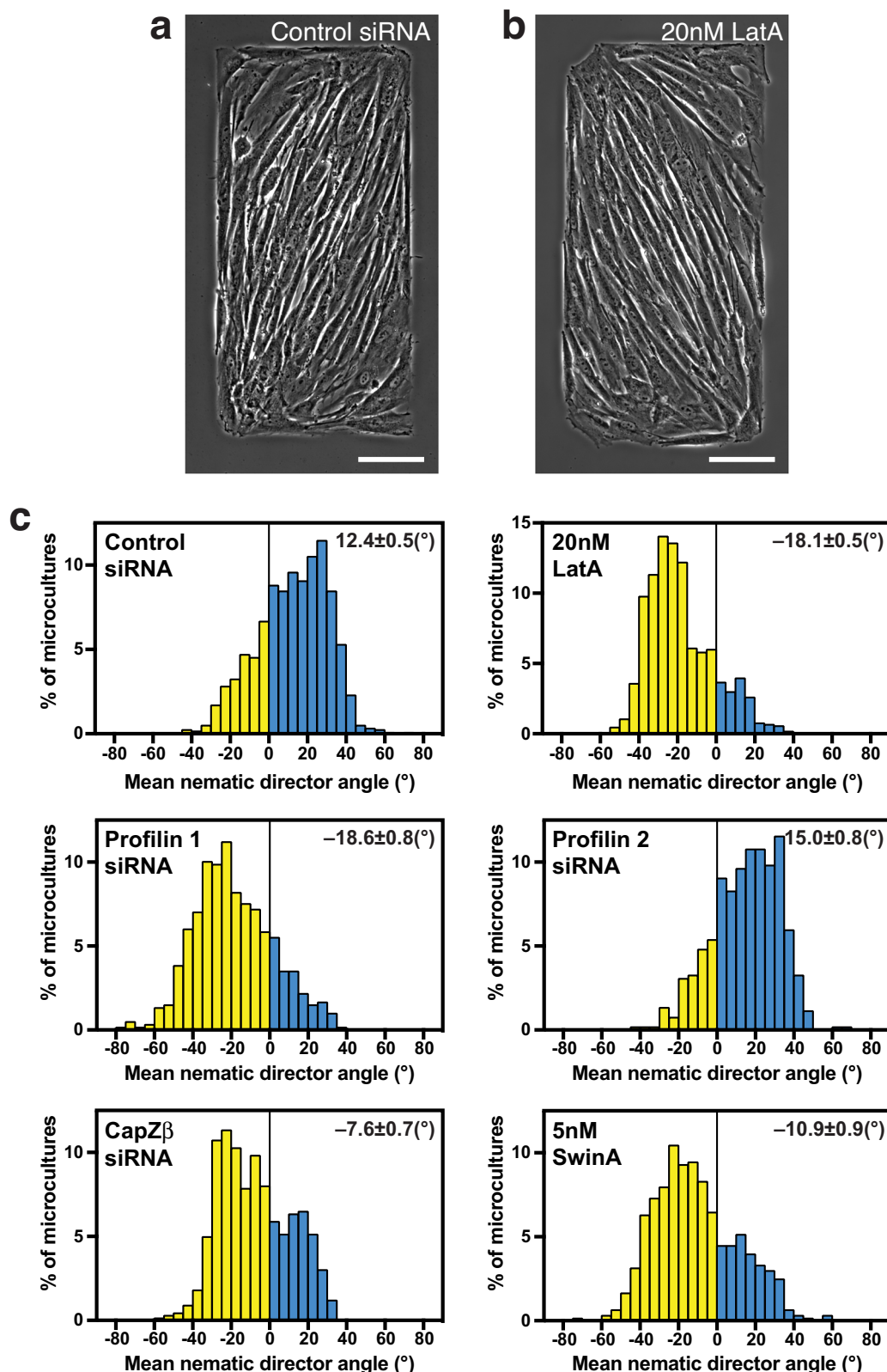
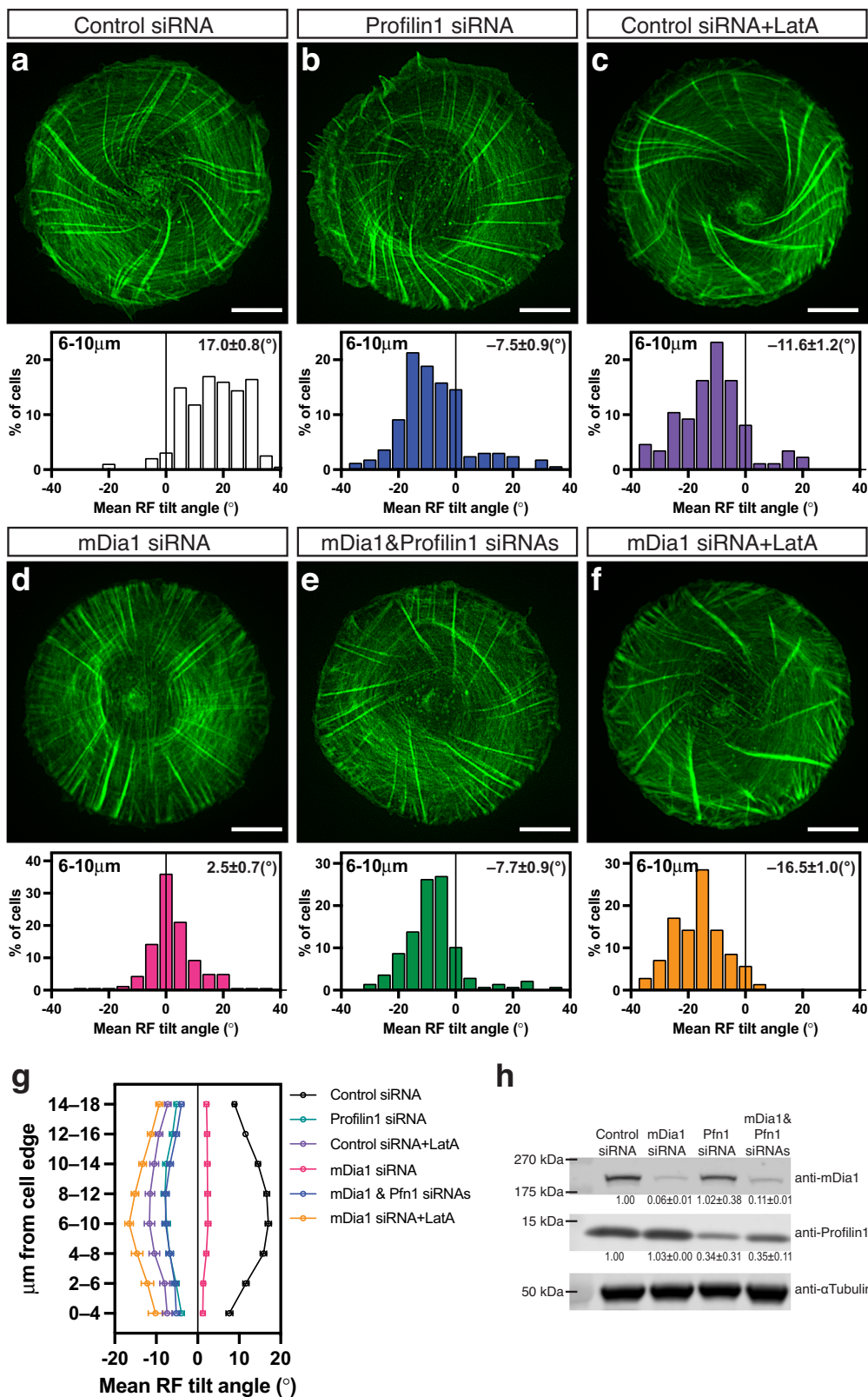


**Fig. 4 | Knockdowns of profilin 1 and CapZ $\beta$  and treatments with latrunculin A and swinholide A reverse the sign of cell orientation angle in microcultures confined to rectangular micropatterns.** **a, b** Typical phase-contrast images showing dextral alignment of control cells (**a**) and sinistral (reversed) alignment of latrunculin A (LatA)-treated cells (**b**) 48 h following plating on rectangular adhesive pattern. **c** Histograms show distributions of the values of mean nematic directors characterising individual microcultures on rectangles for cells treated as indicated.

Negative and positive values are coloured in yellow and cyan respectively. Mean  $\pm$ SEM values are indicated at the top right corner of each histogram. The histograms were built based on average local cell orientation (nematic directors) values from 1168 control, 1031 LatA-treated, 597 Pfn1 knockdown, 519 Pfn2 knockdown, 661 CapZ $\beta$  knockdown and 602 swinholide A (SwinA)-treated microcultures. See also Supplementary Fig. 7. Scale bars, 100  $\mu$ m (**a, b**). For statistical analysis, see Supplementary Table 1, lines 30–40.



organisation. To this end, we plated individual cells on elliptical micropatterns with different aspect ratios (Fig. 9 and Supplementary Fig. 13). On circular patterns, the actin cytoskeleton evolves from the system of radial fibres through the chiral tilting of radial fibres and anti-clockwise swirling of actin flow to the linear organisation of parallel stress fibres (actin bundles containing myosin filaments and associated with focal adhesions at both ends) filling the entire cell<sup>11</sup>. During

spreading on elliptical micropatterns, the growth of radial fibres and focal adhesions were stronger at the vertex regions characterised by higher curvature than at the sides of the ellipses (Supplementary Fig. 13 and Movie 7). The dynamic observations of cells revealed a chiral pattern of radial fibres and anti-clockwise swirling, similar to that in a circular cell but geometrically transformed to accommodate the elliptical shape (Fig. 9g and Supplementary Movie 7). Sometimes, even

**Fig. 5 | Formin mDia1 is dispensable for the development of clockwise (sinistral) actin cytoskeleton chirality in profilin 1 knockdown and latrunculin A-treated cells.** **a–f** Typical examples of actin organisation, at 6 h following seeding on micropatterns, in cells transfected with control siRNA (**a**, **c**), profilin 1 (Pfn1) siRNA (**b**), mDia1 siRNA (**d**, **f**) and mDia1&profilin 1 siRNAs (**e**). 20 nM latrunculin A (LatA) was added to control (**c**) or mDia1 knockdown (**f**) cells 10 min after cell attachment. Actin was visualised by phalloidin-staining after fixation. The histograms below each image show the distribution of average RF tilt in the 6–10  $\mu$ m annulus in cells under corresponding conditions. **g** Average values of RF tilts (mean  $\pm$  SEM) as a function of the distance of annuli from the cell edge. Histograms and

mean  $\pm$  SEM values (in **a** to **g**) are based on measurements of 194 control siRNA cells, 164 profilin 1 knockdown cells, 86 LatA-treated control siRNA cells, 161 mDia1 knockdown cells, 137 mDia1&profilin 1 double knockdown cells and 70 LatA-treated mDia1 knockdown cells. Scale bar, 10  $\mu$ m (**a**–**f**). **h** Western blot showing mDia1 (upper row) and profilin 1 (middle row) protein level in cells treated with scrambled (control), anti-mDia1, anti-profilin 1 or anti-mDia1 plus anti-profilin 1 siRNAs;  $\alpha$ -tubulin (bottom row) was used as loading control. Quantification of fold change relative to control was indicated as mean  $\pm$  SD values for 2 experiments. Colour coding in histograms (**b**–**f**) correspond to those indicated in graph (**g**). See

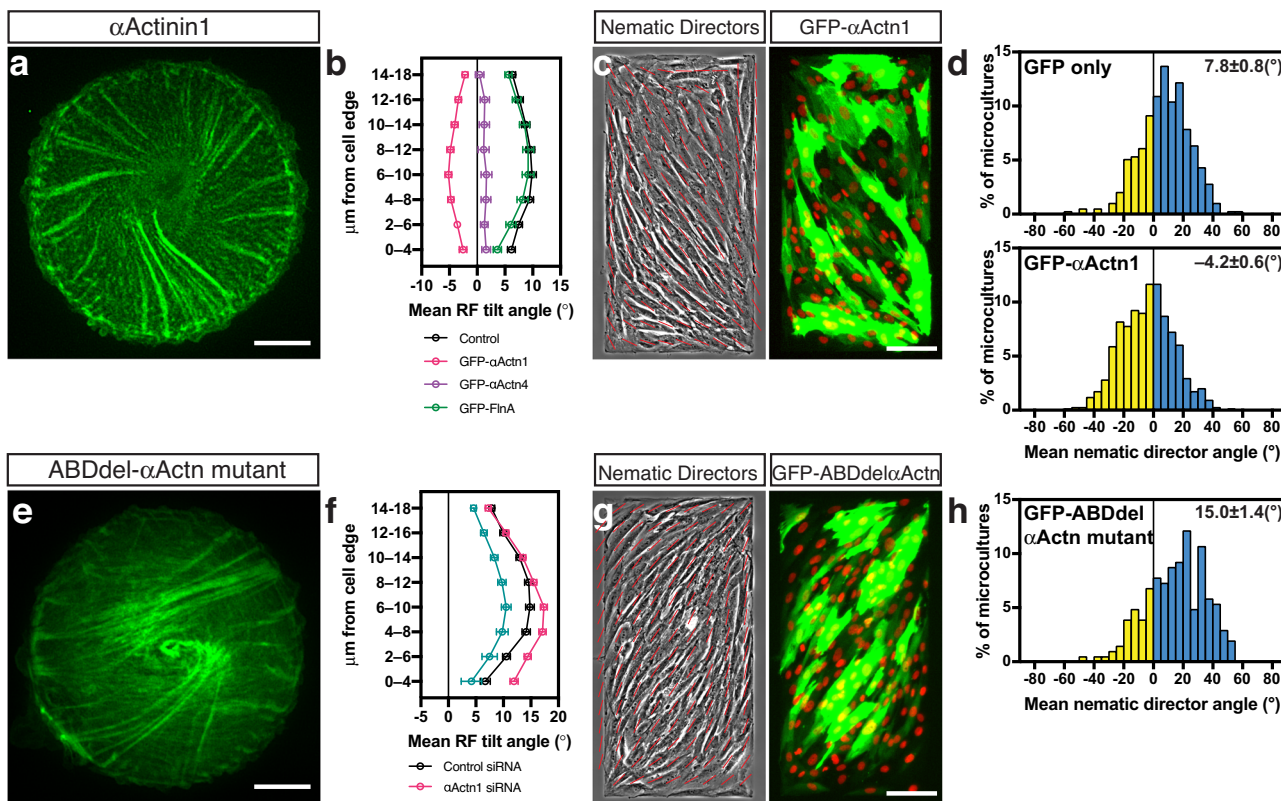


**Fig. 6 |  $\alpha$ -Actinin1 overexpression reverses the sign of chirality in individual cells and cell collectives.** **a** Typical image of GFP- $\alpha$ -actinin1 overexpressing cell with sinistral (reversed) tilt of radial fibres (RFs). **b** Average values of RF tilts (mean  $\pm$  SEM) as a function of the distance of annuli from the cell edge for control cells (LifeAct-labelled;  $n = 58$ ), cells overexpressing  $\alpha$ -actinin1 (GFP- $\alpha$ Actn1;  $n = 156$ ),  $\alpha$ -actinin4 (GFP- $\alpha$ Actn4;  $n = 92$ ) and filamin A (GFP-FlnA;  $n = 69$ ). Average RF tilts were calculated using images taken during the entire period of observation (12–16 h). **c** Phase-contrast image of rectangular microculture (left) and distribution of GFP- $\alpha$ -actinin1 transfected cells in the same field (right). **d** Histogram showing distribution of the angles of mean nematic directors characterising individual microcultures of GFP-only and GFP- $\alpha$ -actinin1 overexpressing cells ( $n = 394$  and 745 microcultures, respectively) at 48 h following plating. Note that the average nematic directors values are shifted in negative direction in microcultures of GFP- $\alpha$ -actinin1 overexpressing cells as compared to control GFP-only expressing cells. **e–h** Dextral chirality is preserved in cells with suppressed  $\alpha$ -actinin crosslinking function. **e** Typical actin organisation in dominant negative GFP-ABDdel- $\alpha$ -actinin

mutant expressing cell visualised by mRuby-LifeAct (pseudo-coloured green). **f** Average values of RF tilts (mean  $\pm$  SEM) as a function of the distance of annuli from the cell edge for control siRNA-transfected cells ( $n = 203$ , at 6 h post cell seeding),  $\alpha$ -actinin1 siRNA-transfected cells ( $n = 192$ , at 6 h post cell seeding) and GFP-ABDdel  $\alpha$ -actinin mutant expressing cells ( $n = 85$ , imaged for 12–16 h). **g** Phase-contrast image of rectangular microculture (left) and distribution of GFP-ABDdel- $\alpha$ -actinin mutant transfected cells in the same field (right). **h** Histogram showing distribution of the angles of mean nematic directors characterising individual microcultures of GFP-ABDdel- $\alpha$ -actinin mutant overexpressing cells. The histogram was built based on 206 microcultures at 48 h following plating. In **(c, g)** phase contrast images were overlaid with local nematic directors (red lines), nuclei are labelled with Hoechst 33342 (pseudo-coloured red). Negative and positive values in histograms (**d, h**) are coloured in yellow and cyan respectively. Scale bars, 10  $\mu$ m (**a, e**); 100  $\mu$ m (**c, g**). See also Supplementary Fig. 9, a–e. For statistical analysis, see Supplementary Table 1, lines 56–81.

anti-clockwise rotation of the nuclei could be seen (Supplementary Movie 7). Remarkably, the mean orientation of the stress fibres deviated from the direction of the long axis of the ellipse in a chiral manner (Fig. 9). Specifically, on average the stress fibres were tilted several degrees ( $^{\circ}$ ) to the right relative to the long axis of the ellipses (Fig. 9c and f), forming slashed ellipse  $\emptyset$  configurations (Fig. 9, a and d and Supplementary Fig. 13). An important piece of evidence that the chiral orientation of the stress fibres on elliptical substrate is driven by

chiral tilting of radial fibres, similar to that on circular substrate, was obtained in experiments with latrunculin A treatment. Similar to the situation on a circular pattern, the spreading on an elliptical pattern in the presence of the low-dose latrunculin A resulted in the formation of the system of stress fibres with reversed (sinistral) direction of chirality (Fig. 9b and e, and Supplementary Fig. 13a and b). On average, these stress fibres were tilted several degrees left relative to the long axis of the ellipses (Fig. 9c and f). Moreover, addition of latrunculin A to the

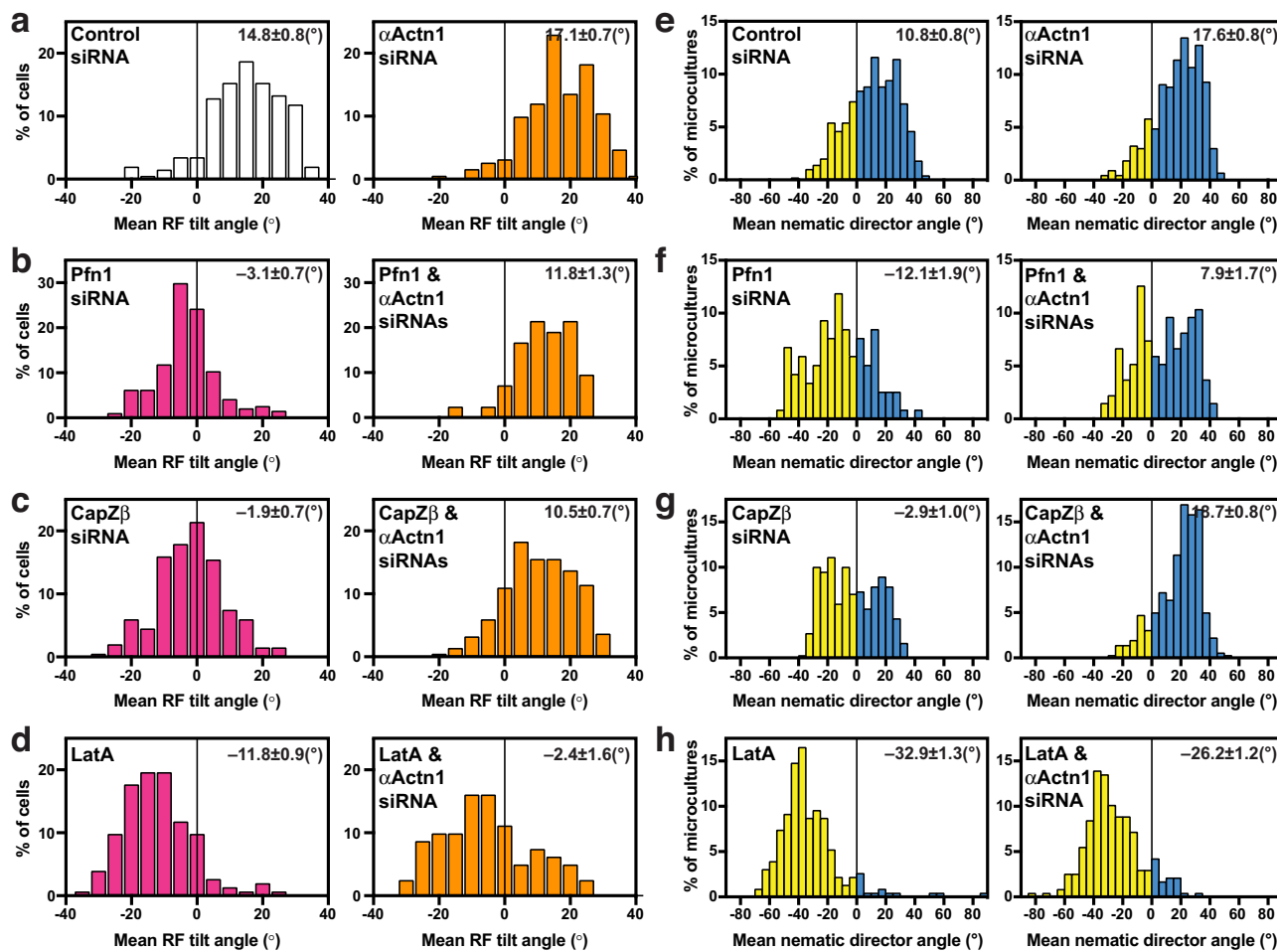


**Fig. 7 |  $\alpha$ -Actinin1 is required for the reversal of chirality direction. a-d** The reversion of radial fibre (RF) tilt is  $\alpha$ -actinin1-dependent. The histograms show the distribution of average RF tilt in the 6–10  $\mu\text{m}$  (a, b, d) or 8–12  $\mu\text{m}$  (c) annuli for (a) control siRNA-transfected cells ( $n = 203$ ) and  $\alpha$ -actinin1 siRNA-transfected cells ( $n = 192$ ), (b) profilin 1 (Pfn1) siRNA-transfected cells ( $n = 194$ ) and Pfn1 &  $\alpha$ -actinin1 siRNAs-transfected cells ( $n = 42$ ), (c) CapZ $\beta$  siRNA-transfected cells ( $n = 201$ ) and CapZ $\beta$  &  $\alpha$ -actinin1 siRNAs-transfected cells ( $n = 219$ ), and (d) 20 nM latrunculin A (LatA)-treated cells ( $n = 153$ ) and  $\alpha$ -actinin1 siRNA-transfected cells treated with 20 nM LatA ( $n = 94$ ). Bar colours in histograms (a-d): white – control cells, magenta – cells treated by agents reversing the chirality direction (Pfn1 siRNA, CapZ $\beta$  siRNA, LatA), orange –  $\alpha$ -actinin1 knockdown cells alone or treated with the chirality reversing agents. See also Supplementary Fig. 9f. e-h The effect of  $\alpha$ -actinin1

knockdown on reversion of the sign of cell alignment angle in microcultures. The histograms showing distributions of the angles of mean nematic directors characterising the microcultures at 48 h following plating for (e) control siRNA-transfected cells ( $n = 499$ ) and  $\alpha$ -actinin1 siRNA-transfected cells ( $n = 430$ ), (f) Pfn1 siRNA-transfected cells ( $n = 118$ ) and Pfn1 &  $\alpha$ -actinin1 siRNAs-transfected cells ( $n = 135$ ), (g) CapZ $\beta$  siRNA-transfected cells ( $n = 369$ ) and CapZ $\beta$  &  $\alpha$ -actinin1 siRNAs-transfected cells ( $n = 360$ ), and (h) 20 nM LatA-treated cells ( $n = 230$ ) and  $\alpha$ -actinin1 siRNA-transfected cells treated with 20 nM LatA ( $n = 237$ ). Negative and positive values in histograms (e-h) are coloured in yellow and cyan respectively. Mean  $\pm$  SEM values are indicated at the top right corner of each histogram. For statistical analysis, see Supplementary Table 1, lines 82–117.

cells on an elliptical pattern with completely established dextral stress fibres orientation led to re-organisation of the system of stress fibres and development of left-tilted sinistral orientation typical for cells treated with latrunculin A (Fig. 9i to k and Supplementary Movie 8).

## Discussion

The key improvement which made this study possible was the development of rigorous quantitative methods which permitted us to perform a large-scale assessment of the degree of left-right asymmetry in the organisation of the actin cytoskeleton in individual cells and the alignment of cells in confined cell groups. The process of left-right asymmetric actin swirling in isotropic discoid cells is manifested by unilateral tilting of the radial fibres. Thus, using deep-learning computational image analysis, we determined the angles characterising the degree of deviation of these fibres from the radial direction in individual cells. Formation of confluent cell monolayer in microcultures confined to a rectangular micropattern resulted in development of a prevalent angle of cell alignment. We assessed the deviation between

cell alignment axis and the long axis of the rectangle by measuring either the average angle of local nematic directors in phase-contrast images or the average angle of long axes of elliptical cell nuclei. These objective measurements of the left-right asymmetry in individual cells and cell groups allowed us to make quantitative comparisons between the processes of asymmetric actin cytoskeleton organisation and asymmetric cell alignment.

In contrast to earlier studies that focused on a single gene as the main regulator of left-right asymmetry, our study revealed that multiple actin-associated proteins are involved in the control of chiral morphogenesis in individual cells and multicellular microcultures. Among the proteins involved in actin assembly, formins, Arp2/3 complex, cofilins, capping protein and profilin appeared to be potent regulators of left-right asymmetry development. Some of these identified actin regulators were also reported to influence actomyosin-powered cortical flow<sup>35</sup> in *C.elegans* zygote. Both in our system and in *C.elegans*, formins (mDia1 and CYK-1<sup>23</sup> respectively) seem to be important players. This role of formin family proteins might be related

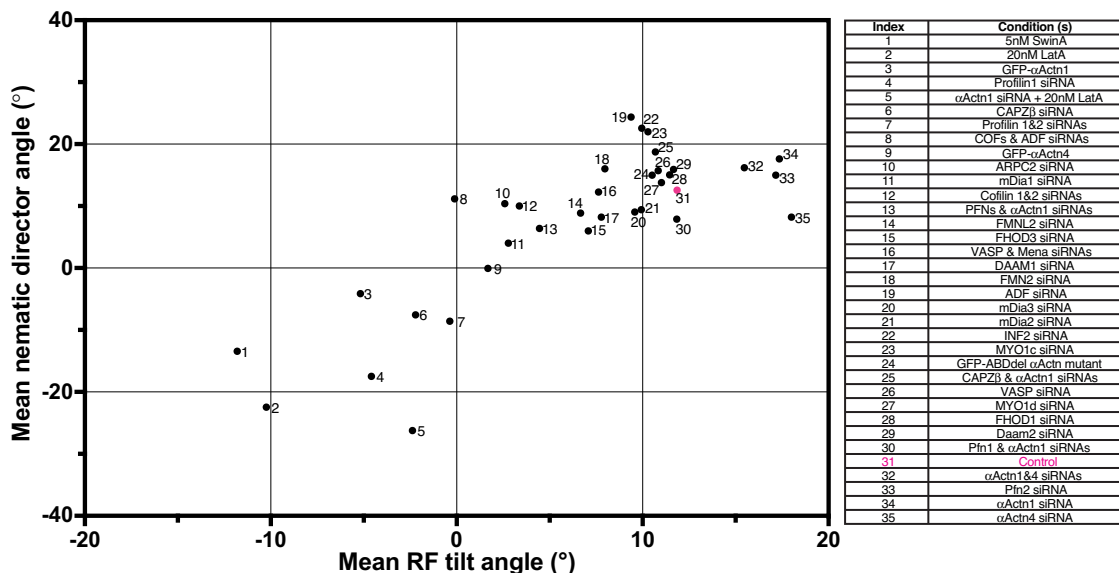


**Fig. 8 | The correlation between mean radial fibre tilt angle in individual cells and mean nematic director angle in microcultures.** Mean nematic director angles for rectangular microcultures are plotted against mean radial fibre (RF) tilt angles at the 6–10  $\mu$ m annulus for each type of treatment. Each dot represents average data from pooled experiments under respective conditions as indicated in the list on the right. The data are ordered and indexed according to ascending

radial fibre tilt angles (x-axis). Control cell data point is marked by magenta. Pearson correlation coefficient,  $r = 0.8104$ ,  $***p < 0.0001$ . Statistical analysis was implemented using GraphPad Prism software. Numbers of cells and microcultures analysed and the values of the means  $\pm$  SEM can be found in Supplementary Table 2. See also Supplementary Fig. 12.

to their rotation at the tip of actin filaments during polymerisation due to helical organization of actin filament<sup>36,37</sup>.

A remarkable type of response observed in our study was switching from dextral to sinistral chirality. While mutations reversing the direction of chirality at the organismal level have often been observed (*situs inversus* in vertebrates, reversed chirality of hindgut in flies, and sinistral chirality in snails<sup>1–3</sup>), the reversion of chirality in isolated individual cells was not sufficiently explored. In our studies, we found that the actin cytoskeleton of individual cells can also demonstrate a pattern of organisation that looks like a mirrored reflection of the normal chiral pattern. The most striking examples are knockdowns of profilin 1 (but not profilin 2) and CapZ $\beta$  subunit of capping protein CapZ, which both led to negative average tilting of the radial fibres in individual cells and clockwise (rather than anti-clockwise) cytoskeleton swirling. Another group of treatments that efficiently reversed chirality direction was treatment with low concentrations of actin polymerisation inhibitors, latrunculin A and swinholide A.

Surprisingly, mDia1, the formin critical for the dextral cell chirality appeared to be dispensable for sinistral chirality induced by the aforementioned treatments. At the same time, knockdown of  $\alpha$ -actinin1, which did not interfere with normal dextral chirality in individual cells (ref. <sup>11</sup> and present study), prevented the reversal of direction of individual cells chirality.  $\alpha$ -Actinin1 is a major cross-linking protein in radial fibres and its function in chirality determination may depend on its possible role in restricting individual filament rotation and regulation of radial fibre twisting. In our previous paper, we speculated that the torque induced by formin-driven rotation of trapped filament can occasionally be released (when elastic energy of the system approaches some threshold), leading to the rotation of filament in the opposite direction<sup>38</sup>. Such consideration could explain the reversal of cell chirality in  $\alpha$ -actinin1 over-expressing cells<sup>11</sup>. In recently published papers<sup>39,40</sup>, this model was elaborated and applied to the explanation of the phenomenon of chirality reversion. However, which factor induces filament rotation in cells with sinistral chirality in the absence of mDia1 remains to be elucidated.

Another model connects the direction of cell chirality with the structural organisation of the interactions between radial and transverse actin fibres. We posited previously that the initial breaking of the left-right symmetry starts when the radial actin bundle rotating unidirectionally around its long axis begins to 'roll' on circumferential transverse actomyosin structures in a 'rack-and-pinion' mechanism<sup>11,41</sup>. If the circumferential structures are 'above' the radial actin bundles (along z-axis), then the clockwise-rotation of the bundles (if one looks along the bundle axis from the barbed ends at focal adhesions) results in anti-clockwise swirling in the cell. However, if the circumferential structures are 'below' the radial actin bundles, then the clockwise-rotation of the bundles should produce clockwise swirling. It is possible that some perturbations of the actin dynamics and/or cross-linking could change the mutual position of radial and transverse fibres, thereby changing the direction of cell chirality. Future structural information is needed to evaluate this hypothesis.

Our experimental systems allowed us to perform systematic quantitative comparison between effects of diverse genetic and pharmacological treatments on development of left-right asymmetry in individual cells and multicellular microcultures confined to rectangular patterns. Asymmetric alignment of cells in our microcultures resembles chiral behaviour seen in cells confined to stripes or ring-shaped patterns<sup>8–10</sup>. Our study revealed a remarkable correlation between responses of individual cells and cell collectives in microcultures. With only few exceptions, the treatments which affected formation of asymmetric actin pattern in individual cells also affected asymmetric alignment of cell groups. Treatments that reversed actin chirality direction in individual cells always resulted in a change of the direction of average cell alignment in cell groups. These data, in line with<sup>42</sup>, provide strong experimental support to the hypothesis that the development of the chiral organisation in multicellular cultures, tissues, and organs is determined by the chirality of the actin cytoskeleton in the individual cell.

Our data on chiral deviation of the average direction of stress fibres from the long axis of elongated cells confined to an elliptical pattern could shed some light on the relationship between individual and collective cell chirality. Previous study suggests that the

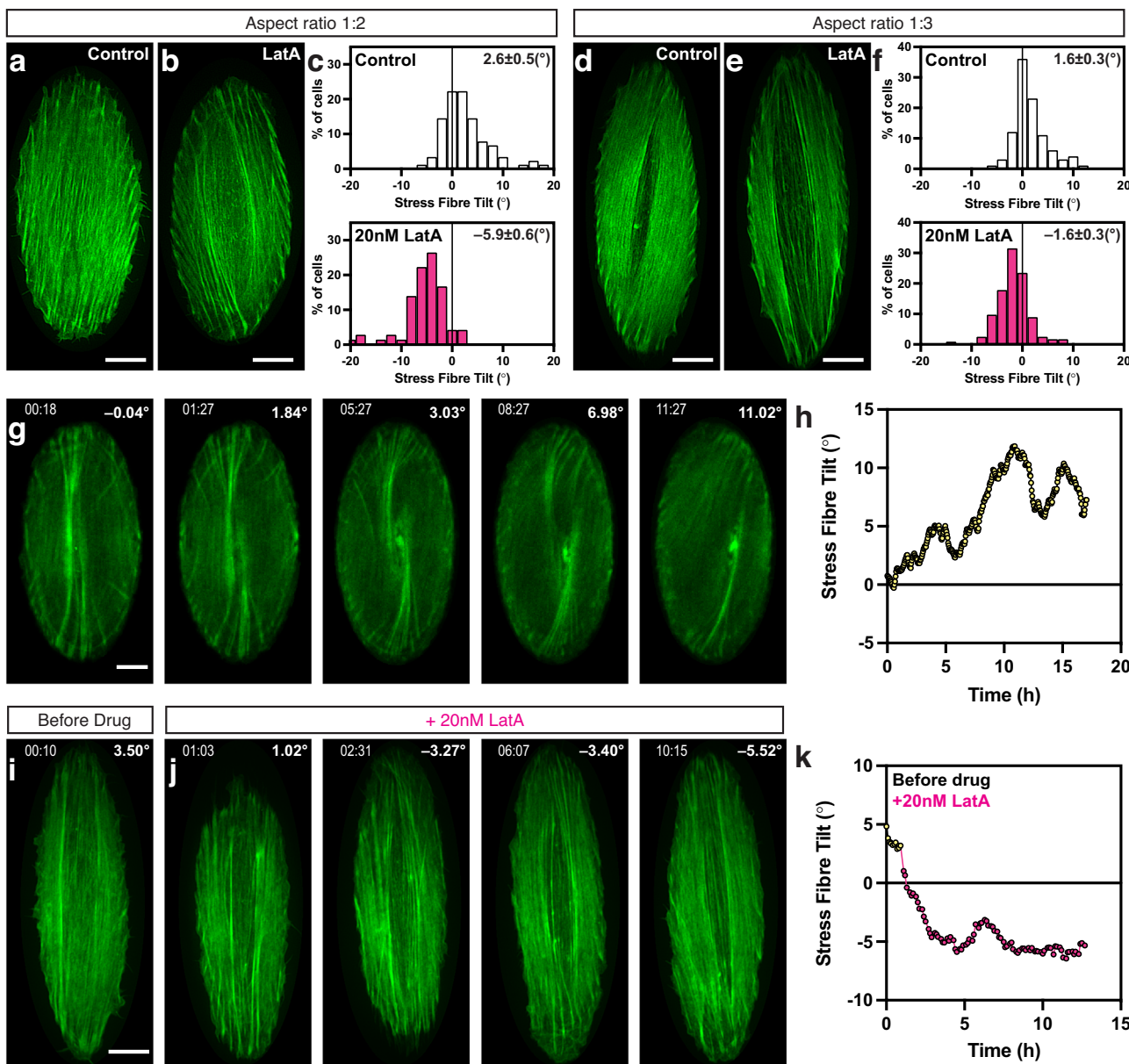


**Fig. 9 | Self-organisation of the actin cytoskeleton in individual cells confined to elliptical micropatterns.** **a–f** Actin cytoskeleton organisation, visualised by phalloidin-staining, of typical control (**a**, **d**) and latrunculin A-treated (**b**, **e**) cells 6 h following plating on elliptical fibronectin-coated patterns with an aspect ratio of 1:2 (**a–c**) and 1:3 (**d–f**) respectively. 20 nM Latrunculin A (LatA) was introduced 10 min after cell plating. The histograms (**c**, **f**) show the distribution of average tilt of stress fibres relative to the long axis of the ellipses in 100 control and 124 LatA-treated cells (**c**), and 90 control and 72 LatA-treated cells (**f**). White and magenta bars correspond to control and LatA-treated cells, respectively. Mean $\pm$ SEM values are indicated at the top right corner of each histogram. See also Supplementary Fig. 13. For statistical analysis, see Supplementary Table 1, lines 118–123. **g** A sequence of images of LifeAct-transfected control cell at different time points after plating on an

elliptical (1:2 aspect ratio) pattern. See also Supplementary Movie 7. **h** Graph showing the changes in the average stress fibre tilt over time in cell (**g**). The graph was smoothed by averaging 4 sequential measurements. **i**, **j** The actin stress fibres in LifeAct-transfected cell on an elliptical (1:3 aspect ratio) pattern before (**i**) and at different time points after the addition of latrunculin A (**j**). See also Supplementary Movie 8. **k** Graph showing the changes in the average stress fibre tilt over time in cell (**i–j**). (**g**, **i**, **j**) The time points (hh:mm) and corresponding stress fibre tilt (°) are indicated in upper left and right corners of the images, respectively. For display and analysis purpose, all images of cells on elliptical pattern were placed on black background and aligned along vertical direction. Scale bars, 10  $\mu$ m (**a**, **b**, **e**, **g**, **i**). See also Supplementary Fig. 13.

orientation of an individual cell starts with orientation of the systems of focal adhesions and stress fibres, followed by orientation of the cell as a whole<sup>43</sup>. We postulate that cells could preserve intrinsic actin cytoskeletal chirality when aligned with the boundaries of the adhesive pattern, in such a way that aligned cell migrates preferentially anti-clockwise around the pattern's boundary. In this scenario, individual cell anti-clockwise bias in collectives might causes an anticlockwise biased streaming of cells around the boundary of the rectangular micropattern because of the combination of contact inhibition of

locomotion, lateral interactions and leader-follower behaviours ultimately aligning cells' polarisation axes with each other to collectively evolve into the  $\mathbb{H}$ -orientation. This biased streaming of cells along the boundaries was also observed in other independent studies on collective cell chirality on stripes and rings patterns<sup>9,10</sup>. The future goal is to elucidate how chiral actin organisation drives chiral cell movement along the boundary of adhesive islands.

The hypothesis of the role of asymmetric self-organisation of the actin cytoskeleton in the emergence of chirality in tissues, organs, and

even in whole organism could unify the existing data on the development of left-right asymmetry in snails<sup>20,21</sup> and in *Drosophila*<sup>5,6,19,22</sup>, and probably for asymmetric heart looping in vertebrate development<sup>4</sup>. The formation of asymmetry of heart and visceral organs positioning in vertebrate deserves special discussion. It is well-established that in many species the key asymmetric factor triggering the signalling cascade determining left-right body asymmetry is an asymmetric flow generated by ciliated cells in the node (left-right organiser of the embryo)<sup>12</sup>. Recent studies have shown, however, that in birds and reptilia the nodal asymmetry does not depend on cilia<sup>1</sup>. Thus, the cilia may function as an amplifier, but not the primary source of asymmetry. Since the position and orientation of basal bodies can in principle be regulated by the actin cytoskeleton<sup>44</sup>, this suggests that the primary asymmetric factor in nodal cilia-dependent systems could still be the intrinsic asymmetry of the actin cytoskeleton. Extensive future studies are necessary to explore this possibility. In conclusion, our study revealed an actin polymerisation-dependent mechanism of establishment of left-right asymmetry in individual cells and cell groups which could be involved in the development of left-right asymmetry in organs and organisms.

## Methods

### Cells and plasmids transfection

Human foreskin fibroblasts (HFF) from American Type Culture Collection (catalog no. SCRC-1041) were cultured in Dulbecco's modified Eagle's medium high glucose supplemented with 10% fetal bovine serum (FBS), 1 mM sodium pyruvate and antibiotics (penicillin and streptomycin) at 5% CO<sub>2</sub> at 37 °C. Enucleated cells were generated as described in our earlier work in ref. <sup>12</sup>. Briefly, non-transfected or LifeAct-transfected cells were seeded onto plasma-treated plastic coverslips (ibidi GmbH) and left overnight to ~70% confluence. Next, cells were treated with 5 ml of 10 µg ml<sup>-1</sup> cytochalasin B (Sigma) in a 50 ml falcon tube and centrifuged at 10,864 g (Beckman centrifuge X30R) for 1 h at 37 °C to enucleate cells. Cells were washed three times with complete medium and allowed to recover for at least 2 h in complete medium following which cells were trypsinised for seeding onto the micropatterned substrate for the experiment. Presence of nuclei were verified by labelling with Hoechst 33342 (10 µg ml<sup>-1</sup> for 10 min) and live imaging of the nucleus. Cells were transfected with DNA plasmids via electroporation (Neon® transfection system, Life Technologies) following manufacturer's instructions. Electroporation condition consists of two pulses of 1150 V for 30 milliseconds. Expression vectors encoding the following fluorescent fusion proteins were used: LifeAct-GFP<sup>11</sup>, mRuby-LifeAct<sup>12</sup>, mEmerald-mDia1-C-14 (Addgene plasmid # 54156), pEGFP-C1 (Clontech), GFP-α-actinin1<sup>11</sup>, GFP-α-actinin4 (gift of Dr. M. Pan, Mechanobiology Institute, Singapore), GFP-ABDdel-α-actinin1<sup>11</sup> (gift of Dr P. Roca-Cusachs, University of Barcelona, Barcelona, Spain), EGFP-Filamin A (gift of Dr. M. Sheetz, Mechanobiology Institute, Singapore), mCherry-Cofilin 1 (gift of Dr. C. G. Koh, Nanyang Technological University, Singapore), mCherry-Profilin1 (Addgene plasmid #55121), Pfn1-P2A-eGFP (Clone ID: OHu24169; GenScript USA Inc) and GFP-VASP<sup>11</sup>. Fluorescence-activated cell sorting (FACS) were performed to select for upper 30% of cells expressing high level of fluorescent fusion proteins of pEGFP-C1, GFP-α-actinin1, GFP-α-actinin4 or GFP-ABDdel-α-actinin1. All cell culture and transfection reagents were obtained from Invitrogen. Other chemicals and reagents were obtained from Sigma, unless otherwise stated.

### siRNA transfection

Cells were seeded into a 35 mm dish on day 0 and transfected with 100 µM of siRNA using Lipofectamine RNAiMAX on days 1 and 2. For experiment involving individual cells, siRNA-transfected cells were trypsinised on day 4 and replated onto circular micropatterns. For experiment involving cell microcultures, siRNA-transfected cells were

trypsinised on day 3 and replated onto rectangular micropatterns. As needed, transfection of plasmids via electroporation into siRNA-treated cells were performed on day 3 and cells were replated on day 4. siRNA transfected cells had their proteins or RNAs extracted on day 4 for immunoblotting or RNA sequencing respectively. siRNAs used in this study are listed in Supplementary Table 3.

### Micropatterning of substrates

Cells were seeded on substrates containing either 1,800 µm<sup>2</sup> circular or elliptical micropatterns of different aspect ratio (individual cell experiment), or 300 × 600 µm rectangles (multicellular microculture experiment). Each micropatterned substrate was fabricated by stencil patterning as previously described in our earlier work<sup>12</sup>. Briefly, polydimethylsiloxane (PDMS) (Sylgard 184 kit, Dow Corning) was cast on the photoresist mould, containing micropattern designs of interest, using a 10:1 ratio (w/w) of elastomer to crosslinker and cured for 2 h at 80 °C. The crosslinked PDMS layer was peeled off and stamps were cut out manually. The PDMS stamp was then inverted and placed onto a hydrophobic uncoated 35 mm µ-dish (ibidi GmbH). Norland Optical Adhesive 73 (NOA-73, Norland Inc.) was deposited along an edge of the stamp and allowed to flow through the gaps between the PDMS stamp and dish by capillary action, upon which the stamp was sealed on all sides using NOA-73. The NOA-73 stencil was cured under ultraviolet illumination for 15 s. After peeling off the PDMS stamp, the stencil and dish were incubated with fibronectin (Calbiochem, Merck Millipore) at a concentration of 50 µg ml<sup>-1</sup> in 1 × PBS at 4 °C overnight after a brief degassing at 10 mbar. At the end of the incubation, the fibronectin solution was aspirated, and the stencil was removed. The printed dish bottom was passivated with 0.2% Pluronic acid-H<sub>2</sub>O for 10 min. Finally, the passivated dishes were washed thrice with 1 × PBS before cell seeding.

### Assessment of individual cells on circular micropattern

Cells were seeded on printed dishes containing circular micropatterns at a density of 5 × 10<sup>4</sup> cells ml<sup>-1</sup> for 10 min. The medium containing unattached cells was then replaced with fresh DMEM. After 6 h incubation, the cells were fixed using 4% paraformaldehyde (Tousimis, USA) in PBS for 10 min, followed by three 1 × PBS washes. Cells were permeabilised using 0.1% Triton-X-100 in PBS, and then blocked with 2% bovine serum albumin (BSA)-PBS for 1 h at room temperature (RT) before incubation with appropriate labelling reagents. Actin and nucleus staining were performed using phalloidin (Molecular Probes) and Hoechst 33342 (Invitrogen), respectively. For live cell imaging experiment, cells were seeded on circular micropatterns at a density of 5 × 10<sup>4</sup> cells ml<sup>-1</sup> for 10 min. The medium containing unattached cells was then replaced with Leibovitz's L-15 containing 10% FBS. Cells were left for at least 2 h before imaging at 37 °C with 5% CO<sub>2</sub>. Time-lapse images for 12–16 h at 10–20 min intervals and Z-stacks of step-size 0.35 µm with total height of 10–15 µm were acquired with a spinning disc confocal microscope (PerkinElmer Ultraview VoX) attached to an Olympus IX81 inverted microscope, equipped with a 100× oil immersion objective (1.40 NA, UPlanSApo), an EMCCD camera (C9100-13, Hamamatsu Photonics) for image acquisition, and Volocity software (PerkinElmer) to control the set-up. Fixed samples were also imaged with the same step-up. Maximum projection of the Z-stack images was performed with Volocity software or with Fiji software and exported as 16-bit TIFF files (512 × 512 pixel and 0.138502 µm pixel<sup>-1</sup>). Each image contained a single cell and these images were subsequently used for deep learning-based identification of radial fibres.

### Assessment of individual cells on elliptical micropattern

Cells were seeded on printed dishes containing elliptical micropatterns with an aspect ratio of 1:2 (34:68 µm) or 1:3 (27.5:84 µm) at a density of 5 × 10<sup>4</sup> cells ml<sup>-1</sup> for 10 min. The medium containing unattached cells was then replaced with fresh DMEM. After 6 h incubation,

the cells were fixed using 4% paraformaldehyde (Tousimis, USA) in PBS for 10 min, followed by three 1×PBS washes. Cells were permeabilised using 0.5% Triton-X-100 in PBS, and then blocked with 5% bovine serum albumin (BSA)-PBS for 1 h at RT before overnight incubation at 4 °C with appropriate primary antibodies. Cells were then incubated for 45 min at RT with appropriate labelling reagents: AlexaFluor-conjugated secondary antibodies (Molecular Probes, dilution 1:500) and Phalloidin (Molecular Probes). For live cell imaging experiment, cell seeding was as above except that the medium containing unattached cells was then replaced with Leibovitz's L-15 containing 10% FBS. Time-lapse images at 3 min intervals and Z-stacks of step-size 0.3 µm with a total height of 11 µm were acquired using a 60× oil immersion objective (1.35 NA, UPlanSApo) with the spinning disc confocal microscope (PerkinElmer Ultraview VoX). Fixed samples were also imaged with the above step-up using a 100× oil immersion objective (1.40 NA, UPlanSApo), or on the spinning disc confocal microscopy coupled with the live super-resolution (SR) module (Roper Scientific) attached to a Nikon Eclipse Ti-E inverted microscope with Perfect Focus System, equipped with 100× oil immersion objective (1.4 NA, PL APO VC), a sCMOS camera (Photometrics Prime 95B) for image acquisition, and MetaMorph software (Molecular Devices) to control the set-up. Maximum projection of the Z-stack images was performed with Velocity software or with Fiji software and exported as 16-bit TIFF files. Angle (°) of stress fibre tilt was measured using images of actin cytoskeleton in cells on elliptical micropattern labelled either by phalloidin or LifeAct with the OrientationJ plugin in Fiji software. As needed, image was rotated using transform tool with bicubic interpolation to align the long axis of the elliptical cell to the vertical orientation. An elliptical mask was then applied to the image and the angle of stress fibre tilt of each elliptical cell, single or in a time-lapse series, was measured using the OrientationJ Measure plugin.

#### Assessment of microcultures on rectangular micropatterns

Cells were seeded on rectangular micropatterns at a density of  $1 \times 10^5$  cells  $\text{ml}^{-1}$  for 20 min. The medium containing unattached cells was then replaced with fresh DMEM and cell microcultures were incubated for a total of 48 h before cell fixation using 4% paraformaldehyde-PBS for 10 min. Just prior to fixation, cell nuclei were stained with 1 µg  $\text{ml}^{-1}$  Hoechst 33342 for 10 min. Phase-contrast and fluorescence images of cell microcultures were taken using a 20× air objective (0.45 NA, LUCPLFLN20X, Olympus) on an Olympus IX81 inverted microscope, equipped with Andor Neo 5.5 sCMOS camera and light source (Lumencor SOLA SE Light Engine). Single plane images of phase contrast and DAPI channels were taken. Each image contained a single rectangular cell microculture and these images were subsequently used for measurement of average nematic directors angle and nuclei orientation angles in rectangular microcultures.

#### Drug treatment

For drug inhibition studies, 10 min following cell seeding on micropatterns, the medium containing unattached cells was replaced with fresh medium containing either 20 nM latrunculin A (Santa Cruz Biotechnology Inc., SCB Inc.) or 5 nM swinholide A (SCB Inc.). For experiments that lasted more than 24 h, fresh drugs were added every 24 h until the end of the observation period. All inhibitors remained in the medium during the entire period of observation, except in drug washout experiments.

#### Segmentation of radial fibres

Images of the actin cytoskeleton were first converted to 8-bit and the 'Enhance brightness/contrast' function in Fiji software was used with the 'saturated pixels' parameter set to the default of 0.35. A Unet-ResNet50 deep learning model<sup>45</sup>, implemented in Python, was trained to identify actin radial fibres in cells confined on circular micropattern. Briefly, the following steps were taken. The model was trained using 32

images of actin cytoskeleton labelled by fluorescent protein tagged-LifeAct. These training images comprise of cells with their actin cytoskeleton in a radial or chiral organisation, and images of varied intensities were selected. Data augmentation was done using the Albumentations library<sup>46</sup>. The ground-truths (binary, 8-bit) were prepared by manual demarcation of actin radial fibres in Fiji. The code and complete list of parameters of the trained deep learning model is available via <https://github.com/gohweijia/Cell-Chirality-Analysis>. This trained model was used to identify radial fibres in both phalloidin- and LifeAct-labelled cells, returning a 32-bit image of identified radial fibres. Segmentation of these identified radial fibres was performed using a custom MATLAB script, in which background subtraction (with rolling ball of 30-pixel radius) and then Niblack local thresholding<sup>47</sup>, with window size of  $15 \times 15$ ,  $k = -0.3$  and offset = -0.01, were applied. The resulting binary image was then skeletonised using the MATLAB built-in function, bwmorph. Intersecting radial fibres were separated by branch point removal, and fibre segments with similar orientation (angle difference  $\leq 30^\circ$ ) and at nearby position (distance  $\leq 30$  pixels) were connected as a single fibre.

#### Measurement of radial fibre tilt angles

The following procedures were performed using a custom MATLAB script unless otherwise stated. Cell segmentation was performed by thresholding the Gaussian-smoothed (sigma value set to 3) actin image using Otsu binarization (threshold value set to 0.4 of Otsu auto threshold), followed by a series of mathematical morphological operations (imclose, imfill, imeroade). Cell centroid and cell spread area were calculated based on this cell mask. The cell mask was also used for generating concentric ring masks of 4 µm in width starting from the cell edge, with 2 µm increments, for masking the segmented radial fibres. In each ring, the angle of each radial fibre segment was measured relative to the cell edge. See also Supplementary Fig. 1c. The angle at the cell edge  $\theta$ , computed using Python, was given by the formula  $\theta = \arcsin(\frac{\sin \theta_r}{R})$ , where  $R$  connects the cell centroid and intersection of the continuation of the radial fibre segment with the edge of the cell and  $r$  connects the cell centroid and intersection of radial fibre with outer edge of the annulus.  $\theta$  and  $\theta_r$  are the angles between the radial fiber segment and  $R$  and  $r$  respectively (Supplementary Fig. 1c). Based on visual inspection, actin fibre segments with  $\theta_r$  more than or equals to  $68^\circ$  were unlikely to be radial fibres and were omitted from the analysis. The average inflation of area of the cell mask relative to the area of the micropatterns ( $1800 \mu\text{m}^2$ ) was estimated to be  $63.353 \mu\text{m}^2$  using a dataset of ~100 cells. This constant was subtracted from the cell area before the computation of cell radius  $R$ . Only cells with area between 1700 and  $2000 \mu\text{m}^2$  were analysed.

#### Computation of nematic directors and nuclei orientation

The following procedures were performed using a custom MATLAB script unless otherwise stated. First, identification and segmentation of individual rectangular microculture using phase contrast images was done by performing a Wiener filter with a neighbourhood size of  $20 \times 20$  pixels to remove image noise. This was followed by an entropy filter with a  $3 \times 3$  pixels structural element and morphological opening with a  $9 \times 9$  pixels structural element. This results in an image that differentiates between areas with and without cells. Otsu binarization was then performed to segment the image, the segmented area at the centre of the image was selected as the segmentation mask. This serves as an indicator of the area covered with cells. The bounding box enclosing this segmented area serves to represent the dimensions of the microculture. Only microcultures with bounding box width of 225 to 375 µm and height of more than 550 µm, and with a segmentation mask that covered more than 80% of the bounding box area were analysed. For each bounding box, the centre  $200 \times 500 \mu\text{m}$  region of interest was used for subsequent steps in the measurements of average nuclei orientation and average nematic director orientation.

Segmentation of the nuclei was achieved using NICK adaptive binarization<sup>48,49</sup>. A Wiener filter using a neighbourhood size of  $9 \times 9$  pixels was performed prior to segmentation. The concaved-point based splitting algorithm<sup>50</sup> was used to separate any overlapping nuclei. Segmented objects above the size of 10000 pixels were removed as these corresponded to the background regions, while objects smaller than 500 pixels were also removed as these were either fragmented nuclei or noise regions that were segmented by chance. In addition, only nucleus that had a centroid position that laid within the bounding box of the segmented phase contrast image was selected for further analysis. The number of nuclei in the bounding box was also counted. Microcultures that had less than 50 nuclei were removed as these microcultures often had too few cells to cover the entire rectangular micropattern. The orientation of these nuclei was then calculated based on the angle of the long axis of a fitted ellipse with respect to the long axis of the rectangular micropattern. Alignment of the cell group was determined based on the mean resultant length<sup>51</sup> of the nuclei orientation. A cutoff value of 0.35 was selected and any rectangle with a mean resultant length greater than that was classified as aligned. The mean nuclei orientation per aligned microculture was determined by calculating the mean of all the orientations of the individual nuclei within a single microculture.

Local cell orientation in the phase contrast image was calculated by obtaining the nematic director field as described in ref. <sup>26</sup>. Briefly the orientation tensor was obtained using OrientationJ implemented in Fiji and the nematic director was obtained using a window size of  $60 \times 60 \mu\text{m}^2$  and 70% overlap. The orientation of each directors was measured as the angle relative to the long axis of the rectangular micropattern. The orientation of the directors within the region of interest was then used to determine the alignment of the microculture in a similar manner as that for the nuclei orientation. A higher cutoff value of 0.5 for alignment was set due to more coherent nature of the nematic directors. The mean nematic director angle per aligned microculture was determined by calculating the mean of all the orientations of the directors within a single microculture.

### Immunoblotting

Cell pellets were collected in RIPA buffer (SCB Inc.) supplemented with  $2 \mu\text{L ml}^{-1}$  protease inhibitors cocktail (Sigma, catalogue no. P8340), and were then mechanically lysed by syringing through a 27.25 G needle on ice. Protein concentration was quantified using the Micro BCA Protein Assay Kit (Thermo Scientific) according to manufacturer's instructions.  $20 \mu\text{g}$  of protein lysate was dissolved in  $1 \times$  Laemmli sample buffer supplemented with 10% 2-mercaptoethanol, and separated by 4–20% SDS-polyacrylamide gel (GenScript USA Inc) electrophoresis at 100 V for 1 h and then transferred to a  $0.4 \mu\text{m}$  pore size PVDF membrane (Thermo Scientific, catalog number 88518) at 100 V for 2 h for formin proteins and 1 h for other proteins in an ice bath. The PVDF membrane was blocked using Intercept<sup>®</sup> (TBS) Blocking Buffer (LI-COR, Inc.) or 5% nonfat milk (Bio-Rad) in Tris-buffered saline with 0.1% Tween 20 (TBS-T) for 1 h at RT before incubation at  $4^\circ\text{C}$  overnight with appropriate primary antibodies. Primary antibodies were diluted in Intercept<sup>®</sup> (TBS) Blocking Buffer containing 0.1% Tween-20 at their respective concentrations summarised in Supplementary Table 4. After washes in TBS-T, the membrane was probed with either IRDye<sup>®</sup> 680RD Goat anti-Rabbit IgG (LI-COR, dilution 1:5,000) or IRDye<sup>®</sup> 800CW Goat anti-Mouse IgG (LI-COR, dilution 1:15,000) for 1 h at RT. The membrane was then washed in TBS-T before fluorescent detection with an Odyssey<sup>®</sup> CLx imaging system at a resolution of  $169 \mu\text{m}$  and 'medium' quality settings on Image Studio software. Alternatively, the primary antibody binding was processed for ECL detection with appropriate HRP-conjugated secondary antibodies (Santa Cruz Biotechnology, catalogue no. sc-2004/5, dilution 1:10,000) and acquisition using Image Lab Touch Software on GelDoc Go Imaging System (Bio-Rad). Protein ladder used include: Precision Plus Protein<sup>™</sup>

Kaleidoscope<sup>™</sup> Prestained Protein Standards (Bio-Rad; catalog number 1610375), Broad Multi Color Pre-Stained Protein Standard (GenScript USA Inc; catalog number M00624) and Cruz Marker<sup>™</sup> Molecular Weight Standards (SCB Inc; catalog number sc-2035).

### Transcriptome profiling by RNA sequencing

RNAs were extracted using RNeasy<sup>®</sup> Plus Universal Kits (Qiagen) according to manufacturer's instructions. Library was prepared using TruSeq Stranded mRNA LT Sample Prep Kit and sequenced using NovaSeq6000 Illumina platform. Alignment was performed (STAR aligner) and trimmed reads were mapped to GRCh38 reference genome (BioProject: PRJNA312570) with HISAT2, splice-aware aligner. Gene expression was presented using transcript per million (TPM) reads.

### Statistics and reproducibility

The numbers of samples (n) of individual cells and microcultures analysed for all of the quantitative data are specified in the figure legends and summarised in Supplementary Table 2. No statistical method was used to predetermine sample size. All images are representative of at least three independent experiments, except for Fig. 3c, Fig. 5e,f, Fig. 6, Fig. 9i,j and Supplementary Figs. 8–10, which were from two independent experiments and Supplementary Fig. 3 was from a single experiment. The quantified immunoblots in Supplementary Figs. 11 and 7c were from three independent experiment and Fig. 5 was from two independent experiments. The rest of the quantified immunoblots were obtained in a single experiment. Transcriptome profiling of gene expression levels by RNA-sequencing (RNA-seq) shown was from a single experiment, except for Supplementary Figs. 2a and 11a (mDia1 and Profilin 1 knockdown cells) which were from two experiment. All supplementary videos show representative data from at least two independent experiments. Prism software (version 9.4.1; GraphPad Software, LLC.) was used for data and statistical analysis, including frequency distribution for histograms plot, Mann-Whitney test for comparison and reporting of significant difference between two groups, Kruskal-Wallis test for multiple comparisons across groups and reporting of any significant difference between groups. Wilcoxon signed-rank test to estimate the difference of median values of samples from zero, and sum of 2 Gaussian fit. For frequency distribution, a bin width of  $5^\circ$  is used for all histograms, except for histograms representing stress fibre tilt which uses a bin width of  $2^\circ$ . Statistical significance is defined as  $P < 0.05$ . Mann-Whitney test was two-tailed. Kruskal-Wallis test was implemented with Dunn's multiple comparisons test and report multiplicity adjusted P value for each comparison. Wilcoxon signed-rank test was implemented against a hypothetical value of zero. For each histogram, we compared the fit of Gaussian versus Sum of two Gaussians with default software recommended parameters, including least squares regression, asymmetrical confidence intervals (CI) using 95% confidence level and plot 95% confidence bands. There was neither special handling of outliers nor weighting. Bimodal distribution is defined by the following parameters: preferred fit by the Sum of two Gaussians and represented by 1 negative (Mean1) and 1 positive (Mean2) means demonstrating chiral sign in opposite directions. Reliability of bimodality is checked by plotting the fitting curve with 95% confidence bands over the histogram (see Supplementary Fig. 4a).

### Reporting summary

Further information on research design is available in the Nature Portfolio Reporting Summary linked to this article.

### Data availability

All data generated or analysed during this study are included in this published article (and its Supplementary Information files). Raw datasets corresponding to all histograms in the main figures,

uncropped western blots and gene expression profiles presented as transcript per million (TPM) reads are provided as a Source Data file with this paper. The raw dataset for all other graphs presented in this study are available from the corresponding authors on reasonable request. Source data are provided with this paper.

## Code availability

Custom-written code used to analyse the data in the current study is available from the corresponding authors on reasonable request. The image analysis code for radial fibre segmentation and measurement of their tilt angle can be found at Github - <https://github.com/gohweijia/Cell-Chirality-Analysis>.

## References

- Hamada, H. & Tam, P. Diversity of left-right symmetry breaking strategy in animals. *F1000Res* **9**, F1000 (2020).
- Blum, M. & Ott, T. Animal left-right asymmetry. *Curr. Biol.* **28**, R301–R304 (2018).
- Martin-Duran, J. M., Vellutini, B. C. & Hejnol, A. Embryonic chirality and the evolution of spiralian left-right asymmetries. *Philos. Trans. R. Soc. Lond. B Biol. Sci.* **371**, 20150411 (2016).
- Desgrange, A., Le Garrec, J. F. & Meilhac, S. M. Left-right asymmetry in heart development and disease: forming the right loop. *Development* **145**, dev162776 (2018).
- Speder, P., Adam, G. & Noselli, S. Type ID unconventional myosin controls left-right asymmetry in Drosophila. *Nature* **440**, 803–807 (2006).
- Hozumi, S. et al. An unconventional myosin in Drosophila reverses the default handedness in visceral organs. *Nature* **440**, 798–802 (2006).
- Cho, B., Song, S. & Axelrod, J. D. Prickle isoforms determine handedness of helical morphogenesis. *Elife* **9**, e5145 (2020).
- Chen, T. H. et al. Left-right symmetry breaking in tissue morphogenesis via cytoskeletal mechanics. *Circ. Res* **110**, 551–559 (2012).
- Duclos, G. et al. Spontaneous shear flow in confined cellular nematics. *Nat. Phys.* **14**, 728–732 (2018).
- Wan, L. Q. et al. Micropatterned mammalian cells exhibit phenotype-specific left-right asymmetry. *Proc. Natl Acad. Sci. USA* **108**, 12295–12300 (2011).
- Tee, Y. H. et al. Cellular chirality arising from the self-organization of the actin cytoskeleton. *Nat. Cell Biol.* **17**, 445–457 (2015).
- Jalal, S. et al. Actin cytoskeleton self-organization in single epithelial cells and fibroblasts under isotropic confinement. *J. Cell Sci.* **132**, jcs220780 (2019).
- Schonegg, S., Hyman, A. A. & Wood, W. B. Timing and mechanism of the initial cue establishing handed left-right asymmetry in *Cae-norhabditis elegans* embryos. *Genesis* **52**, 572–580 (2014).
- Naganathan, S. R., Furthauer, S., Nishikawa, M., Julicher, F. & Grill, S. W. Active torque generation by the actomyosin cell cortex drives left-right symmetry breaking. *Elife* **3**, e04165 (2014).
- Xu, J. et al. Polarity reveals intrinsic cell chirality. *Proc. Natl Acad. Sci. USA* **104**, 9296–9300 (2007).
- Brown, N. A. & Wolpert, L. The development of handedness in left-right asymmetry. *Development* **109**, 1–9 (1990).
- Henley, C. L. Possible Origins of Macroscopic Left-Right Asymmetry in Organisms. *J. Stat. Phys. Vol.* **148**, 741–775 (2012).
- Basu, B. & Brueckner, M. Cilia multifunctional organelles at the center of vertebrate left-right asymmetry. *Curr. Top. Dev. Biol.* **85**, 151–174 (2008).
- Lebreton, G. et al. Molecular to organismal chirality is induced by the conserved myosin 1D. *Science* **362**, 949–952 (2018).
- Davison, A. et al. Formin Is Associated with Left-Right Asymmetry in the Pond Snail and the Frog. *Curr. Biol.* **26**, 654–660 (2016).
- Abe, M. & Kuroda, R. The development of CRISPR for a mollusc establishes the formin Lsdia1 as the long-sought gene for snail dextral/sinistral coiling. *Development* **146**, dev175976 (2019).
- Chougule, A. et al. The Drosophila actin nucleator DAAM is essential for left-right asymmetry. *PLoS Genet* **16**, e1008758 (2020).
- Middelkoop, T. C. et al. CYK-1/Formin activation in cortical RhoA signaling centers promotes organismal left-right symmetry breaking. *Proc. Natl Acad. Sci. USA* **118**, e2021814118 (2021).
- Chin, A. S. et al. Epithelial Cell Chirality Revealed by Three-Dimensional Spontaneous Rotation. *Proc. Natl Acad. Sci. USA* **115**, 12188–12193 (2018).
- Jegou, A. & Romet-Lemonne, G. The many implications of actin filament helicity. *Semin Cell Dev. Biol.* **102**, 65–72 (2020).
- Saw, T. B. et al. Topological defects in epithelia govern cell death and extrusion. *Nature* **544**, 212–216 (2017).
- Carlier, M. F. & Shekhar, S. Global treadmilling coordinates actin turnover and controls the size of actin networks. *Nat. Rev. Mol. Cell Biol.* **18**, 389–401 (2017).
- Pimm, M. L., Hotaling, J. & Henty-Ridilla, J. L. Profilin choreographs actin and microtubules in cells and cancer. *Int Rev. Cell Mol. Biol.* **355**, 155–204 (2020).
- Courtemanche, N., Pollard, T. D. & Chen, Q. Avoiding artefacts when counting polymerized actin in live cells with LifeAct fused to fluorescent proteins. *Nat. Cell Biol.* **18**, 676–683 (2016).
- Fujiwara, I., Zweifel, M. E., Courtemanche, N. & Pollard, T. D. Latrunculin A Accelerates Actin Filament Depolymerization in Addition to Sequestering Actin Monomers. *Curr. Biol.* **28**, 3183–3192 e3182 (2018).
- Klenchin, V. A., King, R., Tanaka, J., Marriott, G. & Rayment, I. Structural basis of swinholide A binding to actin. *Chem. Biol.* **12**, 287–291 (2005).
- Roca-Cusachs, P. et al. Integrin-dependent force transmission to the extracellular matrix by alpha-actinin triggers adhesion maturation. *Proc. Natl Acad. Sci. USA* **110**, E1361–E1370 (2013).
- Hofmann, W. A., Richards, T. A. & de Lanerolle, P. Ancient animal ancestry for nuclear myosin. *J. Cell Sci.* **122**, 636–643 (2009).
- Pyrpassopoulos, S., Feeser, E. A., Mazerik, J. N., Tyska, M. J. & Ostap, E. M. Membrane-bound myo1c powers asymmetric motility of actin filaments. *Curr. Biol.* **22**, 1688–1692 (2012).
- Naganathan, S. R. et al. Morphogenetic degeneracies in the actomyosin cortex. *Elife* **7**, e37677 (2018).
- Mizuno, H. et al. Rotational movement of the formin mDia1 along the double helical strand of an actin filament. *Science* **331**, 80–83 (2011).
- Yu, M. et al. mDia1 senses both force and torque during F-actin filament polymerization. *Nat. Commun.* **8**, 1650 (2017).
- Shemesh, T., Otomo, T., Rosen, M. K., Bershadsky, A. D. & Kozlov, M. M. A novel mechanism of actin filament processive capping by formin: solution of the rotation paradox. *J. Cell Biol.* **170**, 889–893 (2005).
- Li, X. & Chen, B. Mobility of Alpha-Actinin Along Growing Actin Filaments Might Affect the Cellular Chirality. *J. Appl. Mech.* **88**, 1–14 (2021).
- Li, X. & Chen, B. How torque on formins is relaxed strongly affects cellular swirling. *Biophys. J.* **121**, 2952–2961 (2022).
- Mogilner, A. & Mogilner, B. Cytoskeletal chirality: swirling cells tell left from right. *Curr. Biol.* **25**, R501–R503 (2015).
- Inaki, M. et al. Chiral cell sliding drives left-right asymmetric organ twisting. *Elife* **7**, e32506 (2018).
- Prager-Khoutorsky, M. et al. Fibroblast polarization is a matrix-rigidity-dependent process controlled by focal adhesion mechanosensing. *Nat. Cell Biol.* **13**, 1457–1465 (2011).

44. Brucker, L., Kretschmer, V. & May-Simera, H. L. The entangled relationship between cilia and actin. *Int J. Biochem Cell Biol.* **129**, 105877 (2020).
45. He, K., Zhang, X., Ren, S. & Sun, J. in 2016 IEEE Conference on Computer Vision and Pattern Recognition (CVPR) 770–778 (2016).
46. Buslaev, A. et al. Albumentations: Fast and Flexible Image Augmentations. *Information* **11**, 125 (2020).
47. Motl, J. Nick local image thresholding (<https://www.mathworks.com/matlabcentral/fileexchange/42104-nick-local-image-thresholding>), MATLAB Central File Exchange. Retrieved October 23, 2013. (2013).
48. Khurshid, K., Siddiqi, I., Faure, C. & Vincent, N. Comparison of Niblack inspired binarization methods for ancient documents, Vol. 7247. (SPIE, 2009).
49. Motl, J. Niblack local thresholding (<https://www.mathworks.com/matlabcentral/fileexchange/40849-niblack-local-thresholding>), MATLAB Central File Exchange. Retrieved October 8, 2016. (2013).
50. Qi, J. Dense nuclei segmentation based on graph cut and convexity-concavity analysis. *J. Microsc* **253**, 42–53 (2014).
51. Jammalamadaka, S. R. A. S., Ashis. Circular Probability Distributions in *Topics in Circular Statistics* (World Scientific, 2001), pp. 25–64.

## Acknowledgements

We thank M. M. Kozlov (Tel Aviv University, Israel) and T. Hiraiwa (MBI, Singapore) for discussion, T. B. Saw (MBI, Singapore) for consulting on nematic cell orientation, M. Davidson fluorescence protein collection (The Florida State University, Tallahassee, USA), P. Roca-Cusachs, M. Pan, M. Sheetz and C. G. Koh for providing reagents, A. Wong (MBI, Singapore) for expert help in paper editing, P. Kathirvel (MBI, Singapore) and H. Chen (MBI, Singapore) for expert help in molecular work and FACS, and the SIMBA microscopy facility and nanofabrication core facility at the Mechanobiology Institute for technical help. The research is supported in part by the Singapore Ministry of Education Academic Research Fund Tier 2 (MOE Grant No: MOE2018-T2-2-138, awarded to A.D.B; MOE2019-T2-1-099 and MOE2019-T2-02-014; awarded to P.K.), and Tier 3 (MOE Grant No: MOE2016-T3-1-002 and MOET32021-0003; awarded to A.D.B), the National Research Foundation, Prime Minister's Office, Singapore, and the Ministry of Education under the Research Centers of Excellence program through the Mechanobiology Institute, Singapore (ref no. R-714-006-006-271), and by the Singapore Ministry of Health's National Medical Research Council under its Open Fund - Young Individual Research Grant (Grant No: OFYIRG18may-0041; awarded to Y.H.T).

## Author contributions

Y.H.T. and A.D.B conceived and designed the experiments. Y.H.T, W.J.G and X.Y. performed most experiments. J.H., I.Y.Y.T., S.S., S.J., S.F.H.B., P.K., W.H., J.Y., Y.A.B.L., and V.T. contributed to some experiments. W.J.G, X.Y. and H.T.O. developed image analysis tools. A.M. contributed to data analysis and theoretical considerations in Discussion. Y.H.T., A.M., and A.D.B. wrote the manuscript with input from all of the authors.

## Competing interests

The authors declare no competing interests.

## Additional information

**Supplementary information** The online version contains supplementary material available at <https://doi.org/10.1038/s41467-023-35918-1>.

**Correspondence** and requests for materials should be addressed to Yee Han Tee or Alexander D. Bershadsky.

**Peer review information** *Nature Communications* thanks Amy Maddox, and the other, anonymous, reviewer(s) for their contribution to the peer review of this work. Peer reviewer reports are available.

**Reprints and permissions information** is available at <http://www.nature.com/reprints>

**Publisher's note** Springer Nature remains neutral with regard to jurisdictional claims in published maps and institutional affiliations.

**Open Access** This article is licensed under a Creative Commons Attribution 4.0 International License, which permits use, sharing, adaptation, distribution and reproduction in any medium or format, as long as you give appropriate credit to the original author(s) and the source, provide a link to the Creative Commons license, and indicate if changes were made. The images or other third party material in this article are included in the article's Creative Commons license, unless indicated otherwise in a credit line to the material. If material is not included in the article's Creative Commons license and your intended use is not permitted by statutory regulation or exceeds the permitted use, you will need to obtain permission directly from the copyright holder. To view a copy of this license, visit <http://creativecommons.org/licenses/by/4.0/>.

© The Author(s) 2023

# Supplementary Information for

## **Actin polymerisation and crosslinking drive left-right asymmetry in single cell and cell collectives**

*Tee et al.*

### **This PDF file includes:**

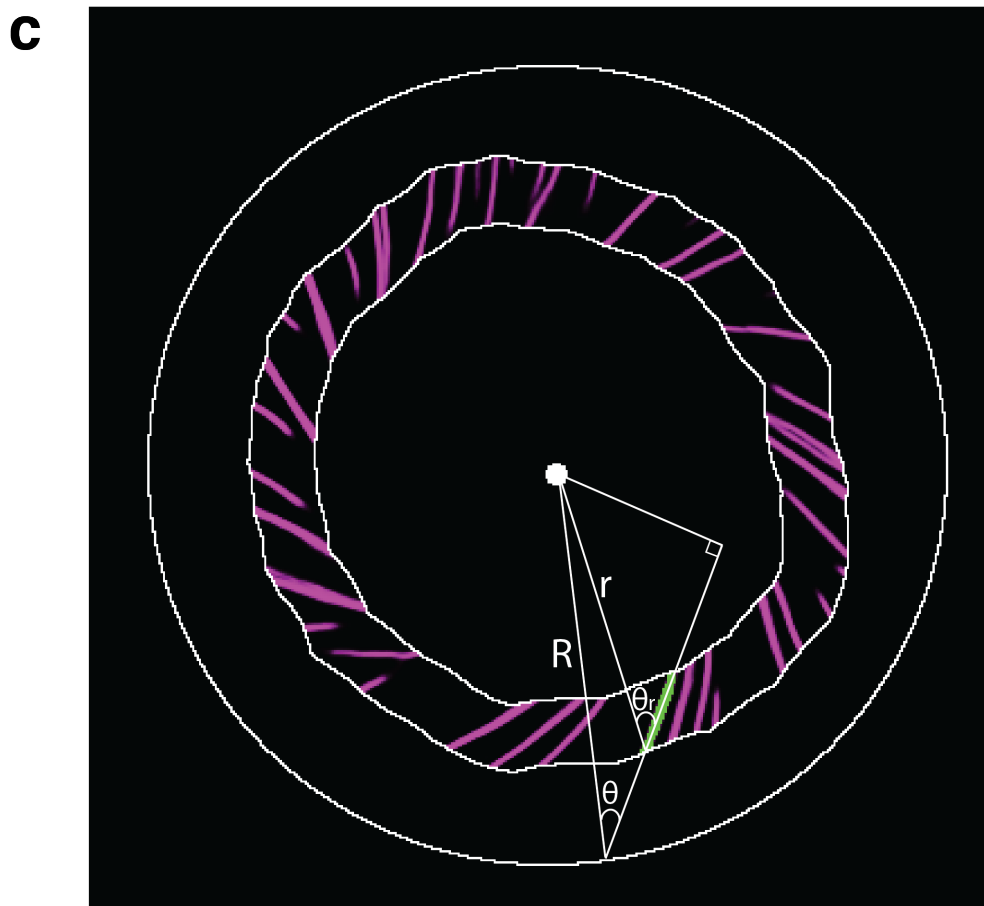
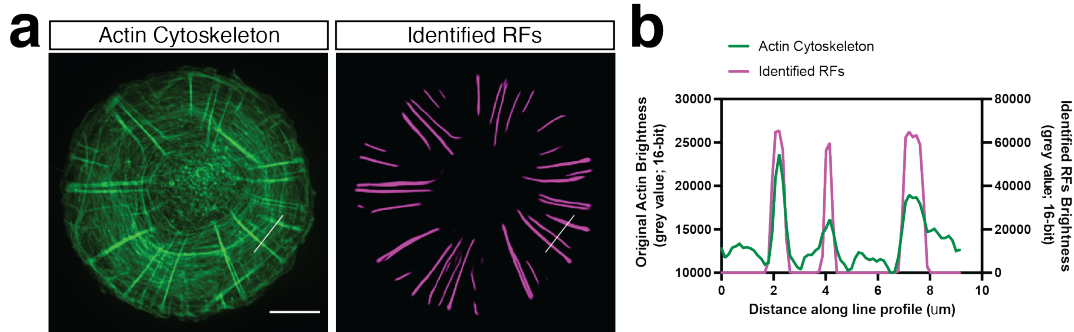
Supplementary Figs 1 to 13

Supplementary Tables 1 to 4

### **Other Supplementary Materials for this manuscript include the following:**

Supplementary Movies 1 to 8

Description of additional supplementary files

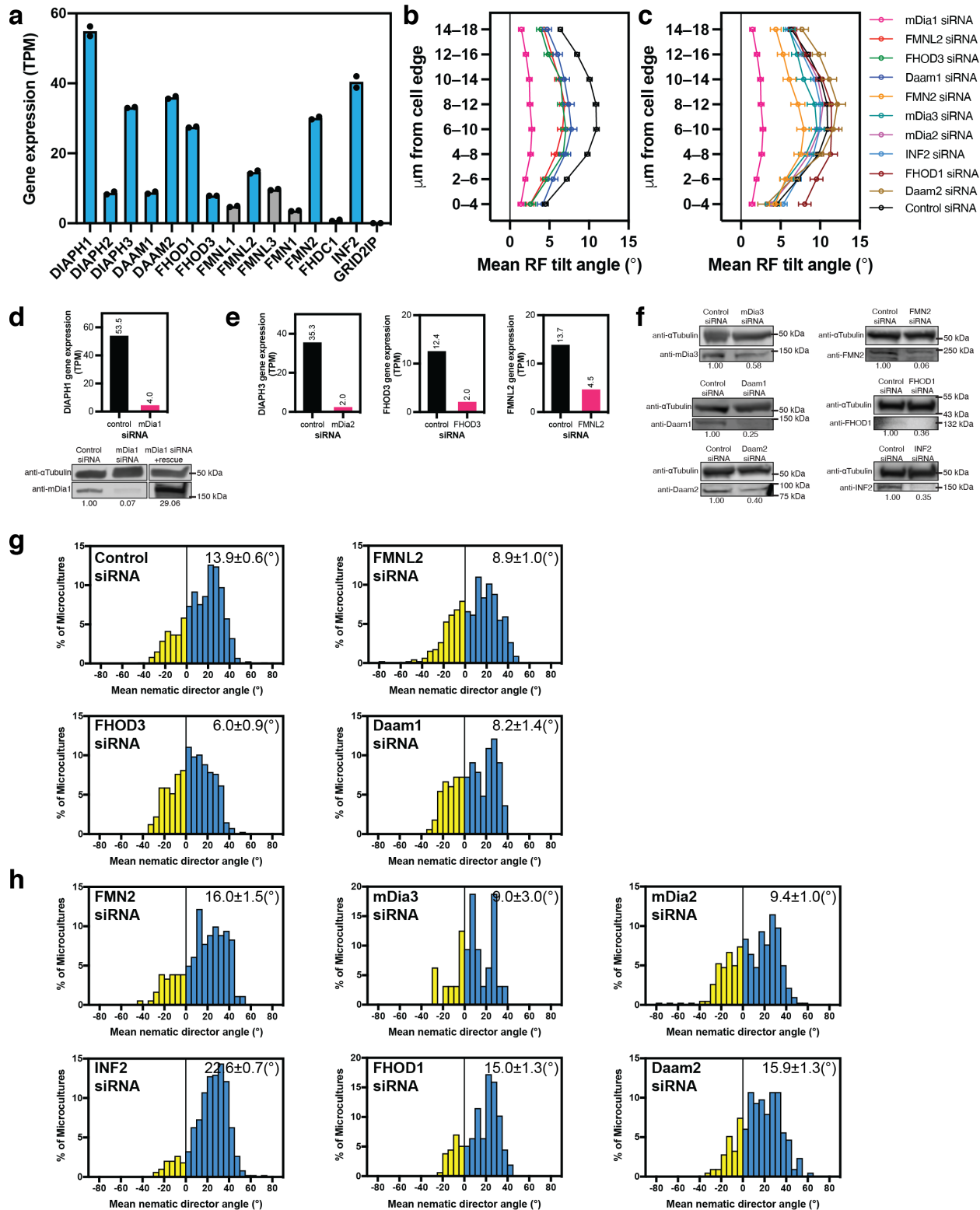


**Supplementary Figure 1. Calculation of radial fibre tilt.**

**a** A fluorescence image of phalloidin-labelled actin cytoskeleton and its corresponding identified radial fibres (RFs) by deep-learning procedure. Scale bar, 10  $\mu\text{m}$ .

**b** Line profile of brightness values (in 16-bit grey scale) of actin cytoskeleton in original image (green) and identified RFs (magenta) along the white line shown in (a). The three peaks along actin cytoskeleton line profile represent RFs of varied brightness and width. Note that three corresponding peaks along magenta line have similar brightness.

**c** The tilts of all radial fibre segments in concentric belts (annuli) located at given distance from the cell edge were measured for each circular cell. The radial fibre segments in the 6–10  $\mu\text{m}$  annulus is shown here. The tilt  $\theta$  of a single radial fibre segment (highlighted in green) was calculated according to the formula below.  $\vec{R}$  connects the cell centroid and intersection of the continuation of the radial fibre segment with the edge of the cell.  $\vec{r}$  connects the cell centroid and intersection of radial fibre with outer edge of the annulus.  $\theta$  and  $\theta_r$  are the angles between the radial fibre segment and  $\vec{R}$  and  $\vec{r}$  respectively.



**Supplementary Figure 2. Effects of knockdown of formin family proteins on left-right asymmetry of actin organisation in individual cells and chiral cell alignment in microcultures.**

**a** Transcriptome profiling of gene expression levels (transcripts per million; TPM) of the 15 mammalian formin members identified by RNA-sequencing (RNA-seq) (mean values of n= 2 experiments) in human fibroblasts. Cyan bars represent formins examined in this study.

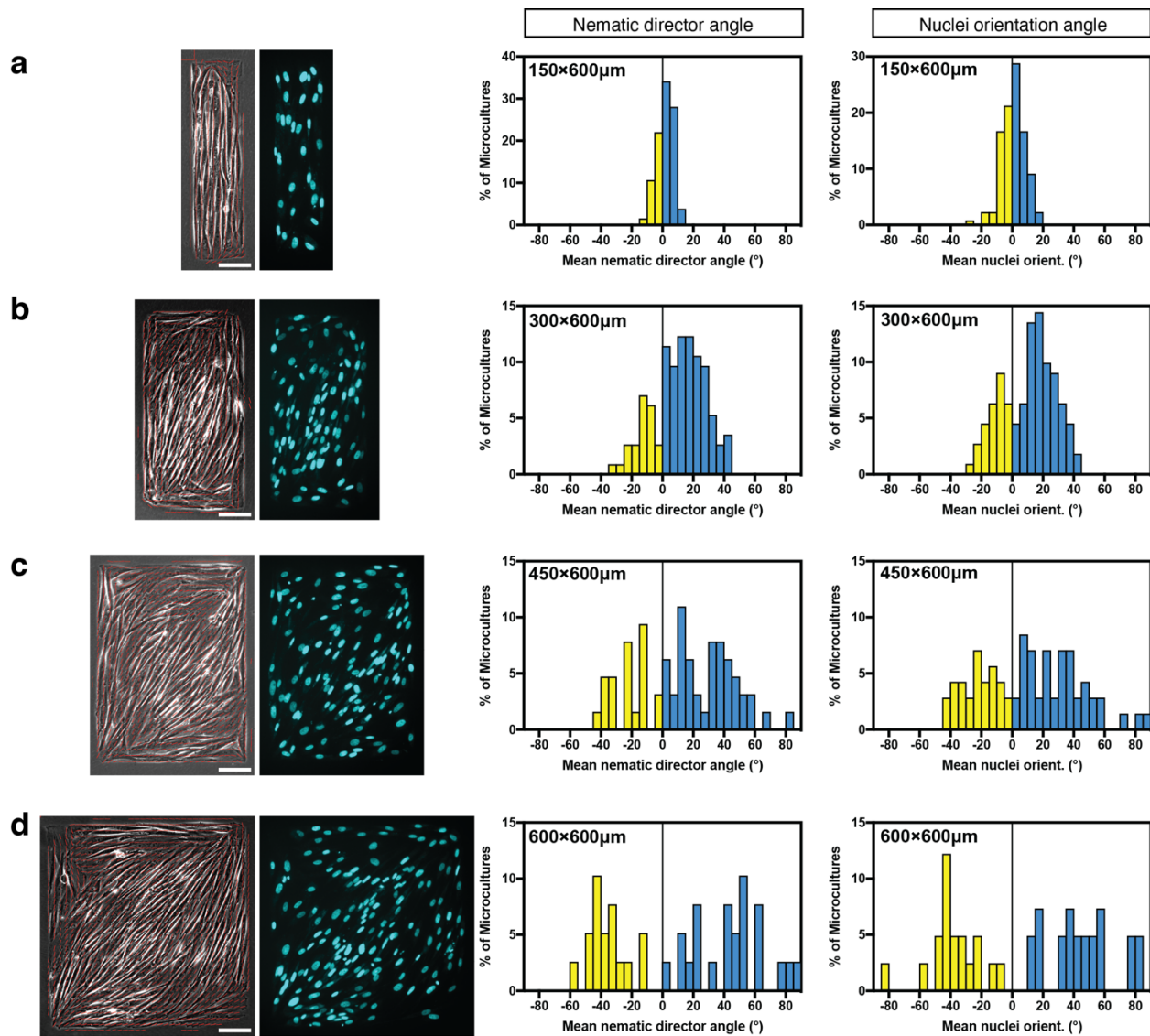
**b,c** Average values of radial fibre (RF) tilts (mean $\pm$ SEM) as a function of the distance of annuli from the cell edge for two groups of formin family members, knockdown of which either reduced (**b**) or did not apparently affect (**c**) actin cytoskeleton chirality. Classification of formins into group (**b**) and (**c**) is based on statistical analysis shown in Supplementary Table 1, lines 124–133. Graphs corresponding to mDia1 (magenta) and control (black) siRNAs are presented in both (**b**) and (**c**). Mean $\pm$ SEM of the distribution of average RF tilt in the 6–10  $\mu$ m annulus of the various knockdowns can be found in Supplementary Table 2.

**d** siRNA knockdown of mDia1 (DIAPH1) in fibroblasts as verified by RNA-profiling (top) and western blot (bottom). Rescue of mDia1 knockdown cells by co-transfection with mDia1 full-length plasmid is shown in lane 3 of western blot.

**e,f** Gene expression levels (**e**) and western blots (**f**) showing individual formin protein levels in scrambled control siRNA and formin specific siRNAs -treated cells. Fold change in protein expression levels normalised to loading control ( $\alpha$ -Tubulin) between control siRNA-treated cell (expression taken as 1.00) and cells treated with corresponding siRNAs are indicated at the bottom of each blot in (**d**) and (**f**).

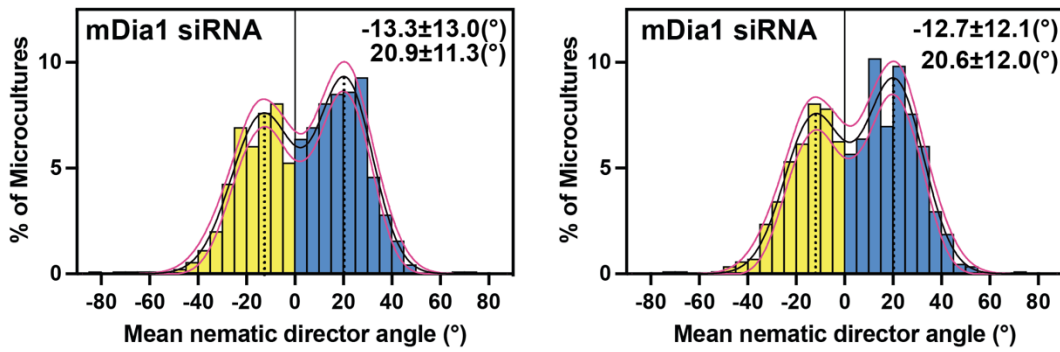
**g,h** Quantification of chiral alignment of cells with formin protein knockdowns in microcultures as characterised by mean nematic directors angle. Mean $\pm$ SEM values are indicated at the top right corner of each histogram. Negative and positive values are coloured in yellow and cyan respectively.

Sample sizes (n) for (**b**), (**c**), (**g**) and (**h**) can be found in Supplementary Table 2. See uncropped blots in Source Data. For statistical analysis, see Supplementary Table 1, lines 124–166.



**Supplementary Figure 3. Relationship between aspect ratio of rectangular micropattern and left-right asymmetric cell alignment in microcultures.**

**a-d** Phase-contrast image overlaid with local nematic directors (red lines) (left) and the corresponding image of cell nuclei stained with Hoechst 33342 (right) of microcultures on 150 $\times$ 600 (a), 300 $\times$ 600 (b), 450 $\times$ 600 (c) and 600 $\times$ 600 (d)  $\mu\text{m}$  rectangular micropatterns. Histograms showing distributions of the values of mean nematic directors angle and mean nuclei orientation characterising individual microcultures on rectangles under respective conditions. The histograms were built based on average local cell orientation (nematic directors angle) values from a single experiment comprising 132 (a), 114 (b), 64 (c) and 39 (d) microcultures, or average nuclei orientation values from 132 (a), 111 (b), 71 (c) and 41 (d) microcultures respectively. Negative and positive values are coloured in yellow and cyan respectively. Scale bars, 100  $\mu\text{m}$  (a-d).

**a****b**

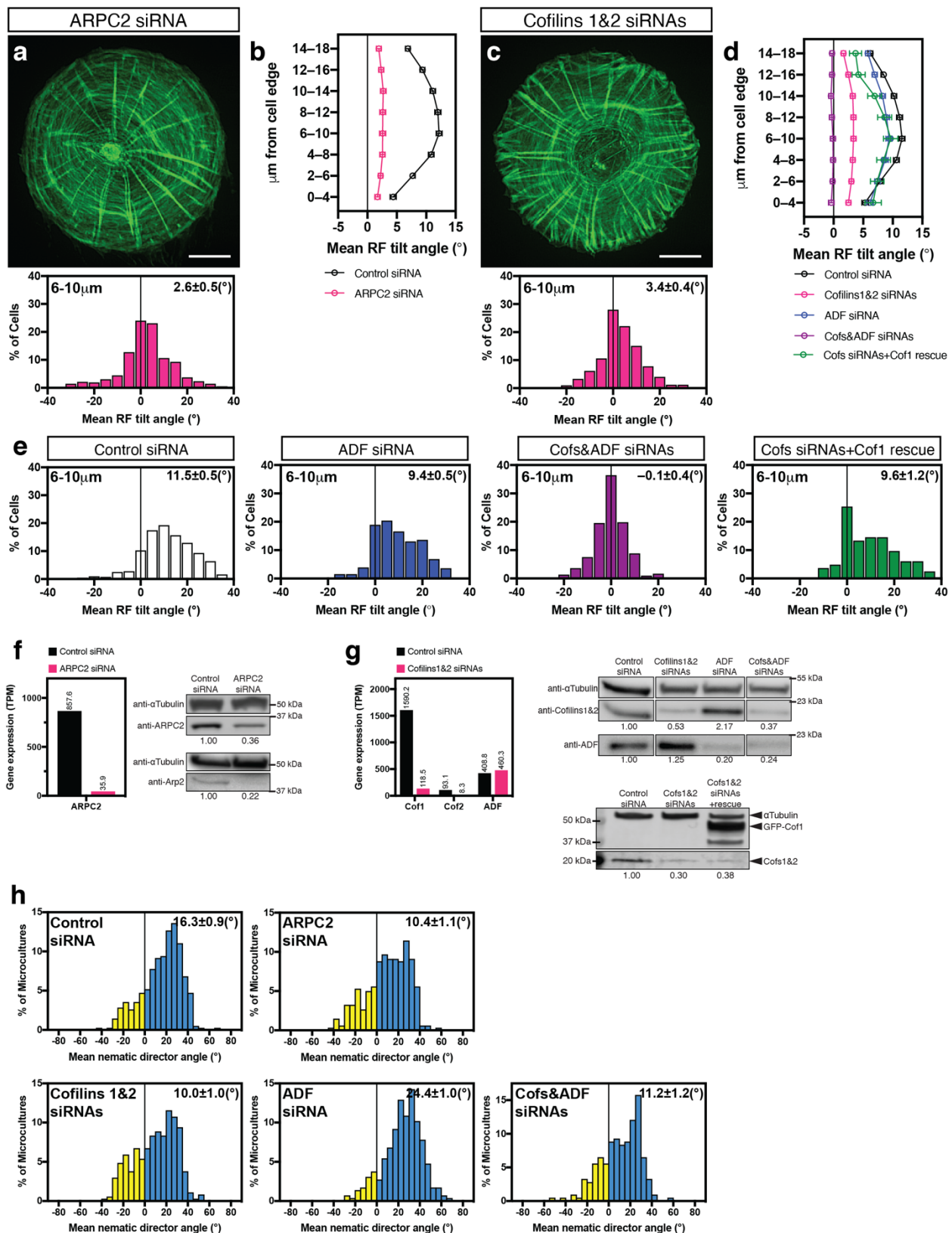
Comparison of Fits	
Null hypothesis	Gaussian
Alternative hypothesis	Sum of two Gaussians

Figure	Parameter	Condition	P value	Representation as a sum of 2 gaussian distribution				95% CI (profile likelihood)	
				Mean1	SD1	Mean2	SD2	95% CI (Mean1)	95% CI (Mean2)
2d	Mean nematic director angle	mDia1 siRNA	<0.0001	-13.25	12.96	20.9	11.25	-15.73 to -10.28	18.86 to 22.92
2d	Mean nuclei orient.	mDia1 siRNA	<0.0001	-12.73	12.1	20.64	11.98	-15.38 to -9.318	18.27 to 23.13
Supp Fig. 2g	Mean nematic director angle	FMNL2 siRNA	<0.0001	-9.25	11.66	21.44	12.97	-13.45 to -0.0223	18.09 to 26.37
Supp Fig. 2h	Mean nematic director angle	mDia2 siRNA	<0.0001	-1.437	17.8	28.97	7.549	-5.886 to 5.028	27.16 to 30.54
4c	Mean nematic director angle	20nM LatA	<0.0001	-26.87	10.11	1.255	14.41	-28.46 to -25.28	-11.11 to 7.739
4c	Mean nematic director angle	5nM SwinA	<0.0001	-19.4	15.68	18.96	11.67	-21.47 to -18.03	13.75 to 22.02
Supp Fig. 7e	Mean nuclei orient.	5nM SwinA	<0.0001	-24.69	12.93	7.947	16.21	-27.49 to -22.16	-5.788 to 14.52
7f	Mean nematic director angle	Pfn1 & $\alpha$ Actn1 siRNAs	0.0002	-4.384	15.14	27.82	8.323	-10.36 to 5.993	22.82 to 31.88
7g	Mean nematic director angle	CapZ $\beta$ siRNA	<0.0001	-16.84	11.61	16.16	10.02	-23.81 to -12.16	3.446 to 20.28
Supp Fig. 7e	Mean nuclei orient.	CapZ $\beta$ siRNA	<0.0001	-19.14	10.23	12.3	11.85	-21.67 to -16.57	6.811 to 16.15
7d	Mean RF tilt angle	LatA + $\alpha$ Actn1 siRNA	0.0043	-7.736	12.56	19.38	5.023	-9.934 to -5.357	16.73 to 21.84

#### Supplementary Figure 4. Fitting of histogram as a sum of two Gaussian distributions.

**a** The distribution of angles of mean nematic director angle (left) or mean nuclei orientation (right) characterising mDia1 knockdown cells alignment in microcultures shows bimodality. The fit as a sum of two Gaussians distribution is represented by the black line bound by a pair of magenta lines that define the 95% confidence bands. The means for each individual Gaussian distribution is indicated by the black dotted line on the graph and their values (mean $\pm$ SD) are shown at the top right corner. Negative and positive values are coloured in yellow and cyan respectively. See also Fig. 2d.

**b** A list summarising other conditions that satisfied the fit as a sum of two Gaussians as defined by a comparison of fits using a null hypothesis (Gaussian fit) versus an alternative hypothesis (Sum of two Gaussians fit) as implemented in GraphPad Prism Software (version 9.4.1). Bimodal distribution is represented by 1 negative (Mean1) and 1 positive (Mean2) means corresponding to opposite chirality signs. See Methods for more details.



**Supplementary Figure 5. Quantification of left-right asymmetry in actin organisation and chiral alignment of cells with knockdown of ARPC2 and actin-depolymerisation factor**

**(ADF)/cofilin family proteins.**

**a-d** Actin organisation visualised by phalloidin staining in ARPC2 siRNA (**a**) and Cofilins 1 and 2 siRNAs (**c**) transfected cells 6 hours following cell plating on circular pattern. The histograms (**a** and **c**) show the distribution of average radial fibre (RF) tilt in the 6–10  $\mu$ m annulus in cells under corresponding conditions. The graphs (**b** and **d**) show the average values of RF tilts (mean $\pm$ SEM) at 6 hours after plating as a function of the distance of annuli from the cell edge for experiments with ARPC2 (**b**) and ADF/Cofilins (**d**) respectively. Scale bars, 10  $\mu$ m (**a** and **c**).

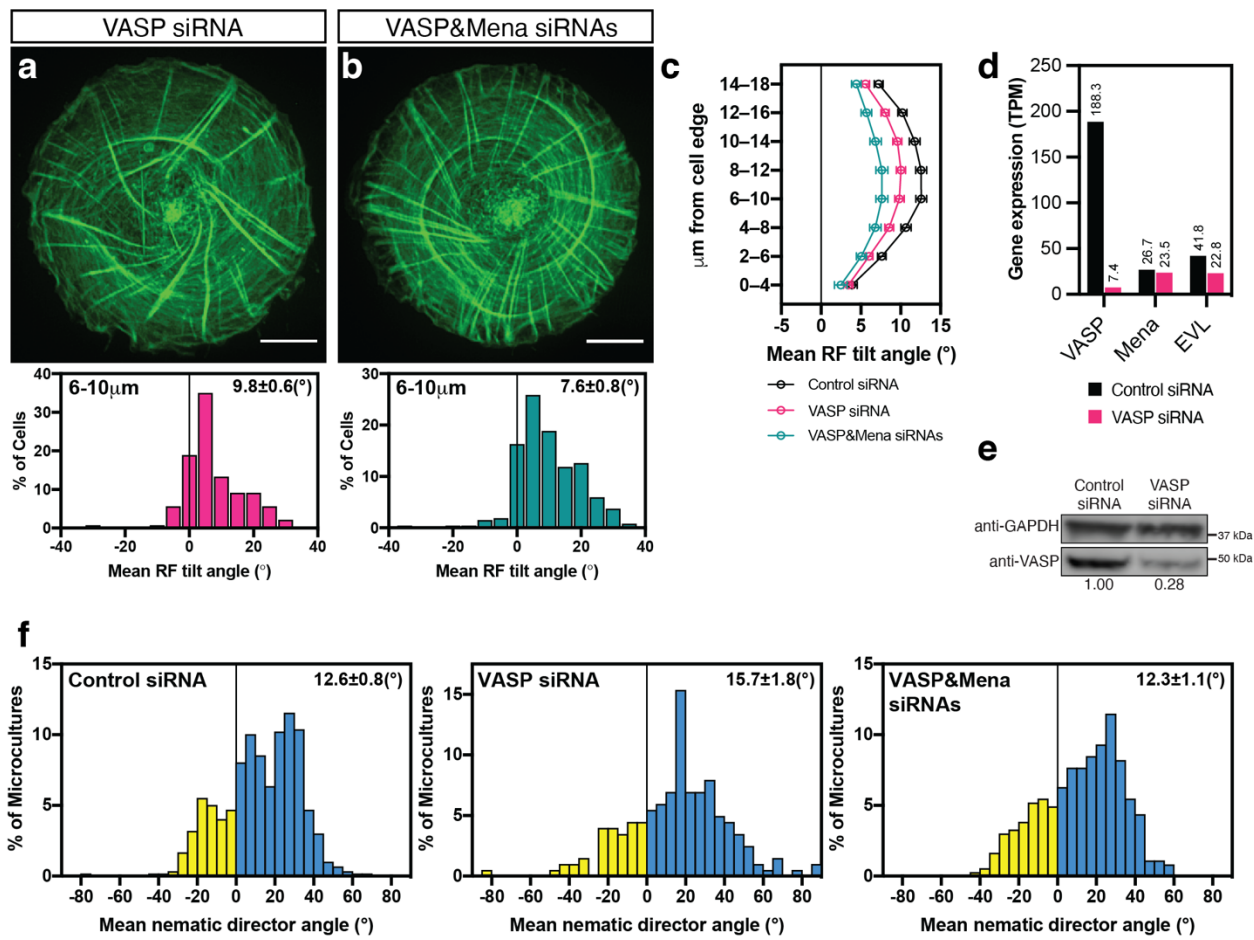
**e** The histograms showing the distribution of average RF tilt in the 6–10  $\mu$ m annulus in cells transfected as indicated at 6 hours after plating. Colour coding in histograms (**c** and **e**) correspond to those indicated in graph (**d**).

**f** siRNA knockdown of ARPC2 in fibroblasts as verified by RNA-profiling (left) and western blot (right upper). Level of Arp2 is also reduced in ARPC2 siRNA transfected cells as compared to control cells (right lower).

**g** siRNA knockdown of ADF/Cofilins family proteins as verified by RNA-profiling (left) and western blot (right upper). Rescue of Cofilins 1&2 knockdown cells by co-transfection with GFP-Cofilin 1 full-length plasmid is shown in lane 3 of western blot (right lower). Fold change in protein level relative to loading control ( $\alpha$ -Tubulin) and normalised to protein expression in control cells (expression ratio = 1.00) are indicated at the bottom of each blot result in (**f**) and (**g**).

**h** Quantification of chiral alignment of cells in microcultures at 48 hours after plating under corresponding conditions as characterised by mean nematic directors angle. Mean $\pm$ SEM values are indicated at the top right corner of each histogram. Negative and positive values are coloured in yellow and cyan respectively.

Sample sizes (n) for (**a**) to (**e**) and (**h**) can be found in Supplementary Table 2. See uncropped blots in Source Data. For statistical analysis, see Supplementary Table 1, lines 167–187.



**Supplementary Figure 6. Effect of knockdown of actin filament elongator VASP on left-right asymmetry of actin organisation in individual cells and chiral cell alignment in microcultures.**

**a,b** Actin organisation visualised by phalloidin staining in VASP siRNA (**a**) and VASP and Mena siRNAs (**b**) transfected cells 6 hours following cell plating on circular pattern. The histograms show the distribution of average RF tilt in the 6–10  $\mu$ m annulus in cells at 6 hours after plating under corresponding conditions. Scale bars, 10  $\mu$ m.

**c** Average values of RF tilts (mean $\pm$ SEM) as a function of the distance of annuli from the cell edge. Histograms and mean $\pm$ SEM values of these average RF tilts (in **a-c**) were obtained from 214 control cells, 271 VASP knockdown cells and 143 VASP and Mena knockdown cells. Colour coding in histograms (**a** and **b**) correspond to those indicated in graph (**c**).

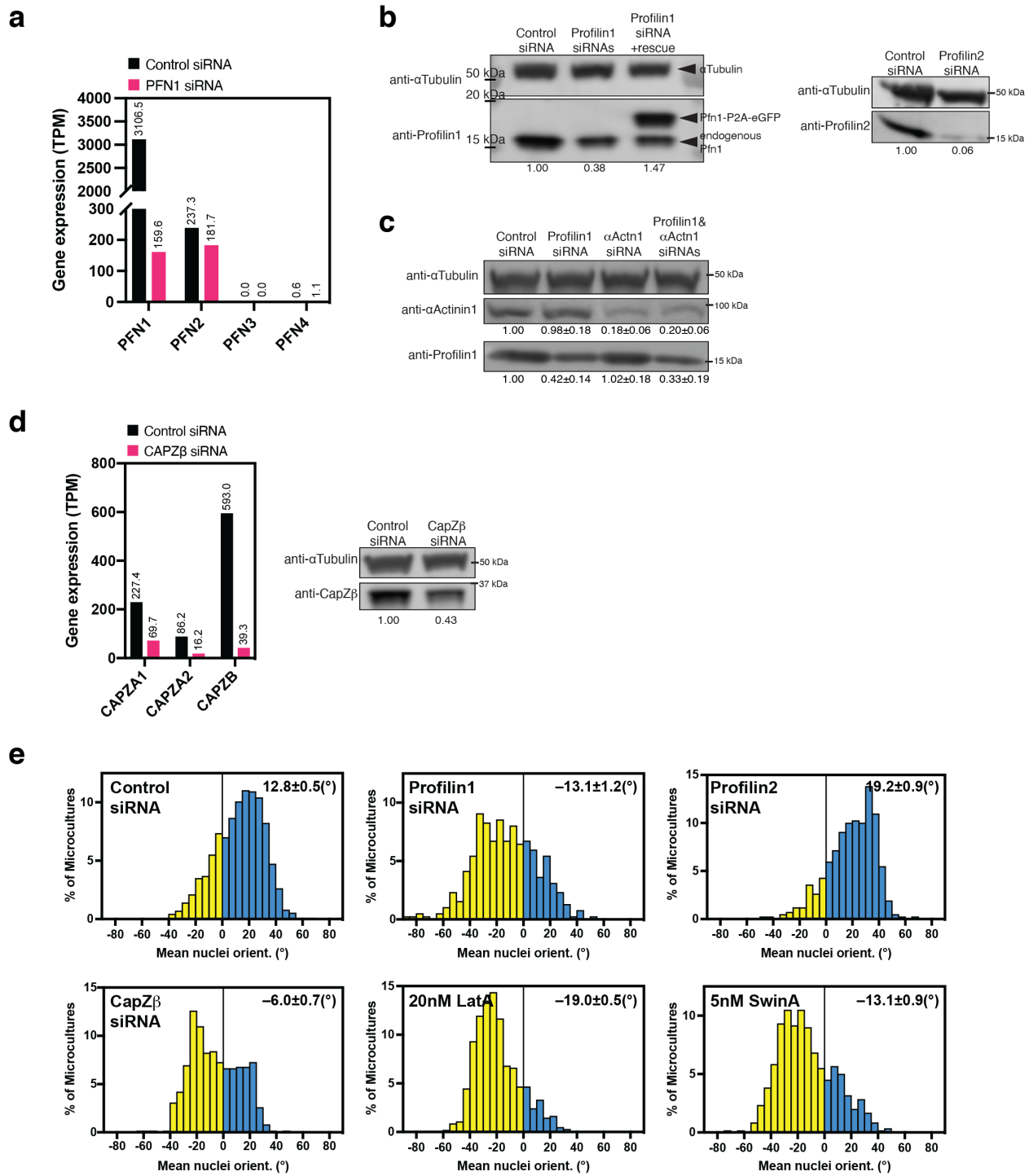
**d** Transcriptome profiling of gene expression levels (transcripts per million; TPM) of the Ena/VASP family proteins by RNA-sequencing in control- and VASP- siRNA transfected human fibroblasts.

**e** Western blot showing VASP level in cells treated with scrambled (control) or anti-VASP siRNA; GAPDH was used as a loading control. Fold change in VASP protein level relative to

loading control and normalised to protein expression level in control cells (expression ratio = 1.00) are indicated at the bottom of the blot. See uncropped blots in Source Data.

**f** Histograms showing distributions of the values of mean nematic directors angle characterising individual microcultures on rectangles under corresponding conditions. The histograms and mean $\pm$  SEM values were built based on average local cell orientation (nematic directors) values from 598 control, 202 VASP knockdown and 366 VASP and Mena knockdown microcultures. Negative and positive values are coloured in yellow and cyan respectively.

For statistical analysis, see Supplementary Table 1, lines 188–196.



**Supplementary Figure 7. Knockdown of profilin 1 and CapZ $\beta$  protein and their effect on nuclei orientation of cells in microcultures.**

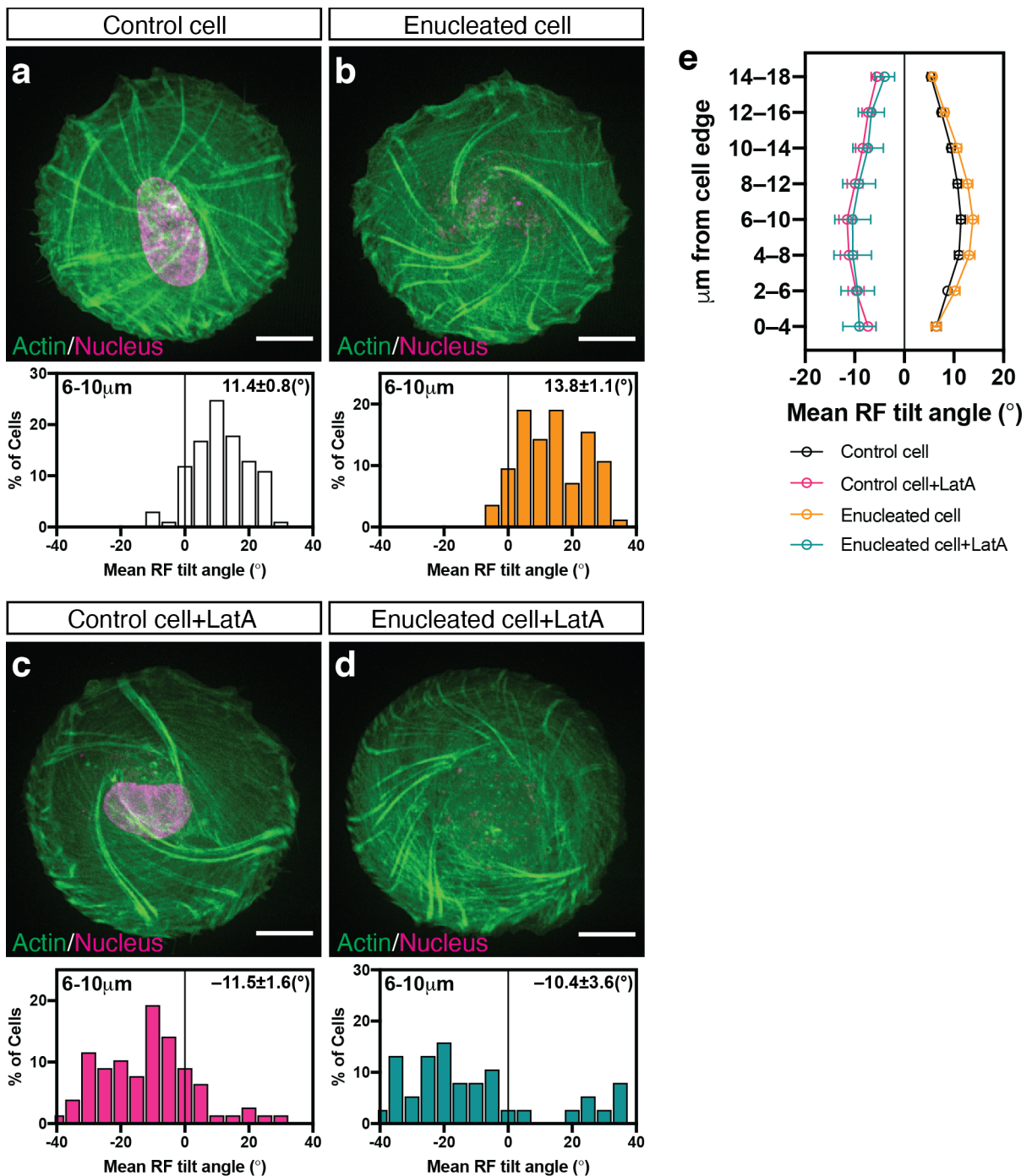
**a** Transcriptome profiling of gene expression levels (transcripts per million; TPM) of Profilin (PFN) 1-4 isoforms identified by RNA-sequencing in control siRNA and profilin 1 siRNA transfected cells.

**b** Western blots showing profilin 1 (left) and profilin 2 (right) levels in cells treated with scrambled (control), profilin 1 siRNA or profilin 2 siRNA;  $\alpha$ -tubulin was used as a loading control. Rescue of profilin 1 knockdown cells by co-transfection with Pfn1-P2A-eGFP full-length plasmid is shown in lane 3 of western blot (left).

**c** Expression level of profilin 1 and  $\alpha$ -actinin1 ( $\alpha$ Actn1) in single and double siRNAs transfected cells were examined (mean $\pm$ SD; n= 3 experiments).

**d** Transcriptome profiling of gene expression levels of CapZA1, CapZA2 and CapZB identified by RNA-sequencing in control siRNA and CapZ $\beta$  siRNA transfected cells. Western blot showing CapZ $\beta$  levels in cells treated with scrambled (control) or CapZ $\beta$  siRNA;  $\alpha$ -tubulin was used as a loading control. Fold change in protein level relative to loading control ( $\alpha$ -Tubulin) and normalised to protein expression in control cells (expression ratio = 1.00) are indicated at the bottom of each blot results in **b-d**. See uncropped blots in Source Data.

**e** Quantification of chiral alignment of cells in microcultures under respective conditions as characterised by mean nuclei orientation. The histograms were built based on average nuclei orientation values from 1144 control, 386 profilin 1 knockdown, 420 profilin 2 knockdown, 620 CapZ $\beta$  knockdown microcultures and 1031 LatA- and 601 SwinA-treated microcultures. Mean $\pm$ SEM values are indicated at the top right corner of each histogram. Negative and positive values are coloured in yellow and cyan respectively. See also Fig. 4c. For statistical analysis, see Supplementary Table 1, lines 197–207.

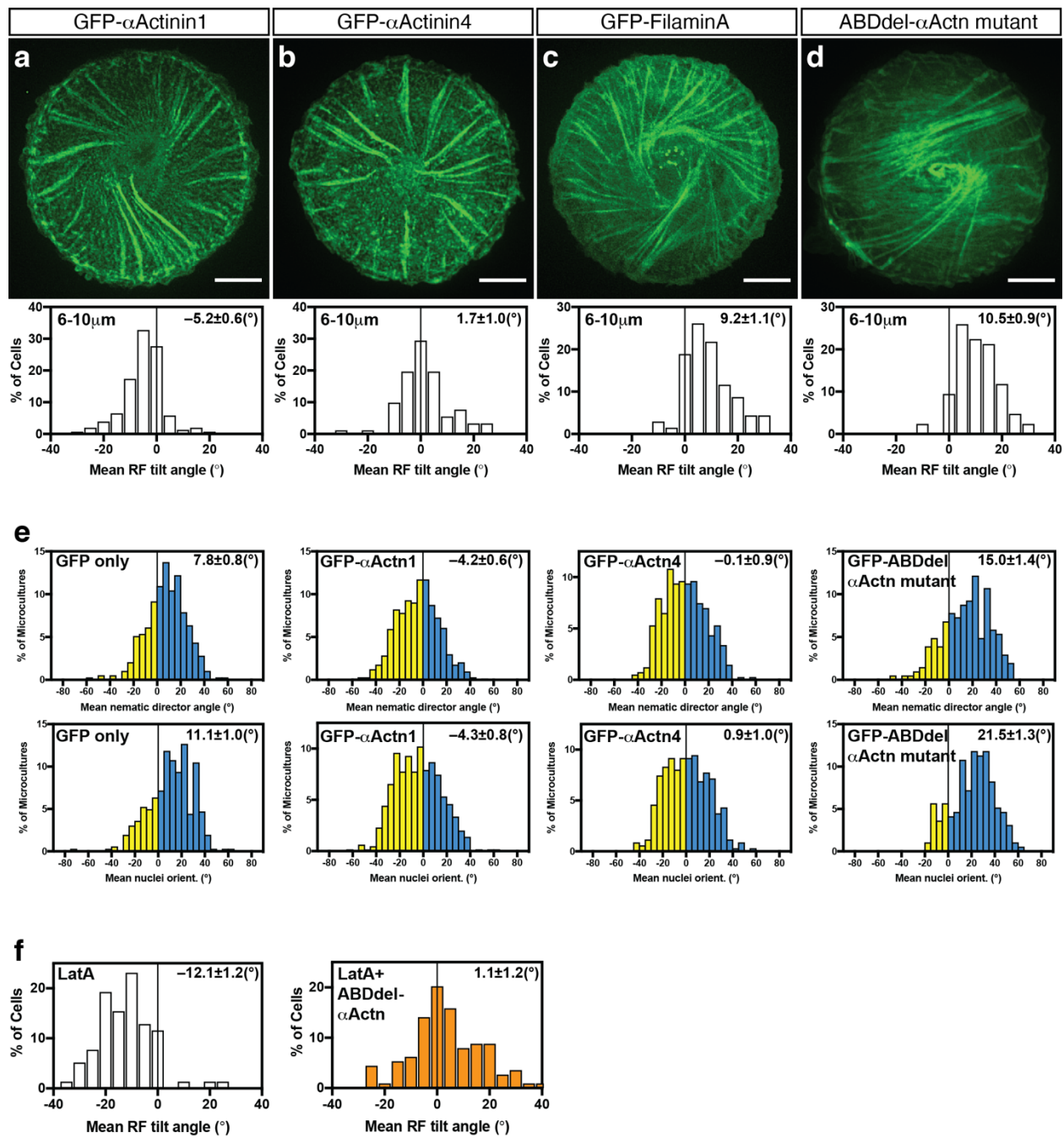


**Supplementary Figure 8. Evaluation of chirality in enucleated and latrunculin A-treated enucleated cells.**

**a-d** Actin organisation (green) as visualised by LifeAct-GFP and nuclei as labelled by Hoechst 33342 (pseudo-coloured magenta) in control cell (**a**), enucleated cell (**b**), control cell treated with 20nM Latrunculin A (LatA) (**c**) and enucleated cell treated with 20nM LatA (**d**). The histograms

**(a-d)** show the distribution of average RF tilt in the 6–10  $\mu\text{m}$  annulus in cells under corresponding conditions. Scale bars, 10  $\mu\text{m}$  **(a-d)**.

**e** Average values of RF tilts (mean $\pm$ SEM) as a function of the distance of annuli from the cell edge. Histograms and mean $\pm$ SEM values of these average RF tilts (in **a-e**) were calculated from 101 control cells, 84 enucleated cells, 78 LatA-treated control cells and 38 LatA-treated enucleated cells. Colour coding in histograms **(a-d)** correspond to those indicated in graph **(e)**. See also Supplementary Movie 6. For statistical analysis, see Supplementary Table 1, lines 208–215.



**Supplementary Figure 9. Effects of overexpression of  $\alpha$ -actinin1 and other crosslinking proteins on radial fibre (RF) tilt and cell alignment in microcultures.**

**a** Image of GFP- $\alpha$ -actinin1 expressing cell showing clockwise actin organisation (as shown in Fig. 6a).

**b** Image of GFP- $\alpha$ -actinin4 expressing cell showing radial actin organisation.

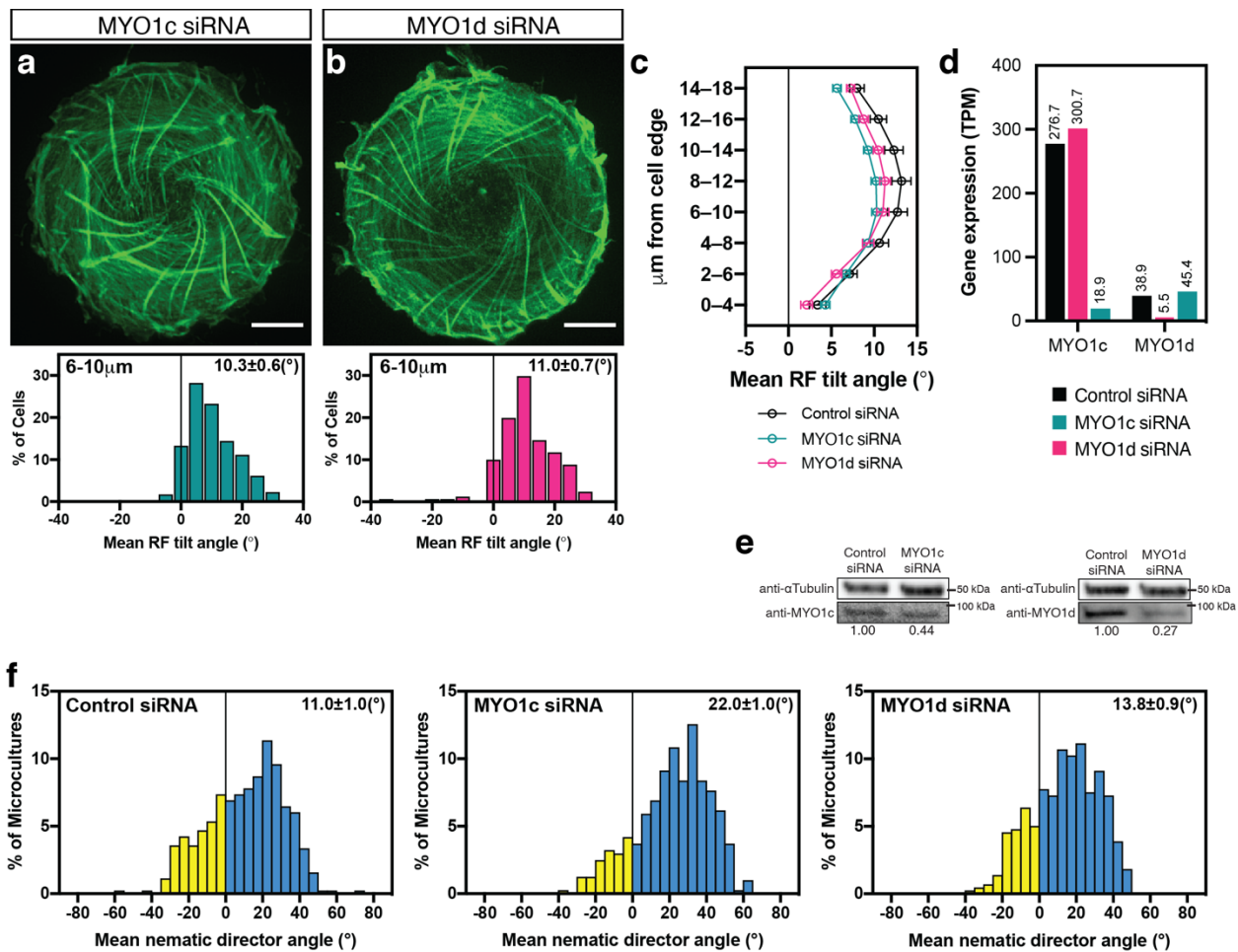
**c** Image of GFP-Filamin A expressing cell showing anti-clockwise actin organisation.

**d** Anti-clockwise actin organisation in GFP-ABDdel- $\alpha$ -actinin mutant expressing cell visualised by mRuby-LifeAct (pseudo-coloured green) (as shown in Fig. 6e). The histograms (**a-d**) show the distribution of average RF tilt in the 6–10  $\mu\text{m}$  annulus in cells under corresponding conditions. See also Fig. 6b and 6f. Scale bars, 10  $\mu\text{m}$  (**a-d**).

**e** Quantification of chiral alignment of cells transfected as indicated in microcultures as characterised by mean nematic directors angle (upper row) or mean nuclei orientation (lower row). The histograms were built based on average local cell orientation (nematic directors) values from 394 GFP-only transfected, 745 GFP- $\alpha$ -actinin1 transfected, 417 GFP- $\alpha$ -actinin4 transfected and 206 GFP-ABDdel- $\alpha$ -actinin mutant transfected microcultures respectively, or average nuclei orientation values from 364 GFP-only transfected cells, 659 GFP- $\alpha$ -actinin1 transfected, 350 GFP- $\alpha$ -actinin4 transfected and 195 GFP-ABDdel- $\alpha$ -actinin mutant transfected microcultures respectively. Histograms depicting the distribution of mean nematic directors angle of GFP-only, GFP- $\alpha$ -actinin1 and GFP-ABDdel- $\alpha$ -actinin mutant expressing cells are also shown in Fig. 6d and 6h. Negative and positive values are coloured in yellow and cyan respectively.

**f** Effect of inhibition of  $\alpha$ -actinin1 crosslinking function by GFP-ABDdel- $\alpha$ -actinin mutant on reversal of RF tilt by latrunculin A (LatA) treatment. Histograms showing the distribution of average RF tilt in the 6–10  $\mu\text{m}$  annulus in 20nM LatA-treated cells (left) ( $n= 78$  cells) versus GFP-ABDdel- $\alpha$ -actinin mutant expressing cells treated with 20nM LatA (right) ( $n= 114$  cells). Mean $\pm$ SEM values are indicated at the top right corner of each histogram.

For statistical analysis, see Supplementary Table 1, lines 56–81 and 216–218.



**a, b** Actin organisation visualised by phalloidin labelling in myosin 1c (MYO1c) siRNA (a) and myosin 1d (MYO1d) siRNA (b) transfected cells 6 hours following cell plating on circular pattern. The histograms show the distribution of average RF tilt in the 6–10  $\mu$ m annulus in cells under corresponding conditions. Scale bars, 10  $\mu$ m.

**c** Average values of RF tilts (mean $\pm$ SEM) as a function of the distance of annuli from the cell edge. Colour coding in histograms (a and b) corresponds to those indicated in graph (c).

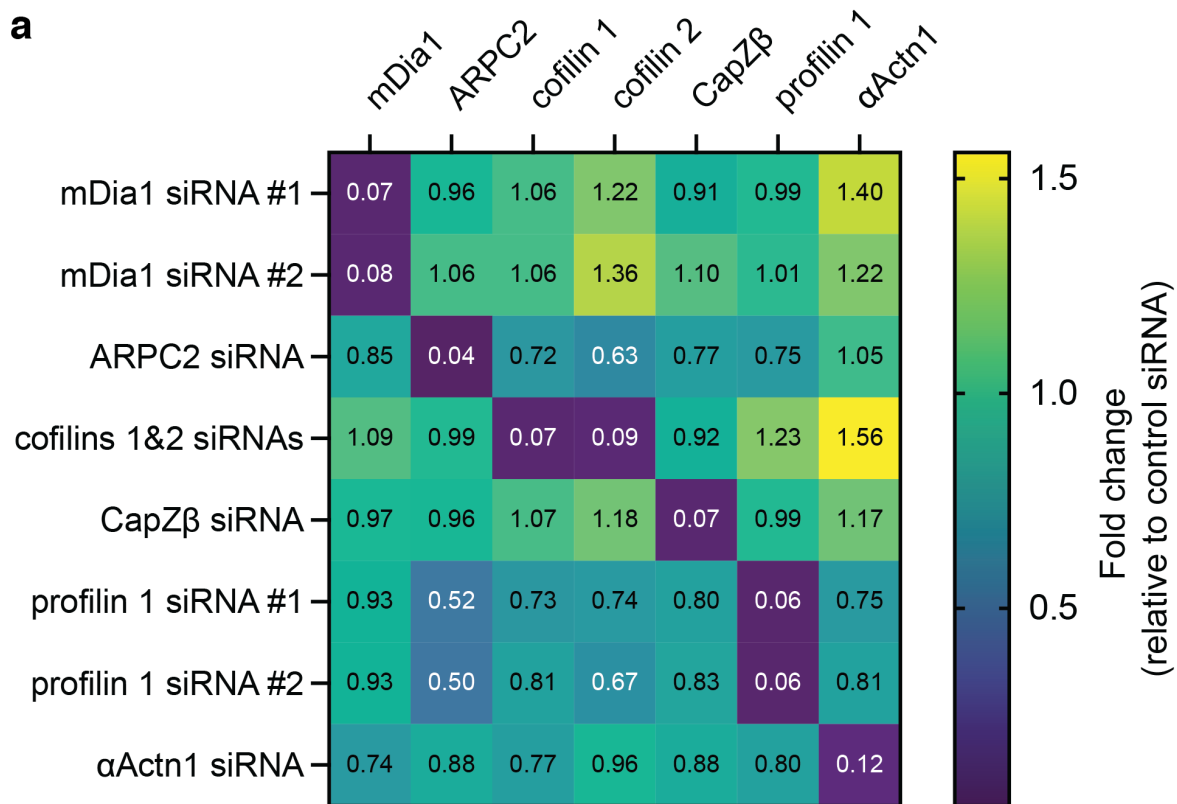
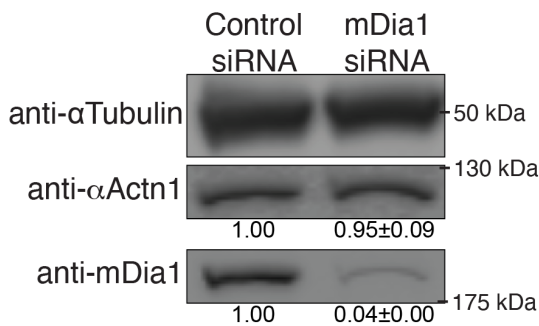
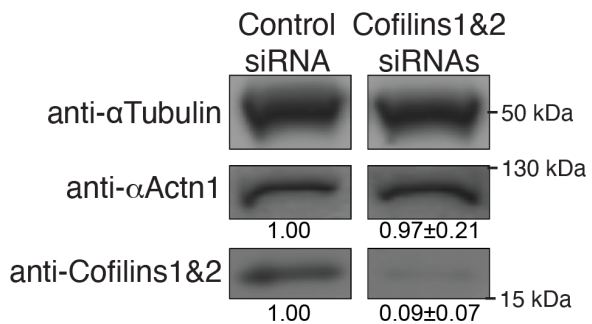
**d** Transcriptome profiling of gene expression levels (transcripts per million; TPM) of MYO1c and MYO1d identified by RNA-sequencing in control-, MYO1c- and MYO1d- siRNA transfected human fibroblasts.

**e** Western blots showing MYO1c (left) or MYO1d (right) level in cells treated with scrambled (control), anti-MYO1c or anti-MYO1d siRNA;  $\alpha$ -tubulin was used as loading controls. Fold change in protein level relative to loading control ( $\alpha$ -Tubulin) and normalised to protein expression in control cells (expression ratio = 1.00) are indicated at the bottom of each blot.

**f** Quantification of chiral alignment of cells in microcultures as characterised by mean nematic directors. Negative and positive values are coloured in yellow and cyan respectively.

Mean $\pm$ SEM values are indicated at the top right corner of each histogram.

Sample sizes (n) for **(a-c)** and **(f)** can be found in Supplementary Table 2. For statistical analysis, see Supplementary Table 1, lines 219–227.

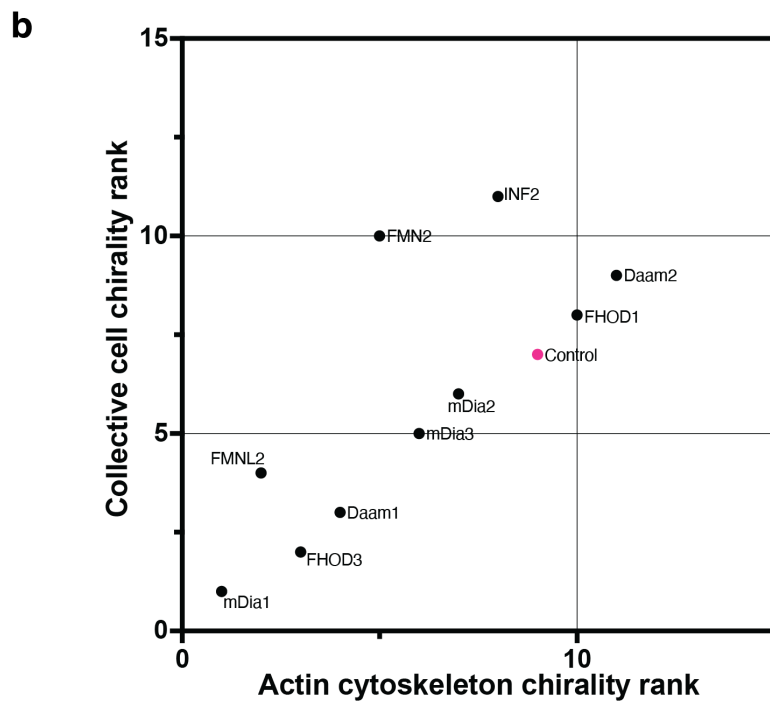
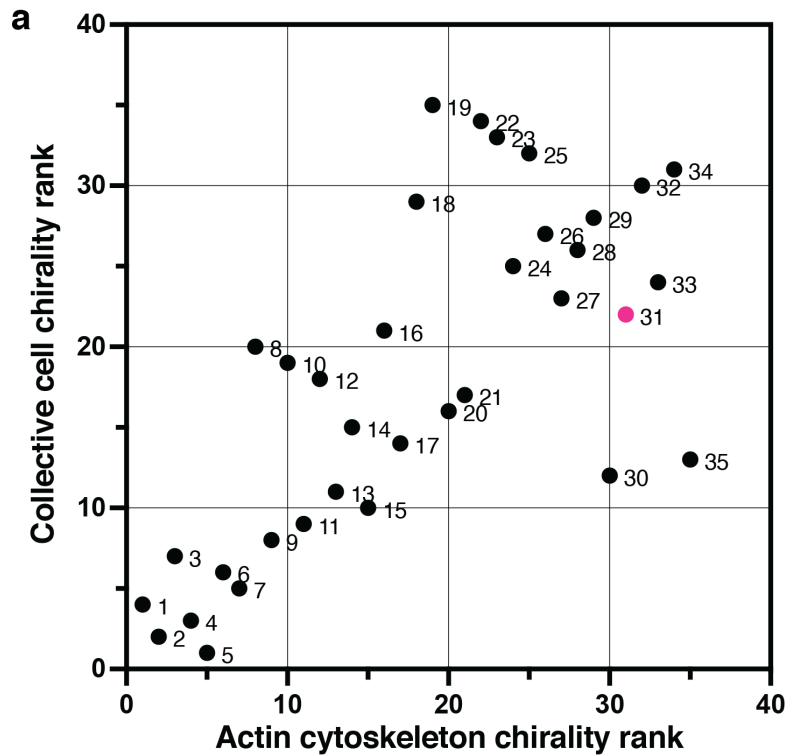
**a****b****c**

**Supplementary Figure 11. Transcriptional profile of major proteins associated with chiral actin organisation.**

**a** Fold changes in gene expression levels (indicated by colour coding and numbers) of major proteins under specific knockdown conditions as assessed by RNA-sequencing. #1 and #2 shows the results of two individual experiments with the same siRNA.

**b,c** Western blots showing mDia1 (**b**), cofilins 1&2 (**c**) and  $\alpha$ -actinin-1 (**b,c**) protein level in cells treated with scrambled (control) (**b,c**), anti-mDia1 (**b**) or anti-cofilins 1&2 (**c**) siRNAs;  $\alpha$ -tubulin was used as loading control. Quantification of fold change relative to control was indicated as mean $\pm$ SD values for 3 experiments.

See measured transcripts per million (TPM) values and uncropped blots in Source Data.

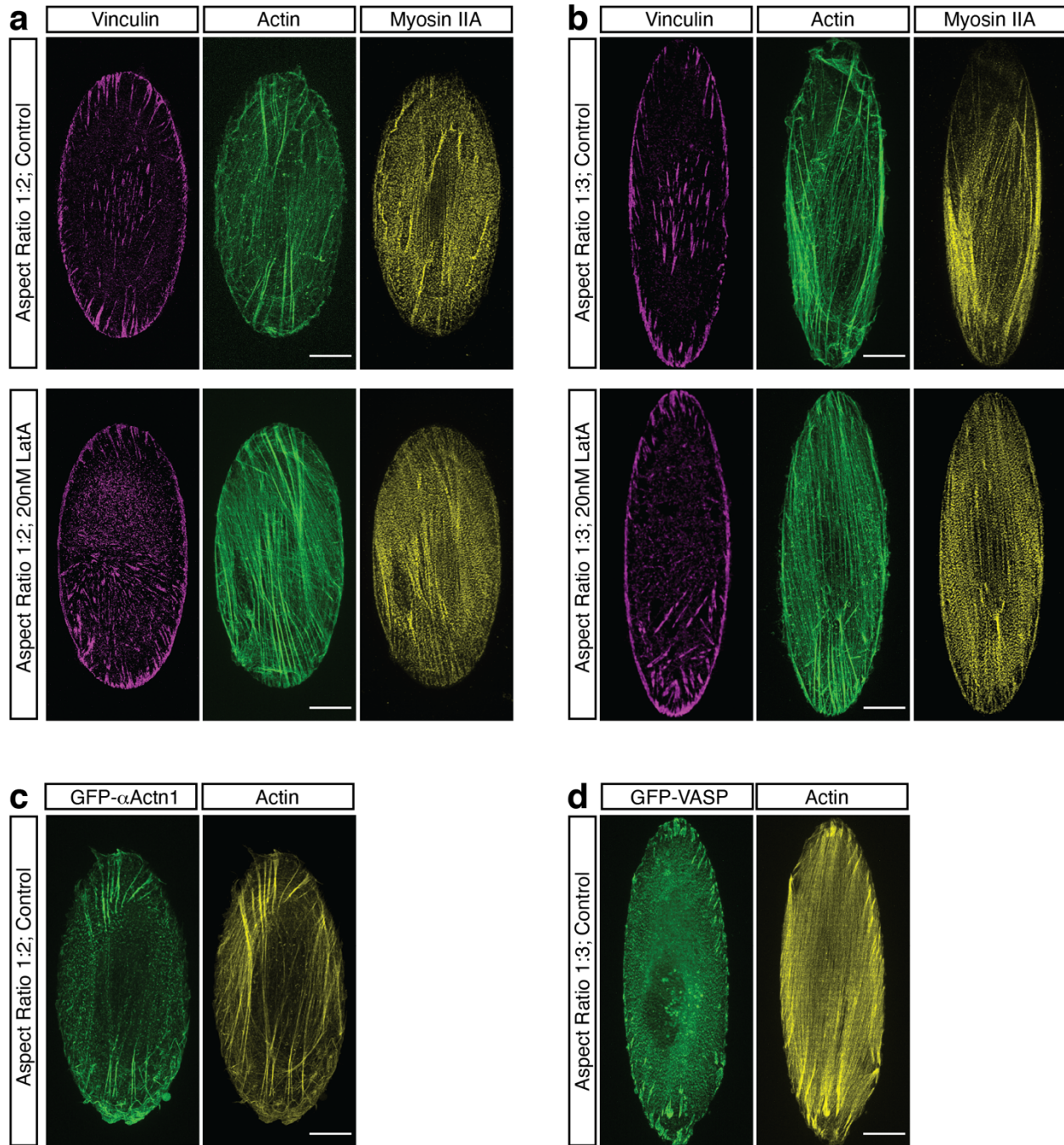


**Supplementary Figure 12. The rank correlation between actin cytoskeleton chirality in individual cells and collective cell chirality in microcultures.**

**a** Each numbered dot represents average data from pooled experiments under respective conditions indicated in the list on the right. All dots are ranked according to actin cytoskeleton

chirality value and collective chirality value. Actin cytoskeleton chirality is defined as the mean radial fibre tilt angle at the 6–10  $\mu\text{m}$  annulus. Collective chirality is defined as the mean nematic director angle for rectangular microcultures. Dots are indexed in ascending actin cytoskeleton chirality rank ( $x$ -axis). Position of control cell (31) is shown in magenta. Numbers of cells and microcultures analysed and the corresponding mean values can be found in Supplementary Table 2. See also Fig. 8. Spearman’s rank correlation coefficient,  $r = 0.7081$ ,  $****p < 0.0001$ .

**b** The rank correlation between actin cytoskeleton chirality in individual cells and collective cell chirality in microculture for the cells with knockdowns of formin family members. The ranking of the chirality values was performed in the same way as in **(a)** and indicated in the list on the right. Position of control cell is shown in magenta. Spearman’s rank correlation coefficient,  $r = 0.7545$ ,  $**p = 0.0098$ .



**Supplementary Figure 13. The system of chiral stress fibres in cells on an elliptical pattern.**

**a,b** Focal adhesions were visualised by anti-vinculin antibody staining, actin fibres by phalloidin staining and myosin IIA by anti-myosin-IIA antibody staining in cells fixed at 6 hours after spreading on an elliptical micropattern with different aspect ratios. Cells were either untreated (control) or treated with 20nM latrunculin A (LatA).

**c,d** Actin fibres were visualised by phalloidin staining,  $\alpha$ -actinin1 ( $\alpha$ Actn1) by transfection with GFP- $\alpha$ Actn1 (**c**) and VASP by transfection with GFP-VASP (**d**) in control cells on elliptical

micropatterns. GFP- $\alpha$ Actn1 (**c**) strongly localised to radial fibres while GFP-VASP (**d**) localised to focal adhesions. Note the right-handed and left-handed tilt of actomyosin stress fibres relative to the long axis of the ellipses in control and latrunculin-treated cells respectively.

Scale bars, 10  $\mu$ m (**a-d**). See also Fig. 9.

**Supplementary Table 1.** Statistical analysis of data.

Line	Figure	Statistical Test	Parameters	Comparison	P-value	P-value summary	
1	1i vs. 1j	Kruskal-Wallis	Mean RF tilt angle	Control siRNA vs. mDia1 siRNA	<0.0001	****	
2	1j vs. 1k			mDia1 siRNA vs. mDia1 siRNA+rescue	<0.0001	****	
3	1i vs. 1k			Control siRNA vs. mDia1 siRNA+rescue	>0.9999	ns	
4	1i	Wilcoxon test	Mean RF tilt angle	Median of Control siRNA vs. zero	<0.0001	****	
5	1j			Median of mDia1 siRNA vs. zero	<0.0001	****	
6	1k			Median of mDia1 siRNA+rescue vs. zero	<0.0001	****	
7	2d	Kruskal-Wallis	Mean nematic director angle	Control siRNA vs. mDia1 siRNA	<0.0001	****	
8	2d			Control siRNA vs. mDia1 siRNA	<0.0001	****	
9	2d			Control siRNA vs. Control siRNA	>0.9999	ns	
10	2d	Wilcoxon test	Mean nematic director angle vs. Mean nuclei orient.	mDia1 siRNA vs. mDia1 siRNA	>0.9999	ns	
11	2d			Median of Control siRNA vs. zero	<0.0001	****	
12	2d			Median of mDia1 siRNA vs. zero	<0.0001	****	
13	2d	Wilcoxon test	Mean nuclei orient.	Median of Control siRNA vs. zero	<0.0001	****	
14	2d			Median of mDia1 siRNA vs. zero	<0.0001	****	
15	3a vs. 3b	Kruskal-Wallis	Mean RF tilt angle	Control siRNA vs. Profilin1 siRNA	<0.0001	****	
16	3b vs. 3c			Pfn1 siRNA vs. Profilin1 siRNA+rescue	<0.0001	****	
17	3a vs. 3c			Control siRNA vs. Profilin1 siRNA+rescue	>0.9999	ns	
18	3a vs. 3d	Wilcoxon test	Mean RF tilt angle	Control siRNA vs. Profilin2 siRNA	<0.0001	****	
19	3a			Median of Control siRNA vs. zero	<0.0001	****	
20	3b			Median of Profilin1 siRNA vs. zero	<0.0001	****	
21	3c	Wilcoxon test	Mean RF tilt angle	Median of Profilin1 siRNA+rescue vs. zero	<0.0001	****	
22	3d			Median of Profilin2 siRNA vs. zero	<0.0001	****	
23	3f vs. 3e	Mann-Whitney	Mean RF tilt angle (8 - 12 $\mu$ m)	Control siRNA #2 vs. CapZ $\beta$ siRNA	<0.0001	****	
24	3e	Wilcoxon test		Median of CapZ $\beta$ siRNA vs. zero	<0.0001	****	
25	3h vs. 3g	Kruskal-Wallis	Mean RF tilt angle	Untreated Control vs. 20nM LatA	<0.0001	****	
26	3h	Untreated Control vs. 5nM SwinA		<0.0001	****		
27	3h	Wilcoxon test		Median of Untreated Control vs. zero	<0.0001	****	
28	3g			Median of 20nM LatA vs. zero	<0.0001	****	
29	3h			Median of 5nM SwinA vs. zero	<0.0001	****	
30	4c	Kruskal-Wallis	Mean nematic director angle	Control siRNA vs. 20nM LatA	<0.0001	****	
31	4c			Control siRNA vs. Profilin1 siRNA	<0.0001	****	
32	4c			Control siRNA vs. Profilin2 siRNA	0.7157	ns	
33	4c	Wilcoxon test	Mean nematic director angle	Control siRNA vs. CapZ $\beta$ siRNA	<0.0001	****	
34	4c			Control siRNA vs. 5nM SwinA	<0.0001	****	
35	4c			Median of Control siRNA vs. zero	<0.0001	****	
36	4c	Wilcoxon test	Mean nematic director angle	Median of 20nM LatA vs. zero	<0.0001	****	
37	4c			Median of Profilin1 siRNA vs. zero	<0.0001	****	
38	4c			Median of Profilin2 siRNA vs. zero	<0.0001	****	
39	4c	Kruskal-Wallis	Mean nematic director angle	Median of CapZ $\beta$ siRNA vs. zero	<0.0001	****	
40	4c			Median of 5nM SwinA vs. zero	<0.0001	****	
41	5a vs. 5b	Kruskal-Wallis	Mean RF tilt angle	Control siRNA vs. Profilin1 siRNA	<0.0001	****	
42	5a vs. 5c			Control siRNA vs. Control siRNA+LatA	<0.0001	****	
43	5a vs. 5d			Control siRNA vs. mDia1 siRNA	<0.0001	****	
44	5a vs. 5e	Wilcoxon test	Mean RF tilt angle	Control siRNA vs. mDia1&Profilin1 siRNAs	<0.0001	****	
45	5a vs. 5f			Control siRNA vs. mDia1 siRNA+LatA	<0.0001	****	
46	5d vs. 5e			mDia1 siRNA vs. mDia1&Profilin1 siRNAs	<0.0001	****	
47	5d vs. 5f	Kruskal-Wallis	Mean RF tilt angle	mDia1 siRNA vs. mDia1 siRNA+LatA	<0.0001	****	
48	5e vs. 5b			mDia1&Profilin1 siRNAs vs. Profilin1 siRNA	>0.9999	ns	
49	5f vs. 5c			mDia1 siRNA+LatA vs. Control siRNA+LatA	0.3911	ns	
50	5a	Wilcoxon test	Mean RF tilt angle	Median of Control siRNA vs. zero	<0.0001	****	
51	5b			Median of Profilin1 siRNA vs. zero	<0.0001	****	
52	5c			Median of siControl siRNA+LatA vs. zero	<0.0001	****	
53	5d	Kruskal-Wallis	Mean RF tilt angle	Median of mDia1 siRNA vs. zero	<0.0001	****	
54	5e			Median of mDia1&Profilin1 siRNAs vs. zero	<0.0001	****	
55	5f			Median of mDia1 siRNA+LatA vs. zero	<0.0001	****	
56	6b/Supp Fig. 9a	Kruskal-Wallis	Mean RF tilt angle	Control vs. GFP- $\alpha$ Actn1	<0.0001	****	
57	6b/Supp Fig. 9b			Control vs. GFP- $\alpha$ Actn4	<0.0001	****	
58	6b/Supp Fig. 9c			Control vs. GFP-FIna	>0.9999	ns	
59	6b	Wilcoxon test	Mean RF tilt angle	Median of Control vs. zero	<0.0001	****	
60	6b/Supp Fig. 9a			Median of GFP- $\alpha$ Actn1 vs. zero	<0.0001	****	
61	6b/Supp Fig. 9b			Median of GFP- $\alpha$ Actn4 vs. zero	>0.9999	ns	
62	6b/Supp Fig. 9c			Median of GFP-FIna vs. zero	<0.0001	****	
63	6d/Supp Fig. 9e	Kruskal-Wallis	Mean nematic director angle	GFP only control vs. GFP- $\alpha$ Actn1	<0.0001	****	
64	Supp Fig. 9e			GFP only control vs. GFP- $\alpha$ Actn4	<0.0001	****	
65	Supp Fig. 9e			GFP only control vs. GFP-ABDdel $\alpha$ Actn mutant	0.0016	**	
66	Supp Fig. 9e	Wilcoxon test	Mean nuclei orient.	GFP only control vs. GFP- $\alpha$ Actn1	<0.0001	****	
67	Supp Fig. 9e			GFP only control vs. GFP- $\alpha$ Actn4	<0.0001	****	
68	Supp Fig. 9e			GFP only control vs. GFP-ABDdel $\alpha$ Actn mutant	<0.0001	****	
69	6d/Supp Fig. 9e	Wilcoxon test	Mean nematic director angle	Median of GFP only control vs. zero	<0.0001	****	
70	6d/Supp Fig. 9e			Median of GFP- $\alpha$ Actn1 vs. zero	<0.0001	****	
71	Supp Fig. 9e			Median of GFP- $\alpha$ Actn4 vs. zero	0.7214	ns	
72	6h/Supp Fig. 9e	Kruskal-Wallis	Mean nuclei orient.	Median of GFP-ABDdel- $\alpha$ Actn1 mutant vs. zero	<0.0001	****	
73	Supp Fig. 9e			Median of GFP control vs. zero	<0.0001	****	
74	Supp Fig. 9e			Median of GFP- $\alpha$ Actn1 vs. zero	<0.0001	****	
75	Supp Fig. 9e	Wilcoxon test	Mean RF tilt angle	Median of GFP- $\alpha$ Actn4 vs. zero	0.5323	ns	
76	Supp Fig. 9e			Median of GFP-ABDdel- $\alpha$ Actn1 mutant vs. zero	<0.0001	****	
77	6f	Kruskal-Wallis	Mean RF tilt angle	Control siRNA vs. $\alpha$ Actn1 siRNA	0.1425	ns	
78	6f/Supp Fig. 9d			Control siRNA vs. ABDDel- $\alpha$ Actn mutant	0.0003	***	
79	6f			Median of Control siRNA vs. zero	<0.0001	****	
80	6f	Wilcoxon test	Mean RF tilt angle	Median of $\alpha$ Actn1 siRNA vs. zero	<0.0001	****	
81	6f/Supp Fig. 9d			Median of ABDDel- $\alpha$ Actn1 mutant vs. zero	<0.0001	****	
82	7a	Kruskal-Wallis	Mean RF tilt angle	Control siRNA vs. $\alpha$ Actn1 siRNA	>0.9999	ns	
83	7b			Pfn1 siRNA vs. Pfn1& $\alpha$ Actn1 siRNAs	<0.0001	****	
84	7a vs. 7b			Control siRNA vs. Pfn1 siRNA	<0.0001	****	
85	7a vs. 7b	Wilcoxon test	Mean RF tilt angle	Control siRNA vs. Pfn1& $\alpha$ Actn1 siRNAs	>0.9999	ns	
86	7d			LatA vs. LatA+ $\alpha$ Actn1 siRNAs	<0.0001	****	
87	7a vs. 7d			Control siRNA vs. LatA	<0.0001	****	
88	7a vs. 7d	Kruskal-Wallis	Mean RF tilt angle (8 - 12 $\mu$ m)	Control siRNA vs. LatA+ $\alpha$ Actn1 siRNAs	<0.0001	****	
89	7c			CapZ $\beta$ siRNA vs. CapZ $\beta$ & $\alpha$ Actn1 siRNAs	<0.0001	****	
90	7a vs. 7c			Control siRNA vs. CapZ $\beta$ siRNA	<0.0001	****	
91	7a vs. 7c	Wilcoxon test	Mean RF tilt angle (8 - 12 $\mu$ m)	Control siRNA vs. CapZ $\beta$ & $\alpha$ Actn1 siRNAs	0.0005	***	
92	7a			Median of Control siRNA vs. zero	<0.0001	****	
93	7a			Median of $\alpha$ Actn1 siRNA vs. zero	<0.0001	****	
94	7b	Wilcoxon test	Mean RF tilt angle	Median of $\alpha$ Actn1 siRNA vs. zero	<0.0001	****	
95	7b			Median of Pfn1& $\alpha$ Actn1 siRNAs vs. zero	<0.0001	****	
96	7d			Median of LatA vs. zero	<0.0001	****	
97	7d	Kruskal-Wallis	Mean RF tilt angle (8 - 12 $\mu$ m)	Median of LatA+ $\alpha$ Actn1 siRNA vs. zero	0.1225	ns	
98	7c			Median of CapZ $\beta$ siRNA vs. zero	0.0105	*	
99	7c			Median of CapZ $\beta$ & $\alpha$ Actn1 siRNAs vs. zero	<0.0001	****	
100	7e	Wilcoxon test	Mean nematic director angle	Control siRNA vs. $\alpha$ Actn1 siRNA	<0.0001	****	
101	7f			Pfn1 siRNA vs. Pfn1& $\alpha$ Actn1 siRNAs	<0.0001	****	
102	7e vs. 7f			Control siRNA vs. Pfn1 siRNA	<0.0001	****	
103	7e vs. 7f	Kruskal-Wallis	Mean nematic director angle	Control siRNA vs. Pfn1& $\alpha$ Actn1 siRNAs	>0.9999	ns	
104	7g			CapZ $\beta$ siRNA vs. CapZ $\beta$ & $\alpha$ Actn1 siRNAs	<0.0001	****	
105	7e vs. 7g			Control siRNA vs. CapZ $\beta$ siRNA	<0.0001	****	

106	7e vs. 7g		Control siRNA vs. CapZ $\beta$ & $\alpha$ Actn1 siRNAs LatA vs. LatA+ $\alpha$ Actn1 siRNAs Control siRNA vs. LatA Control siRNA vs. LatA+ $\alpha$ Actn1 siRNA	<0.0001 >0.9999 ns <0.0001 **** <0.0001 ****	
107	7h		Median of Control siRNA vs. zero Median of $\alpha$ Actn1 siRNA vs. zero Median of CapZ $\beta$ siRNA vs. zero Median of CapZ $\beta$ & $\alpha$ Actn1 siRNAs vs. zero Median of LatA vs. zero Median of LatA+ $\alpha$ Actn1 siRNA vs. zero	<0.0001 **** <0.0001 **** <0.0001 **** <0.0001 **** <0.0001 **** <0.0001 ****	
108	7e vs. 7h		Median of Control siRNA vs. zero Median of $\alpha$ Actn1 siRNA vs. zero Median of CapZ $\beta$ siRNA vs. zero Median of CapZ $\beta$ & $\alpha$ Actn1 siRNAs vs. zero Median of LatA vs. zero Median of LatA+ $\alpha$ Actn1 siRNA vs. zero	<0.0001 **** <0.0001 **** <0.0001 **** <0.0001 **** <0.0001 **** <0.0001 ****	
109	7e vs. 7h		Median of Control siRNA vs. zero Median of $\alpha$ Actn1 siRNA vs. zero Median of CapZ $\beta$ siRNA vs. zero Median of CapZ $\beta$ & $\alpha$ Actn1 siRNAs vs. zero Median of LatA vs. zero Median of LatA+ $\alpha$ Actn1 siRNA vs. zero	<0.0001 **** <0.0001 **** <0.0001 **** <0.0001 **** <0.0001 **** <0.0001 ****	
110	7e		Median of Control siRNA vs. zero Median of $\alpha$ Actn1 siRNA vs. zero Median of CapZ $\beta$ siRNA vs. zero Median of CapZ $\beta$ & $\alpha$ Actn1 siRNAs vs. zero Median of LatA vs. zero Median of LatA+ $\alpha$ Actn1 siRNA vs. zero	<0.0001 **** <0.0001 **** <0.0001 **** <0.0001 **** <0.0001 **** <0.0001 ****	
111	7e		Median of Control siRNA vs. zero Median of $\alpha$ Actn1 siRNA vs. zero Median of CapZ $\beta$ siRNA vs. zero Median of CapZ $\beta$ & $\alpha$ Actn1 siRNAs vs. zero Median of LatA vs. zero Median of LatA+ $\alpha$ Actn1 siRNA vs. zero	<0.0001 **** <0.0001 **** <0.0001 **** <0.0001 **** <0.0001 **** <0.0001 ****	
112	7f		Median of Control siRNA vs. zero Median of $\alpha$ Actn1 siRNA vs. zero Median of CapZ $\beta$ siRNA vs. zero Median of CapZ $\beta$ & $\alpha$ Actn1 siRNAs vs. zero Median of LatA vs. zero Median of LatA+ $\alpha$ Actn1 siRNA vs. zero	<0.0001 **** <0.0001 **** <0.0001 **** <0.0001 **** <0.0001 **** <0.0001 ****	
113	7f		Median of Control siRNA vs. zero Median of $\alpha$ Actn1 siRNA vs. zero Median of CapZ $\beta$ siRNA vs. zero Median of CapZ $\beta$ & $\alpha$ Actn1 siRNAs vs. zero Median of LatA vs. zero Median of LatA+ $\alpha$ Actn1 siRNA vs. zero	<0.0001 **** <0.0001 **** <0.0001 **** <0.0001 **** <0.0001 **** <0.0001 ****	
114	7g		Median of Control siRNA vs. zero Median of $\alpha$ Actn1 siRNA vs. zero Median of CapZ $\beta$ siRNA vs. zero Median of CapZ $\beta$ & $\alpha$ Actn1 siRNAs vs. zero Median of LatA vs. zero Median of LatA+ $\alpha$ Actn1 siRNA vs. zero	0.0028 ** <0.0001 **** <0.0001 **** <0.0001 **** <0.0001 **** <0.0001 ****	
115	7g		Median of Control siRNA vs. zero Median of $\alpha$ Actn1 siRNA vs. zero Median of CapZ $\beta$ siRNA vs. zero Median of CapZ $\beta$ & $\alpha$ Actn1 siRNAs vs. zero Median of LatA vs. zero Median of LatA+ $\alpha$ Actn1 siRNA vs. zero	0.0028 ** <0.0001 **** <0.0001 **** <0.0001 **** <0.0001 **** <0.0001 ****	
116	7h		Median of Control siRNA vs. zero Median of $\alpha$ Actn1 siRNA vs. zero Median of CapZ $\beta$ siRNA vs. zero Median of CapZ $\beta$ & $\alpha$ Actn1 siRNAs vs. zero Median of LatA vs. zero Median of LatA+ $\alpha$ Actn1 siRNA vs. zero	<0.0001 **** <0.0001 **** <0.0001 **** <0.0001 **** <0.0001 **** <0.0001 ****	
117	7h		Median of Control siRNA vs. zero Median of $\alpha$ Actn1 siRNA vs. zero Median of CapZ $\beta$ siRNA vs. zero Median of CapZ $\beta$ & $\alpha$ Actn1 siRNAs vs. zero Median of LatA vs. zero Median of LatA+ $\alpha$ Actn1 siRNA vs. zero	<0.0001 **** <0.0001 **** <0.0001 **** <0.0001 **** <0.0001 **** <0.0001 ****	
118		Mann-Whitney	Control vs. 20nM LatA (Aspect Ratio 1:2)	<0.0001 ****	
119		9c	Wilcoxon test	Median of Control vs. zero (Aspect Ratio 1:2)	<0.0001 ****
120			Median of 20nM LatA vs. zero (Aspect Ratio 1:2)	<0.0001 ****	
121		Mann-Whitney	Control vs. 20nM LatA (Aspect Ratio 1:3)	<0.0001 ****	
122		9f	Wilcoxon test	Median of Control vs. zero (Aspect Ratio 1:3)	<0.0001 ****
123			Median of 20nM LatA vs. zero (Aspect Ratio 1:3)	<0.0001 ****	
124		Supp Fig. 2b		Control siRNA vs. mDia1 siRNA	<0.0001 ****
125			Control siRNA vs. FMNL2 siRNA	<0.0001 ****	
126			Control siRNA vs. FHOD3 siRNA	<0.0001 ****	
127			Control siRNA vs. Daam1 siRNA	<0.0001 ****	
128		Supp Fig. 2c		Control siRNA vs. FMNL2 siRNA	0.1131 ns
129			Control siRNA vs. mDia3 siRNA	>0.9999 ns	
130			Control siRNA vs. mDia2 siRNA	>0.9999 ns	
131			Control siRNA vs. INF2 siRNA	>0.9999 ns	
132			Control siRNA vs. FHOD1 siRNA	>0.9999 ns	
133			Control siRNA vs. Daam2 siRNA	>0.9999 ns	
134		Supp Fig. 2b		mDia1 siRNA vs. FMNL2 siRNA	<0.0001 ****
135			mDia1 siRNA vs. Daam1 siRNA	<0.0001 ****	
136			Median of Control siRNA vs. zero	<0.0001 ****	
137		Supp Fig. 2b		Median of mDia1 siRNA vs. zero	<0.0001 ****
138			Median of FMNL2 siRNA vs. zero	<0.0001 ****	
139			Median of FHOD3 siRNA vs. zero	<0.0001 ****	
140			Median of Daam1 siRNA vs. zero	<0.0001 ****	
141		Wilcoxon test		Median of FMNL2 siRNA vs. zero	<0.0001 ****
142		Supp Fig. 2c		Median of mDia3 siRNA vs. zero	<0.0001 ****
143			Median of mDia2 siRNA vs. zero	<0.0001 ****	
144			Median of INF2 siRNA vs. zero	<0.0001 ****	
145			Median of FHOD1 siRNA vs. zero	<0.0001 ****	
146			Median of Daam2 siRNA vs. zero	<0.0001 ****	
147		Supp Fig. 2g		Control siRNA vs. FMNL2 siRNA	0.0027 **
148			Control siRNA vs. FHOD3 siRNA	<0.0001 ****	
149			Control siRNA vs. Daam1 siRNA	0.0425 *	
150			Control siRNA vs. FMNL2 siRNA	>0.9999 ns	
151		Supp Fig. 2h		Control siRNA vs. mDia3 siRNA	>0.9999 ns
152			Control siRNA vs. mDia2 siRNA	0.054 ns	
153			Control siRNA vs. INF2 siRNA	<0.0001 ****	
154			Control siRNA vs. FHOD1 siRNA	>0.9999 ns	
155			Control siRNA vs. Daam2 siRNA	>0.9999 ns	
156		Supp Fig. 2g		Median of Control siRNA vs. zero	<0.0001 ****
157			Median of FMNL2 siRNA vs. zero	<0.0001 ****	
158			Median of FHOD3 siRNA vs. zero	<0.0001 ****	
159		Wilcoxon test		Median of Daam1 siRNA vs. zero	<0.0001 ****
160			Median of mDia3 siRNA vs. zero	<0.0001 ****	
161		Supp Fig. 2h		Median of FMNL2 siRNA vs. zero	<0.0001 ****
162			Median of mDia3 siRNA vs. zero	0.0044 **	
163			Median of mDia2 siRNA vs. zero	<0.0001 ****	
164			Median of INF2 siRNA vs. zero	<0.0001 ****	
165			Median of FHOD1 siRNA vs. zero	<0.0001 ****	
166			Median of Daam2 siRNA vs. zero	<0.0001 ****	
167		Supp Fig. 5a	Mann-Whitney	Control siRNA vs. ARPC2 siRNA	<0.0001 ****
168			Wilcoxon test	Median of ARPC2 siRNA vs. zero	<0.0001 ****
169	Supp Fig. 5, e vs. c			Control siRNA vs. Cofilins1&2 siRNAs	<0.0001 ****
170	Supp Fig. 5, c vs. e		Kruskal-Wallis	Cofilins1&2 siRNAs vs. Cofs siRNAs+Cof1 rescue	0.0001 ***
171		Supp Fig. 5e		Control siRNA vs. Cofs siRNAs+Cof1 rescue	0.2418 ns
172			Control siRNA vs. ADF siRNA	0.0386 *	
173			Control siRNA vs. Cofs&ADF siRNAs	<0.0001 ****	
174		Supp Fig. 5c		Median of Cofilins1&2 siRNAs vs. zero	<0.0001 ****
175			Median of Control siRNA vs. zero	<0.0001 ****	
176		Supp Fig. 5e	Wilcoxon test	Median of ADF siRNA vs. zero	<0.0001 ****
177			Median of Cofs siRNAs vs. zero	0.9554 ns	
178			Median of Cofs siRNAs+Cof1 rescue vs. zero	0.0001 ***	
179		Supp Fig. 5h	Kruskal-Wallis	Control siRNA vs. ARPC2 siRNA	0.0004 ***
180			Control siRNA vs. Cofilins1&2 siRNAs	<0.0001 ****	
181			Control siRNA vs. ADF siRNA	<0.0001 ****	
182			Control siRNA vs. Cofs&ADF siRNAs	0.0046 **	
183		Supp Fig. 5h	Wilcoxon test	Median of Control siRNA vs. zero	<0.0001 ****
184			Median of ARPC2 siRNA vs. zero	<0.0001 ****	
185			Median of Cofilins1&2 siRNAs vs. zero	<0.0001 ****	
186			Median of ADF siRNA vs. zero	<0.0001 ****	
187			Median of Cofs&ADF siRNAs vs. zero	<0.0001 ****	
188	Supp Fig. 6, c vs. a	Kruskal-Wallis	Mean RF tilt angle	Control siRNA vs. VASP siRNA	0.0167 *
189	Supp Fig. 6, c vs. b			Control siRNA vs. VASP&Mena siRNAs	<0.0001 ****
190	Supp Fig. 6a	Wilcoxon test	Mean RF tilt angle	Median of VASP siRNA vs. zero	<0.0001 ****
191	Supp Fig. 6b			Median of VASP&Mena siRNAs vs. zero	<0.0001 ****
192	Supp Fig. 6f	Kruskal-Wallis	Mean nematic director angle	Control siRNA vs. VASP siRNA	0.3084 ns
193			Control siRNA vs. VASP&Mena siRNAs	>0.9999 ns	
194		Supp Fig. 6f	Wilcoxon test	Median of Control siRNA vs. zero	<0.0001 ****
195			Median of VASP siRNA vs. zero	<0.0001 ****	
196			Median of VASP&Mena siRNAs vs. zero	<0.0001 ****	
197		Supp Fig. 7e		Control siRNA vs. Profilin1 siRNA	<0.0001 ****
198			Control siRNA vs. Profilin2 siRNA	0.0002 ***	
199			Control siRNA vs. CapZ $\beta$ siRNA	<0.0001 ****	
200			Control siRNA vs. 20nM LatA	<0.0001 ****	
201			Control siRNA vs. 5nM SwinA	<0.0001 ****	
202		Supp Fig. 7e	Wilcoxon test	Median of Control siRNA vs. zero	<0.0001 ****
203			Median of Profilin 1 siRNA vs. zero	<0.0001 ****	
204			Median of Profilin 2 siRNA vs. zero	<0.0001 ****	
205			Median of CapZ $\beta$ siRNA vs. zero	<0.0001 ****	
206			Median of 20nM LatA vs. zero	<0.0001 ****	
207			Median of 5nM SwinA vs. zero	<0.0001 ****	
208	Supp Fig. 8, a vs. b	Kruskal-Wallis	Mean nuclei orient.	Control cell vs. Enucleated cell	>0.9999 ns
209	Supp Fig. 8, a vs. c			Control cell vs. Control cell+LatA	<0.0001 ****
210	Supp Fig. 8, c vs. d			Control cell+LatA vs. Enucleated cell+LatA	>0.9999 ns
211	Supp Fig. 8, b vs. d			Enucleated cell vs. Enucleated cell+LatA	<0.0001 ****
212	Supp Fig. 8a		Wilcoxon test	Median of Control cell	<0.0001 ****
213	Supp Fig. 8b			Median of Enucleated cell	<0.0001 ****
214	Supp Fig. 8c			Median of Control cell+LatA	<0.0001 ****
215	Supp Fig. 8d			Median of Enucleated cell+LatA	0.0109 *

216	Supp Fig. 9f	Mann-Whitney	Mean RF tilt angle	LatA vs. LatA+ABDdel $\alpha$ Actn mutant	<0.0001	****
217				Median of 20nM LatA vs. zero	<0.0001	****
218		Wilcoxon test		Median of LatA+ABDdel $\alpha$ Actn mutant vs. zero	0.616	ns
219	Supp Fig. 10, c vs. a Supp Fig. 10, c vs. b	Kruskal-Wallis	Mean RF tilt angle	Control siRNA vs. MYO1c siRNA	>0.9999	ns
220				Control siRNA vs. MYO1d siRNA	0.0783	ns
221	Supp Fig. 10a Supp Fig. 10b	Wilcoxon test	Mean RF tilt angle	Median of MYO1c siRNA vs. zero	<0.0001	****
222				Median of MYO1d siRNA vs. zero	<0.0001	****
223	Supp Fig. 10f	Kruskal-Wallis	Mean nematic director angle	Control siRNA vs. MYO1c siRNA	<0.0001	****
224				Control siRNA vs. MYO1d siRNA	0.2975	ns
225				Median of Control siRNA vs. zero	<0.0001	****
226	Supp Fig. 10f	Wilcoxon test	Mean nematic director angle	Median of MYO1c siRNA vs. zero	<0.0001	****
227				Median of MYO1d siRNA vs. zero	<0.0001	****
228	1j vs. 5d	Kruskal-Wallis	Mean RF tilt angle	mDia1 siRNA vs. mDia1 siRNA	>0.9999	ns
229	1i vs. 5a			Control siRNA vs. Control siRNA	0.0001	***
230	3b vs. 5b	Kruskal-Wallis	Mean RF tilt angle	Profilin1 siRNA vs. Profilin1 siRNA	>0.9999	ns
231	3b vs. 7b			Profilin1 siRNA vs. Pfn1 siRNA	0.4581	ns
232	5b vs. 7b			Profilin1 siRNA vs. Pfn1 siRNA	0.0748	ns
233	3a vs. 5a			Control siRNA vs. Control siRNA	0.0289	*
234	3a vs. 7a			Control siRNA vs. Control siRNA	0.5144	ns
235	5a vs. 7a			Control siRNA vs. Control siRNA	>0.9999	ns
236	3e vs. 7c			CapZ $\beta$ siRNA vs. CapZ $\beta$ siRNA	>0.9999	ns
237	3f vs. 7a			Control siRNA #2 vs. Control siRNA	>0.9999	ns
238	3g vs. 5c	Kruskal-Wallis	Mean RF tilt angle (8 - 12 $\mu$ m)	20nM LatA vs. Control siRNA+LatA	>0.9999	ns
239	3g vs. 7d			20nM LatA vs. LatA	>0.9999	ns
240	3g vs. Supp Fig. 8c			20nM LatA vs. Control cell+LatA	>0.9999	ns
241	5c vs. 7d			Control siRNA+LatA vs. LatA	>0.9999	ns
242	5c vs. Supp Fig. 8c			Control siRNA+LatA vs. Control cell+LatA	>0.9999	ns
243	7d vs. Supp Fig. 8c			LatA vs. Control cell+LatA	>0.9999	ns
244	3h vs. 5a			Untreated Control vs. Control siRNA	<0.0001	****
245	3h vs. 7a			Untreated Control vs. Control siRNA	0.0085	**
246	3h vs. Supp Fig. 8a			Untreated Control vs. Control cell	>0.9999	ns
247	5a vs. 7a			Control siRNA vs. Control siRNA	>0.9999	ns
248	5a vs. Supp Fig. 8a			Control siRNA vs. Control cell	0.1523	ns
249	7a vs. Supp Fig. 8a			Control siRNA vs. Control cell	>0.9999	ns
250	4c vs. 7e	Kruskal-Wallis	Mean nematic director angle	Control siRNA vs. Control siRNA	>0.9999	ns
251	4c vs. 7f			Profilin1 siRNA vs. Pfn1 siRNA	0.1574	ns
252	4c vs. 7g			CapZ $\beta$ siRNA vs. CapZ $\beta$ siRNA	0.0422	*
253	4c vs. 7h			20nM LatA vs. LatA	<0.0001	****

All statistical tests were implemented using Graphpad Prism software (version 9.4.1).

Statistical significance is defined as P<0.05 for all tests.

Two-tailed Mann-Whitney test was used.

Kruskal-Wallis test was implemented with Dunn's multiple comparisons test and report multiplicity adjusted P value for each comparison.

Wilcoxon signed-rank test was implemented against a hypothetical value of zero.

See Methods for details of computation of mean radial fibre (RF) tilt angle of individual cells and mean nematic director angle and mean nuclei orient. of cell collectives in microcultures.  
Parameter: Mean radial fibre (RF) tilt angle refers to measurements in the 6–10  $\mu$ m annuli in cells (unless otherwise stated).

**Supplementary Table 2. Mean radial fibre (RF) tilt angles at the 6-10  $\mu\text{m}$  annulus and corresponding mean nematic director angles for rectangular microcultures for each type of treatment.** Ranks and sample sizes (n) are included. See also Fig. 8 and Supplementary Fig. 12.

Rank of RF tilt angle	Condition(s)	Mean RF tilt angle ( $^{\circ}$ )	Mean nematic director angle ( $^{\circ}$ )	Rank of nematic director angle	n= (cells)	n= (micro-cultures)
1	5nM SwinA	-11.80 $\pm$ 0.78	-13.43 $\pm$ 0.70	4	153	1108
2	20nM LatA	-10.24 $\pm$ 0.48	-22.47 $\pm$ 0.54	2	490	1416
3	GFP- $\alpha$ Actn1	-5.18 $\pm$ 0.60	-4.15 $\pm$ 0.65	7	156	745
4	Profilin1 siRNA	-4.59 $\pm$ 0.51	-17.50 $\pm$ 0.77	3	431	715
5	$\alpha$ Actn1 + 20nM LatA	-2.38 $\pm$ 1.55	-26.24 $\pm$ 1.20	1	94	237
6	CAPZ $\beta$ siRNA	-2.21 $\pm$ 0.52	-7.56 $\pm$ 0.72	6	409	661
7	Profilins1&2 siRNAs	-0.37 $\pm$ 1.08	-8.59 $\pm$ 1.38	5	76	207
8	COFs & ADF siRNAs	-0.11 $\pm$ 0.41	11.16 $\pm$ 1.19	20	308	216
9	GFP- $\alpha$ Actn4	1.68 $\pm$ 0.97	-0.07 $\pm$ 0.88	8	92	417
10	ARPC2 siRNA	2.59 $\pm$ 0.53	10.38 $\pm$ 1.05	19	434	342
11	mDia1 siRNA	2.78 $\pm$ 0.36	4.02 $\pm$ 0.71	9	515	894
12	Cofilins1&2 siRNA	3.37 $\pm$ 0.43	10.00 $\pm$ 0.99	18	426	373
13	PFNs & $\alpha$ Actn1 siRNAs	4.45 $\pm$ 0.76	6.39 $\pm$ 1.34	11	295	227
14	FMNL2 siRNA	6.66 $\pm$ 0.64	8.87 $\pm$ 0.95	15	227	454
15	FHOD3 siRNA	7.08 $\pm$ 0.64	5.99 $\pm$ 0.87	10	262	407
16	VASP & Mena siRNAs	7.63 $\pm$ 0.76	12.26 $\pm$ 1.10	21	143	366
17	DAAM1 siRNA	7.78 $\pm$ 0.70	8.21 $\pm$ 1.44	14	268	165
18	FMN2 siRNA	7.97 $\pm$ 0.92	16.02 $\pm$ 1.49	29	115	181
19	ADF siRNA	9.38 $\pm$ 0.54	24.36 $\pm$ 1.01	35	339	295
20	mDia3 siRNA	9.58 $\pm$ 0.99	9.05 $\pm$ 2.93	16	98	32

21	mDia2 siRNA	9.93±0.60	9.41±1.04	17	283	419
22	INF2 siRNA	9.95±0.53	22.56±0.74	34	356	495
23	MYO1c siRNA	10.29±0.58	21.99±0.98	33	181	406
24	GFP-ABDdel αActn mutant	10.51±0.87	14.99±1.37	25	85	206
25	CAPZβ & αActn1 siRNAs	10.69±0.73	18.73±0.78	32	219	360
26	VASP siRNA	10.84±0.46	15.70±1.78	27	395	202
27	MYO1d siRNA	11.01±0.69	13.78±0.86	23	171	440
28	FHOD1 siRNA	11.45±0.91	15.03±1.26	26	147	157
29	DAAM2 siRNA	11.66±1.10	15.92±1.25	28	100	215
30	Pfn1 & αActn1 siRNAs	11.84±1.33	7.90±1.67	12	42	135
31	Control	11.85±0.25	12.56±0.28	22	1559	4432
32	αActn1&4 siRNAs	15.47±1.22	16.19±1.07	30	105	182
33	Profilin2 siRNA	17.16±0.63	14.98±0.76	24	182	519
34	αActn1 siRNA	17.35±0.62	17.61±0.78	31	264	430
35	αActn4 siRNA	18.00±0.70	8.20±1.47	13	116	135

**Supplementary Table 3. List of siRNAs used.**

siRNA	Company, Product name or Target Sequence(s)	Catalogue No.
Control	Dharmacon, ON-TARGETplus Non-targeting control	D-001810-01
Alpha-Actinin1	Dharmacon, ON-TARGETplus SMARTpool, Human ACTN1 siRNA	L-011195-00
Alpha-Actinin4	Dharmacon, ON-TARGETplus SMARTpool, Human ACTN4 siRNA	L-011988-00
ADF	Dharmacon, ON-TARGETplus, Human DSTN siRNA	J-012303-05 & J-012303-06
ARPC2	Dharmacon, ON-TARGETplus SMARTpool, Human ARPC2 siRNA	L-012081-00
CapZ $\beta$	Dharmacon, ON-TARGETplus SMARTpool, Human CAPZB siRNA	L-011990-00
Cofilin 1	Santa Cruz Biotechnology Inc, Cofilin 1 siRNA (h)	sc-35078
Cofilin 2	Santa Cruz Biotechnology Inc, Cofilin 2 siRNA (h)	sc-37027
DAAM1	Santa Cruz Biotechnology Inc, DAAM1 siRNA (h)	sc-62190
DAAM2	Santa Cruz Biotechnology Inc, DAAM2 siRNA (h)	sc-62192
FHOD1	Santa Cruz Biotechnology Inc, FHOD1 siRNA (h)	sc-60635
FHOD3	Dharmacon, ON-TARGETplus SMARTpool, Human FHOD3 siRNA	L-023411-01
FMNL2	Dharmacon, ON-TARGETplus, Human FMNL2 siRNA	J-031993-09 & J-031993-10
FMN2	Santa Cruz Biotechnology Inc, Formin 2 siRNA (h)	sc-43765
INF2	Santa Cruz Biotechnology Inc, INF2 siRNAs (h)	sc-92159
mDia1	Dharmacon, ON-TARGETplus, Human DIAPH1 siRNA	J-010347-06
mDia2	Dharmacon, ON-TARGETplus SMARTpool, Human DIAPH3 siRNA	L-018997-00
mDia3	Dharmacon, ON-TARGETplus, Human DIAPH2 siRNA	J-012029-05 & J-012029-06
Mena	Santa Cruz Biotechnology Inc, Mena siRNA (h)	sc-43496
MYO1c	Santa Cruz Biotechnology Inc, Myosin 1c siRNA (h)	sc-44604
MYO1d	Santa Cruz Biotechnology Inc, Myosin 1d siRNA (h)	sc-44608
Profilin 1	5'-GCAAAGACCGGUCAAGUUU-3' and 5'-CACGGUGGUUUGAUCAACA-3'	
Profilin 2	5'-GUAGAGCAUUGGUUAUAGU-3' and 5'-CCAGGGACAUUCCAUCUU-3'	
VASP	Santa Cruz Biotechnology Inc, VASP siRNA (h)	sc-29516

**Supplementary Table 4. List of antibodies used.**

Target	Company	Catalogue No.	Dilution
$\alpha$ -Tubulin	Sigma-Aldrich	T6199	1:5000
$\alpha$ -Actinin1	US Biological	A0761-02F	1:1000
ADF	Abcam	ab186754	1:1000
ARP2	Santa Cruz Biotechnology Inc	sc-166103 (E-12)	1:1000
ARPC2	Santa Cruz Biotechnology Inc	sc-515754 (F-5)	1:1000
CAPZ $\beta$	Abcam	ab175212	1:1000
Cofilins1&2	Santa Cruz Biotechnology Inc	sc-376476 (E-8)	1:1000
DAAM1	Abcam	ab56951	1:1000
DAAM2	Santa Cruz Biotechnology Inc	sc-515129 (E-1)	1:1000
FHOD1	ECM Biosciences	FM3521	1:1000
FMN2	Santa Cruz Biotechnology Inc	sc-376787 (C-3)	1:1000
GAPDH	Santa Cruz Biotechnology Inc	sc-47724 (0411)	1:5000
INF2	Proteintech	20466-1-AP	1:1000
mDia1	BD Biosciences	610849	1:1000
mDia3	ECM Biosciences	DP4511	1:1000
MYO1c	Santa Cruz Biotechnology Inc	sc-136544 (13)	1:1000
MYO1d	Santa Cruz Biotechnology Inc	sc-515292 (H-1)	1:1000
Myosin IIA	Sigma Aldrich	M8064	1:800
Profilin 1	Santa Cruz Biotechnology Inc	sc-137235 (B-10)	1:1000
Profilin 2	Santa Cruz Biotechnology Inc	sc-100955 (4K-6)	1:1000
VASP	Santa Cruz Biotechnology Inc	sc-46668 (A-11)	1:1000
Vinculin	Sigma Aldrich	V9131	1:400
IRDye® 680RD Goat anti-Rabbit IgG	LI-COR, Inc.	926-68071	1: 5000
IRDye® 800CW Goat anti-Mouse IgG	LI-COR, Inc.	926-32210	1:15,000
goat anti-rabbit IgG-HRP	Santa Cruz Biotechnology Inc	sc-2004	1:10,000
goat anti-mouse IgG-HRP	Santa Cruz Biotechnology Inc	sc-2005	1:10,000
Donkey anti-Mouse IgG (H+L) Highly Cross-Adsorbed Secondary Antibody, Alexa Fluor™ 488	Invitrogen	A-21202	1:500
Donkey anti-Rabbit IgG (H+L) Highly Cross-Adsorbed Secondary Antibody, Alexa Fluor™ 647	Invitrogen	A31573	1:500